## Uniaxial strain effects on quantum materials probed by electronic transport

Lorenz, J.P.

**Publication date**
2025
**Document Version**
Final published version

# **Uniaxial strain effects** on **quantum materials** probed by **electronic transport**

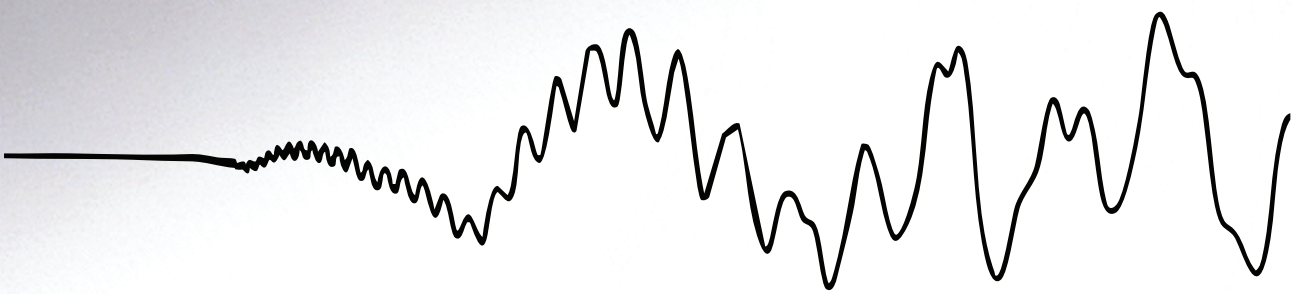

Jelle P. Lorenz

# Uniaxial strain effects on quantum materials probed by electronic transport

*Uniaxial strain effects on quantum materials probed by electronic transport*
Ph.D. Thesis, University of Amsterdam, May 2025
Jelle Pepijn Lorenz

The work described in this thesis was performed at the Van der Waals-Zeeman Institute, Institute of Physics, University of Amsterdam, Science Park 904, 1098 XH Amsterdam, The Netherlands, and at the High Field Magnet Laboratory, Radboud University, Toernooiveld 7, 6525 ED Nijmegen, The Netherlands. It was financed in the framework of the TOPCORE consortium (OCENW.GROOT.2019.048) by the Netherlands Organisation for Scientific Research (NWO).

ISBN: 978-94-6473-830-8

Cover:
*A quantum oscillation of ZrSiS. Designed by Dennis Bierreth-Fernandez.*

Printed by: proefschriften.nl

Uniaxial strain effects on quantum materials probed by electronic transport

ACADEMISCH PROEFSCHRIFT

ter verkrijging van de graad van doctor
aan de Universiteit van Amsterdam
op gezag van de Rector Magnificus
prof. dr. ir. P.P.C.C. Verbeek
ten overstaan van een door het College voor Promoties ingestelde commissie,
in het openbaar te verdedigen in de Aula der Universiteit
op donderdag 19 juni 2025, te 11.00 uur

door Jelle Pepijn Lorenz
geboren te Delft

***Promotiecommissie***

| | | |
|---|---|---|
| *Promotor:* | dr. A. de Visser | Universiteit van Amsterdam |
| *Copromotor:* | prof. dr. M.S. Golden | Universiteit van Amsterdam |
| *Overige leden:* | dr. A. Isaeva | Universiteit van Amsterdam |
| | dr. E. van Heumen | Universiteit van Amsterdam |
| | prof. dr. P. Schall | Universiteit van Amsterdam |
| | prof. dr. J. van Wezel | Universiteit van Amsterdam |
| | dr. S.R. Wiedmann | Radboud Universiteit |
| | prof. dr. ir. A. Brinkman | Universiteit Twente |

Faculteit der Natuurwetenschappen, Wiskunde en Informatica

# Contents

# 1 Introduction

Quantum physics is required to properly explain many phenomena in crystalline materials. The phenomena often include quantized states, collective behaviors, and emergent properties that are the result of the wave-like nature of particles that is not embodied in classical physics [1]. There are very large differences in the resistivities of metals and insulators even though they are composed of similar amounts of atomic nuclei and electrons. Some materials exhibit zero electrical resistance below a certain temperature, i.e. they superconduct. In two-dimensional electron systems at low temperatures and high magnetic fields, the Hall conductance is found to be quantized in integer or fractional values. Other materials conduct electricity on their surfaces while being insulating in the bulk owing to their non-trivial topological character.

All these phenomena can be properly described by quantum mechanics. Our comprehension of electronic band structure, superconductivity, the quantum Hall effect, and non-trivial topology has been central to the development of the information age. Quantum materials are foundational in a great number of advanced technologies, such as microelectronics, magnetic resonance imaging (MRI), quantum computing, light-emitting diodes (LEDs), and magnets used for electric motors and wind turbines.

The electronic properties of a crystal are directly determined by the symmetries of its lattice. These symmetries control phenomena such as band gaps, degeneracies, and the existence of exotic states. Uniaxial strain can be used to explore the delicate connection between electronic band structure and the underlying crystal lattice, by breaking rotational symmetry and tuning lattice parameters without introducing impurities or defects. On top of that, all strain effects are fully reversible as long as the crystal stays within its elastic limit.

Here follows a short introduction to quantum materials, including basic information about electronic band structure and emergent phenomena relevant to this thesis. This is followed by an introductory description of uniaxial strain. Lastly, I will briefly address quantum oscillations, which has been the most important phenomenon used to probe strain-induced effects on the electronic properties of materials in this work.

## 1.1 Quantum materials

At the atomic level, the dynamic interplay between the four fundamental degrees of freedom in quantum materials – lattice, charge, orbital, and spin – gives rise to a diverse and often intricate range of electronic states with physically allowed energies called bands [2]. These states can be regarded as collective excitations of the electrons in the momentum space of the system, known as quasiparticles. Energy levels that are forbidden are called band gaps. Electronic band structure refers to the energy-momentum space that incorporates all states. Electrons fill the available states from the lowest energy, with each state being occupied by two electrons due to the Pauli exclusion principle. The level to which the bands are filled with electrons is determined by the Fermi energy $E_\mathrm{F}$ or Fermi level, which is the highest occupied energy at 0 K. At higher temperatures, the Fermi-Dirac distribution function broadens and allows electrons to occupy states in a range around $E_\mathrm{F}$. In semiconductors with sufficiently small band gaps this broadening can lead to electrons being excited to the lowest unoccupied band (conduction band), leaving a hole in the highest occupied band (valence band) and creating an electron-hole pair. The hole is a quasiparticle that can behave similarly to an excited electron.

In this thesis, we frequently investigate the material classification known as semimetals, in which the valence and conduction bands touch or overlap slightly. When relating $E_\mathrm{F}$ to the momentum of the bands at the Fermi level, one can map out the boundary for the filled electronic states in momentum space. This is called the Fermi surface, and for semimetals its volume is very small. It therefore comprises low electron densities and weak electron-electron interactions, leading to quasiparticles in semimetals behaving as if they only possess a fraction of the free electron mass. This is desirable, as it can lead to relatively large responses to external parameters such as magnetic fields or uniaxial strain.

### 1.1.1 Topological materials

In topological quantum materials, the band structure has unique features that are protected by topology – originally a mathematical concept. The key idea there is that topology focuses on topological equivalence, meaning two shapes can be continuously deformed into each other without cutting or merging parts. A donut and a coffee cup can smoothly be transformed into the other without cutting or tearing. Some properties of the donut change (size, curvatures), while others stay the same

(number of holes). Analogous to this, topological materials have electronic states that are topologically protected. Topological insulators possess an insulating bulk with a conducting surface. Because the surface states here are topologically protected, they are robust and will not be affected by disruptions such as impurities or defects. Some topological materials exhibit unique properties such as massless Dirac fermions. The fascinating resilience of topologically non-trivial states has the potential to open new frontiers in fields where control of quantum states is critical.

If the conduction and valence bands possess linear dispersion and cross each other, the point where they touch is referred to as a Dirac node. If this crossing happens close to the Fermi level and (alone or together with other such crossings) dominates the electronic transport properties of a material, that material is considered to be a Dirac semimetal [3]. These materials possess topologically protected states, as the Dirac nodes are protected by symmetries such as time-reversal symmetry and inversion symmetry. Breaking either of these symmetries can lift the four-fold degeneracy of the Dirac node and convert the Dirac semimetal into a Weyl semimetal, which possesses two-fold degenerate Weyl nodes with opposite chirality. Fig. 1.1(a) shows a band crossing in two dimensions of momentum space to yield a Dirac node. Bismuth, covered in chapter 5, is known to exhibit a transition from a topologically trivial phase to a topologically non-trivial Dirac semimetal phase with Sb doping [4].

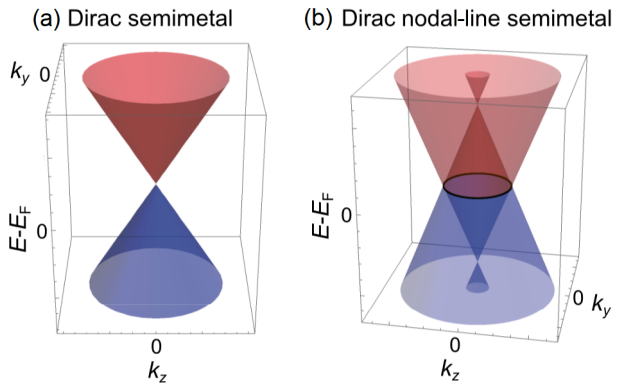


**Figure 1.1.** Low-energy spectrum $E(0, k_y, k_z)$ for a Dirac semimetal and a Dirac nodal-line semimetal. Adapted from [5].

When the conduction and valence bands cross each other along a continuous line in momentum space, instead of a single point a nodal line is created and the material is categorized as a Dirac nodal-line semimetal (NLSM), see Fig. 1.1(b) [3]. Here, the nodal line is symmetry-protected and can lead to interesting electronic properties, such as 'drumhead-like' surface states with high electron density ideal for exploring electron correlation effects, high carrier mobility, and which show unusual magnetoresistance properties [6–9]. In chapter 3 we discuss our research on the NLSM ZrSiS, which shows how uniaxial strain can be used to tune the quantum mobility of its quasiparticle orbits.

### 1.1.2 Superconductivity

Because superconductivity is a common property of materials we have studied, an introduction is warranted. A superconductor has a critical temperature $T_c$ and critical field $B_c$, below which the material exhibits zero electrical resistance [10, 11]. Superconductivity is conventionally well described by Bardeen-Cooper-Schrieffer (BCS) theory, dictating that macroscopic coherence is the result of Cooper pair formation. Electrons near the Fermi surface pair up despite their mutual Coulomb repulsion due to their interaction with phonons – quasiparticles resulting from lattice vibrations. As an electron moves through the lattice it slightly distorts it, which attracts an electron of opposite momentum and spin. The formation of the pairs of attracted electrons, the Cooper pairs, opens up a small energy gap $2\Delta$ in the electronic density of states at the Fermi level. This gap is not to be confused with a band gap, but principally serves the same purpose of representing the required energy necessary to bridge it. If the thermal energy $k_{\mathrm{B}}T$ is low enough, there is no scattering process that is able to provide sufficient energy to excite both electrons of a Cooper pair across the gap. This means the entire correlated system is resistant to scattering due to its macroscopic phase-coherence. In this way, Cooper pairs contribute to zero electrical resistance.

Not all superconductors can be properly described by BCS theory, as it is limited to conventional superconductors where electron-phonon coupling is the pairing mechanism. In high-temperature superconductors or unconventional superconductors other mechanisms such as spin fluctuations may be involved [12, 13]. In chapter 4 we investigate the very large critical field of $LaO_{0.8}F_{0.2}BiS_{2-x}Se_x$, a layered superconductor with local inversion asymmetry. In this material, spin polari-

sation based on Rashba-type spin-orbit coupling has been observed and is believed to be responsible for its anisotropic superconducting properties.

### 1.1.3 Charge density waves

When electron-phonon coupling is sufficiently strong in a material, periodic modulations of the electronic charge density coupled with periodic distortions of the underlying atomic lattice can occur. These modulations called charge density waves (CDWs) are relevant to this thesis as they are an important material property of two materials studied, $NbSe_2$ and $ZrTe_3$. The lattice distortion opens up an energy gap similar to the superconducting energy gap, stabilizing the CDW phase. CDWs are most prominent in low-dimensional systems (1D or quasi-2D), where Fermi surface nesting is enhanced and the order originates from the Peierls instability. Nesting refers to a concept in which parallel portions of the Fermi surface that can be connected by a single wavevector tend to strongly interact, and is a geometric feature that is known to enhance electronic instabilities. CDWs can also arise from other mechanisms, such as strong electron-phonon coupling like in $NbSe_2$ [14], and are sometimes linked to topological band structure features [15, 16].

Because the CDW phase and superconducting phase involve different rearrangements of electronic states near the Fermi surface, the two phases often suppress each other [17–22]. CDWs 'gap out' parts of the Fermi surface by opening an energy gap, reducing the density of states available for superconducting pairing. Alternatively, the application of a magnetic field below superconducting $T_c$ suppresses superconductivity and enhances the CDW phase [19]. External tuning parameters can influence the competition between CDWs and superconductivity. Applying hydrostatic pressure reduces the ability of electron-phonon coupling to distort the lattice and may thereby suppress the CDW phase and enhance superconductivity, while chemical doping alters the electronic density and may have similar effects [23, 24]. Studying the interplay between CDWs and superconductivity could provide insights to the mechanisms underlying unconventional superconductivity. Additionally, it may shine light on how electronic correlations, lattice effects, and dimensionality influence quantum phases and their tunability. In this thesis, we use uniaxial strain as a tuning parameter to research CDWs and their competition with superconductivity. See chapter 6 for our studies on the transition metal di- and trichalcogenides $NbSe_2$ and $ZrTe_3$.

## 1.2 Uniaxial strain

### 1.2.1 Stress and strain

When a load is applied to a sample, the deformation it causes can be described as both stress and strain [25, 26], see Fig. 1.2. Stress ($\sigma$) is a measure of the internal forces that develop within a material when subjected to external loads and is given in units of $N/m^2$ or Pa. Strain ($\varepsilon$) measures the deformation or displacement in a material relative to its original size and is dimensionless. The mathematical expression for strain is $\varepsilon = \frac{\Delta L}{L_0}$, with $\Delta L$ the change in length and $L_0$ the original length. At low strains where the material is still in the elastic regime, stress and strain are directly related through Hooke's Law $\sigma = E\varepsilon$, where $E$ is the Young's modulus, a material-specific constant. Just as for stress, there are two types of strain: normal strain which describes a relative change in length along a particular axis, and shear strain which describes a relative change in angle between two straight lines along different axes.

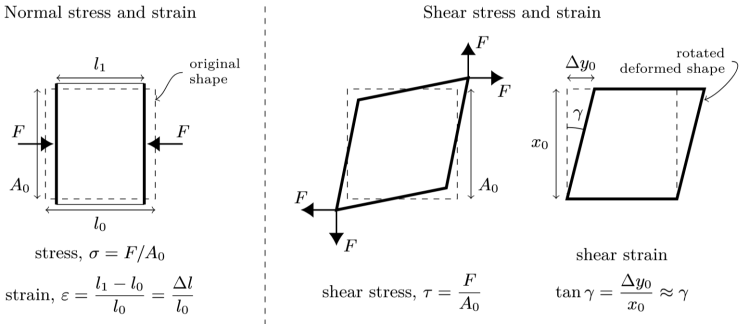


**Figure 1.2.** Definitions of normal stress and strain, and shear stress and strain. Adapted from [27]

It can be advantageous to use the tensor representation of strain. The strain tensor $\varepsilon_{ij}$ measures the relative deformation of the material in the $i$-th direction due to a displacement in the $j$-th direction. The indices $i$ and $j$ can take values corresponding to the Cartesian coordinates $x, y, z$. Diagonal strain tensor components ($\varepsilon_{xx}$, $\varepsilon_{yy}$, $\varepsilon_{zz}$) represent normal strain, while off-diagonal strain tensor components ($\varepsilon_{xy}$, $\varepsilon_{xz}$, $\varepsilon_{yz}$) represent shear strain. For example, $\varepsilon_{xz}$ measures the deformation in the $x$-direction caused by displacement in the $z$-direction. In the Voigt

notation, the $i$ and $j$ indices are reduced to one index $m$ through $xx \rightarrow 1, yy \rightarrow 2$, $zz \rightarrow 3, yz \rightarrow 4, xz \rightarrow 5$, and $xy \rightarrow 6$. The same can be done for the stress tensor, and leads to the resulting stress and strain vectors being linked via the elasticity tensor $C_{mn}$:

$$\sigma_m = \sum_n C_{mn}\varepsilon_n. \tag{1.1}$$

The elasticity tensor is often reported in literature through the use of theoretical calculations or experimental observations, which makes it a readily available description of how materials behave under strain. It can be used to calculate the Young's modulus $E$ of a material, which takes on a different value along each of the high-symmetry directions. Another use is for calculating Poisson's ratio, the ratio of transverse strain to longitudinal strain for a longitudinally applied load. Chapter 3 demonstrates how $C$ is utilized to calculate Poisson's ratio for ZrSiS. Note that Poisson's ratio has a different meaning in engineering terms, where it refers to the isotropic changes of the dimensions of the material under strain rather than the microscopic high-symmetry directional changes.

### 1.2.2 Recent developments in strain research

The experiments that led to the writing of this thesis were all performed using a thermally compensated piezoelectric strain cell, but the development of this technique is actually quite a recent one [28, 29]. The main method used to apply uniaxial stress to samples prior to 2010 was the anvil cell, which uses pistons to apply a force to a sample through mechanical, hydraulic or pneumatic means [30]. The anvil cell came with its challenges: imperfect mating with the sample would lead to stress concentration, bending, and fracture. To remedy this, samples were made short and wide, though this led to increased stress inhomogeneity. It was difficult to apply electrical contacts due to limited accessibility to the sample faces, the anvil technique requires a lot of equipment, and uniaxial stress magnitude generally appears to be limited to $\sim 0.5$ GPa (typically 0.5 % strain, assuming $E = 100$ GPa and the elastic regime). Still, uniaxial stress experiments performed with the anvil method led to some interesting results. Shifting of superconducting $T_c$ was observed in $YBa_2Cu_3O_7$ [31], $CeIrIn_5$ [32], and $UPt_3$ [33], with in-situ tunability achieved with pistons [34] or with helium-filled bellows [31].

A key catalyst for further development of uniaxial strain techniques was the study of superconductivity in the FeAs plane of Fe-based superconductors [35].

The phase diagram of $Ba(Fe_{1-x}Co_x)_2As_2$ changes rapidly with small amounts of strain [36–38], as seen in chapter 2. The goal was to more easily perform in-situ strain measurements at low temperatures. A new experimental setup was popularized: affixing samples directly on top of piezoelectric actuators [37]. This increased strain homogeneity and made the sample face a lot more accessible. However, drawbacks of this method are the anisotropic and often large differential thermal contraction, and the fact that it limits strain magnitudes to about $\sim 0.01\ \%$ [39].

$Sr_2RuO_4$ provided another strong motivation to further develop uniaxial strain techniques. It has been a popular material in the last decade due to its mysterious superconducting pairing mechanism [40, 41]. With localized regions of higher $T_c$ in defective $Sr_2RuO_4$ samples [42], uniaxial strain measurements were proposed. As consistent and reliable measurements could not be obtained with the use of the anvil method, Hicks *et al.* constructed the piezoelectric-based apparatus that established the foundation for the Razorbill strain cells, whose use is reported in chapter 2 of this thesis [28]. This setup has been the standard for strain research since about 2018.

With this new setup, a number of important discoveries have been made [43]. $Sr_2RuO_4$ was found to display a dramatic increase in $T_c$ with uniaxial stress [44]. Charge order was induced in the underdoped regime of cuprates [45, 46]. Transitions between different non-trivial topological phases were induced by uniaxial stress in $ZrTe_5$ and $HfTe_5$ [47, 48]. In $WTe_2$, an extremely large magneto-elastoresistance was observed due to its semimetallic band structure with various effective masses near $E_F$ [49]. To this day, new experimental schemes are being developed to improve the homogeneity and accommodation of the thermally compensated strain devices for a larger amount of experimental probes, such as spectroscopy, high magnetic fields, ultra-high vacuum, low-temperature scattering techniques, and electronic transport.

## 1.3 Quantum oscillations

Quantum oscillations (QOs) are an excellent probe of the electronic structure of a material. When a magnetic field is applied to a solid, the trajectories of electrons carrying a current are bent due to the Lorentz force, generally leading to a resistance

increase called the magnetoresistance. The electrons move in a helical motion perpendicular to $B$ with the cyclotron frequency

$$\omega_c = \frac{e|B|}{m_c}, \tag{1.2}$$

where $m_c$ is the effective cyclotron mass.

When temperatures are low enough ($T \lesssim \hbar\omega_c/k_\mathrm{B}$) and magnetic fields sufficiently high ($\omega_c\tau \gg 1$, where $\tau$ is the mean free time between electron scattering events), electronic states are quantized into Landau tubes in $k$ space [50]. The cross-section of the tubes on which the electrons orbit perpendicular to $B$ is $a = (n + \varphi)2\pi eB/\hbar$, where $n$ is an integer and $\varphi$ is a phase factor dependent on band structure characteristics [51, 52]. As $B$ is increased, $a$ becomes larger as well, eventually leading to Landau tubes passing through the Fermi surface. When a tube passes through an extremal area on the Fermi surface, the local density of states (DOS) will reach a minimum or a maximum, leading to changes in the electrical resistivity (Shubnikov-de Haas effect, SdH) and magnetization (de Haas-van Alphen effect, dHvA) as a result. Continuing to increase $B$ will cause more Landau tubes to pass through the Fermi surface extrema with changes observable periodically in $1/B$, hence the term quantum oscillations. The frequency of the oscillations is directly proportional to the extremal area of the Fermi surface $A$ that corresponds to the affected orbits, via

$$F = \frac{\hbar A}{2\pi e}, \tag{1.3}$$

known as the Onsager relation.

In practice, and particularly in Dirac semimetals and CDW systems, materials often have a Fermi surface that consists of multiple different carrier pockets. This means that a number of different frequencies can be observed in the oscillatory resistivity at the same time. After removing the magnetoresistance background, one can perform a fast Fourier transform (FFT) to analyze the oscillations and find out which frequencies are present. When coupled with a rotating magnetic field direction, the Fermi surface can be mapped out experimentally [53]. In some cases, Fermi surface pockets are separated by a very small gap in $k$ space with its extremal orbits in the same plane. When a quasiparticle orbits around one pocket and has not yet scattered, it is able to tunnel through the gap and orbit around the neighbouring pocket. The total orbit frequency is then the sum of the two pockets if

their character is the same (electron-electron pockets or hole-hole pockets) or the difference if they have opposite character. This tunneling effect is known as magnetic breakdown (MB), and is only possible if $B$ is sufficiently large enough, with the required magnitude depending on the size of the gap between the pockets.

Measuring QOs at higher temperatures will lead to smaller oscillation amplitudes. This is because the minima and maxima reached by the DOS will be less pronounced, which translates to a less abrupt depletion of available states as the Landau tubes pass through the Fermi surface extrema. The amplitude size reduction is directly related to $T$ and $m_c$, the latter of which defines the separation between adjacent tubes. $T$-dependent QO data can therefore be an excellent way to acquire information about the $m_c$ of quasiparticle orbits in the material.

In this thesis, we make use of the SdH effect in most notably chapter 3 and chapter 5 to elucidate strain effects on the Fermi surface and quantum mobility of those materials.

# 2 Experimental techniques

We begin this chapter with a description of the experimental details of uniaxial strain measurements using the Razorbill CS1x0 strain cells. Then, we briefly go over our techniques used for measuring sample resistance and the determination of crystal orientation. The chapter ends with information about two cryogenic setups we used to acquire our data, one being the Quantum Design Physical Property Measurement System at the Van der Waals-Zeeman Institute in the UvA's Institute of Physics and the other being the high magnetic field setup at the High Field Magnet Laboratory in Nijmegen.

## 2.1 Uniaxial strain measurements

We used Razorbill CS100 and CS120 uniaxial strain cells to perform all of the strain studies described in this thesis. The Razorbill website provides users with a collection of comprehensive user guides already [54], so this section will limit itself to a quick overview of the essential basics while providing information about the unique specifics of our experiments.

### 2.1.1 Principle of operation

Originally, uniaxial strain experiments were performed by directly mounting samples on top of stacks made of piezoelectric crystal. Extending or shortening the stacks is achieved by applying a positive or negative voltage to them using a power supply. The problem with using piezoelectric crystals in this uniaxial strain setup is that they expand along their poled direction when cooled. This can cause a differential thermal expansion between the strain cell and the sample, preventing the sample from being held at zero strain during the cooling process. Razorbill strain cells possess a symmetric arrangement of piezoelectric stacks that cancels out the thermal expansion of the stacks and allows the sample to remain unstrained. Long stacks provide access to relatively large strains, with the CS100 and CS120 typically reaching values of $\pm 0.3\%$ and $\pm 0.6\%$ strain at 2 K, respectively.

Fig. 2.1 shows a simplified sketch of the CS100 and demonstrates the manner in which temperature-compensated uniaxial stress is applied. Extending the outer stacks and contracting the inner stack will apply tension (c), while the opposite will apply compression (d). Meanwhile, thermal expansion affects the piezoelectric stacks in the same way, resulting in a net zero movement applied to the sample (b).

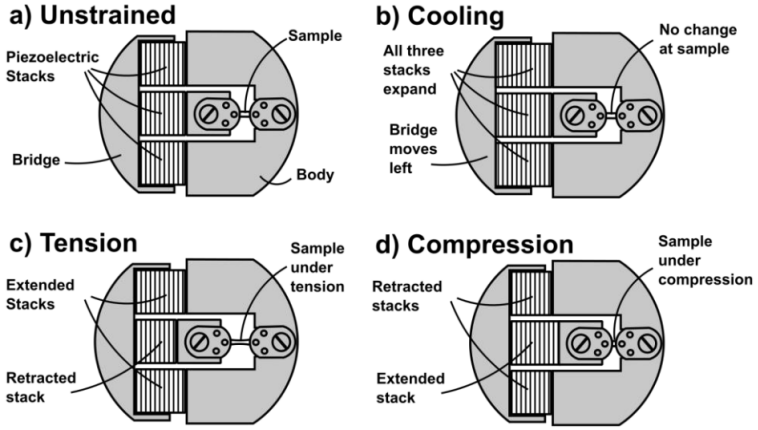


**Figure 2.1.** The principle of operation of the CS100 strain cell. Displacements are not to scale. Adapted from Ref. [55].

In Razorbill strain cells such as the CS100 and CS120, displacement applied to the sample that is collectively caused by the piezoelectric stacks can be measured indirectly. A capacitance value is measured by a parallel-plate capacitive sensor inside the cell. The sensor is connected to an Andeen-Hagerling 2700A capacitance bridge with a resolution of 0.8 aF at a frequency of 1 kHz. The capacitance is used to calculate the displacement through the following formula:

$$d = \frac{\alpha}{C - C_p} - d_0, \tag{2.1}$$

where $d$ is the applied displacement in $\mu$m, $C$ the measured capacitance in pF, and $\alpha$, $C_p$ and $d_0$ are parameters specific to every cell. See Fig. 2.2 for an example of a capacitance curve used in this work. The capacitance sensor is slightly temperature dependent, and so too the value for $d_0$. This is trivial when performing strain measurements at constant temperature, as $d_0$ can simply be determined using Eq. 2.1 by taking $d = 0$ and the value for $C$ at zero strain. The change in $d_0$ of the sensor is generally less than 1 fF between 50 and 2 K, meaning that for temperature sweeps in this region the temperature dependence can be neglected. However, when performing temperature sweeps with a larger range than this the temperature dependence of $d_0$ should be taken into account.

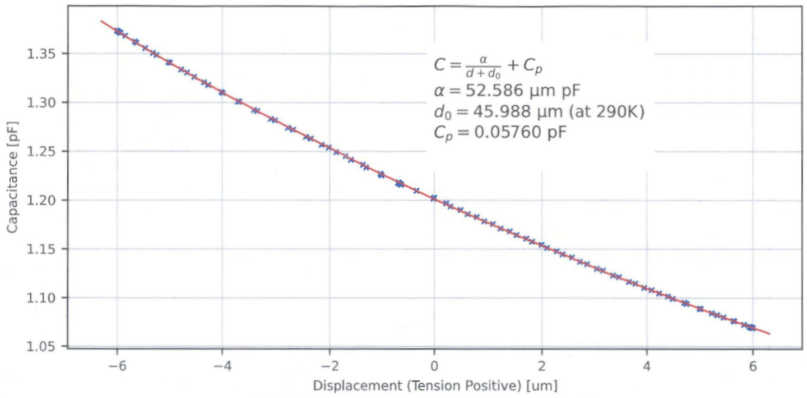


**Figure 2.2.** The capacitance curve of cell CS100 #0293. The formula describing the curve and the cell-specific parameters are listed inside the graph. Provided by Razorbill.

### 2.1.2 Sample and cell mounting

A detailed guide to mounting samples on the CS1x0 strain cells is available on the Razorbill website as application note AP005 [56]. In this work, small pieces of insulated copper wire have been used as epoxy thickness spacers with their thickness depending on the sample and sample plate spacer thicknesses. The epoxy used is Araldite Ultra Strong [57], with a working time of 90 minutes and a full-strength curing time of 14 hours. With the choice between six sets of spacers, each with a different thickness, the sample was always given 30 to 50 $\mu$m wiggle room on both its bottom and top side.

Fig. 2.3 shows a CS100 strain cell mounted with a black WP100 wiring platform and a sample of $BaFe_{1.95}Co_{0.05}As_2$ between titanium sample plates. Small pieces of double-sided tape are used to keep the 30 $\mu$m diameter gold wires in place.

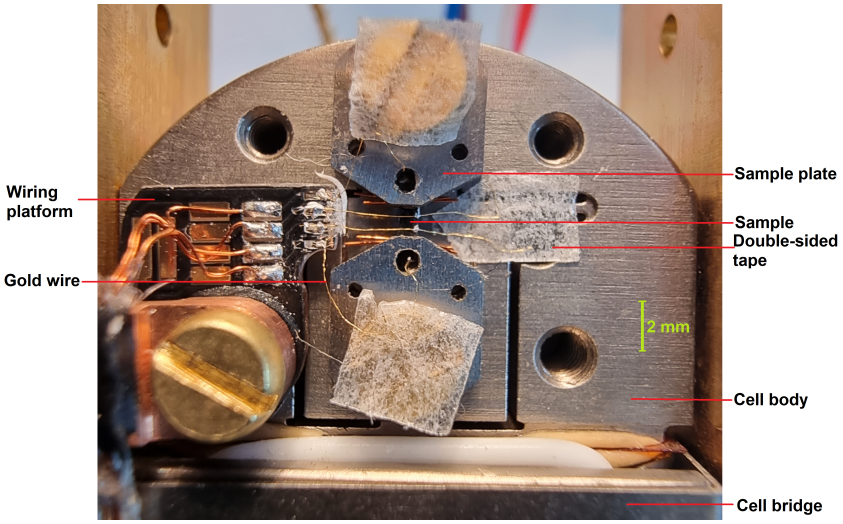


**Figure 2.3.** An example of a mounted CS100 strain cell.

Fig. 2.4 shows a Physical Property Measurement System (PPMS) multifunction probe adapted for use with the CS100 and CS120 strain cells. The CS100 can be mounted in a way in which the magnetic field direction of the PPMS is aligned parallel or perpendicular to the long axis of the mounted sample, while the CS120 only allows for a parallel field direction. The cell power supply connectors (beige, on the far left in Fig. 2.4) and the MMCX connectors (micro-miniature coax, brass) for the capacitance are attached to their probe counterpart. Additionally, the wiring platform is plugged in, allowing for contact between the sample and the PPMS measuring instruments. Fig. 2.4 shows an improvised wiring platform, but since after it broke down Razorbill WP100 wiring platforms have been used.

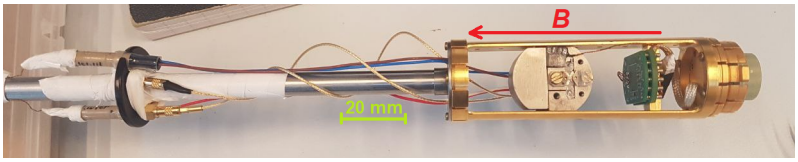


**Figure 2.4.** A PPMS multifunction probe mounted with the CS100 cell. In this configuration the magnetic field $B$ is applied parallel to the strain direction.

### 2.1.3 Operating the cell

The CS1x0 datasheet gives a comprehensive description of how to operate the strain cells [54]. A typical resistivity measurement would go as follows. After having properly mounted the cell into the probe, the probe is inserted into the PPMS. The PPMS is closed and the sample chamber is purged of air before being filled with 10 mbar of helium exchange gas. If the sample shows an appropriate resistivity it means the sample contacts are working as intended, the cables linking the cell to the capacitance bridge and power supply can now be connected. In order to make sure the capacitance can be read out a few readings are done. This is done by running a program that reads out the capacitance every second (software written in Python). Next, the RP100 power supply main switch is turned on (for the manual see [58]). The RP100 is operated using the accompanying Razorbill power supply software tool which allows for control of the inner and outer stack voltages of the cell. Stack slew rate – the change of voltage per unit of time – is always set to 1 V/s.

If everything works as desired, the temperature of the chamber can be lowered to the planned point with a maximum rate of 10 K/min. Here, the zero-strain capacitance value should be recorded to later calculate $d_0$. If a temperature or field sweep is going to be performed at a different strain amount, the voltages must be adjusted in the Razorbill software tool. Once the new voltages are reached, the capacitance is recorded again to later calculate $d$. Note that the capacitance may drift slightly after the voltages have stopped slewing. It is recommended to wait about 1 minute for the capacitance to stabilize before starting a measurement sweep. If the cell is functioning correctly, the remaining drift in $C$ will be negligibly small. A small hysteretic effect in $C$ with changing voltages may also be observed. Important to remember here is that the value of $C$ compared to its value at zero strain is ultimately what determines the amount of displacement that is applied to the sample.

Once finished, the voltages on the stacks are set to zero and the cryostat sample space is warmed back up to room temperature, after which the RP100 is turned off and the cables can be disconnected.

### 2.1.4 Limit of displacement

There are three factors that limit the amount of displacement that can be applied to a sample. The first limiting factor depends on the temperature. For the CS100

and CS120, operating at 2 K means the achievable displacement is about twice as small as at room temperature. This reduction with temperature can to some extent be offset with the application of larger voltages to the piezoelectric stacks, as a decreasing temperature increases the maximum allowed applied voltage $V_{\text{max}}$ (see Fig. 8 of the CS1x0 datasheet [54]). In order to perform temperature sweeps at constant strain levels, we wrote a Python script that continuously adjusted $V_{\text{max}}$ using temperature read-outs.

The second limiting factor depends on the shortest distance $L$ between the two glued ends of the sample. With $\varepsilon_{\text{maxdisp}} = d_{\text{max}}/L$ and with $d_{\text{max}}$ being a fixed amount at a fixed temperature, it leaves the user only the $L$ value to play with. Shorter samples allow for higher achievable strains.

The third limiting factor depends on the spring constant of the sample. The stroke of the cell is divided between force and displacement. How much of each depends on the ratio of the spring constant of the cell to the spring constant of the sample plus sample mounts. If a sample is too stiff, the force will overload the cell and the stroke of the cell will go into deforming itself. Because some sample materials are quite complex their spring constant can be difficult to know. The spring constant of a sample in the elastic limit can be estimated as $k_s = EA/L$, where $A$ is the cross-sectional area of the sample and $E$ is its Young's modulus, which is around 100 GPa for most metals and ceramics. A typical cross section of samples used in this work is less than $0.1\ \text{mm}^2$. Using Figs. 1 and 2 from the Razorbill CS1x0 datasheet (Ref. [54]) and assuming $T = 1$ K, the safe limit of a sample spring constant is about 20 N/$\mu$m for the CS100 and 10 N/$\mu$m for the CS120. Using these values and solving for $L$ gives a safe minimum of $L = 0.5$ mm for the CS100 and of $L = 1$ mm for the CS120. With $L$ values in this work easily exceeding 1 mm, there is no risk of overloading, and therefore full voltage amounts can be applied. However, it must be noted that these are approximations; $E$ can greatly vary depending on strain direction, and some stiff materials have a relatively high $E$ such as $Sr_2RuO_4$ with $E = 176$ GPa [28]. Lastly, the titanium sample plates should technically be taken into account when calculating the spring constant that relates to the datasheet figures, as they are in series with the sample and collectively working on the cell. They are omitted here, as they have a much higher spring constant than the sample, which means their effect on the combined spring constant is very small. In reality the sample plates allow for samples with a slightly higher spring constant to be used safely in the strain cells.

### 2.1.5 Strain inhomogeneity

Strain inhomogeneity has presented a notorious technical challenge in past uniaxial strain experiments. An indication of strain inhomogeneity can be the broadening of phase transitions as uniaxial strain is increased [32, 59–61]. Samples with high length-to-width ratios can help obtain better strain homogeneity. Fig. 2.5 shows a schematic view of one side of a mounted sample, highlighting the insulating epoxy fully surrounding the sample end. This 'sandwiched' sample mounting setup helps reduce strain inhomogeneity significantly, as demonstrated by finite element simulations in the literature [28, 38, 62]. These studies also show that strain homogeneity is excellent in the center of the sample where the voltage contacts are located for resistance measurements, assuming the sample has been properly aligned with the strain direction. Additionally, strain relaxation effects in the epoxy layers have been estimated, finding a strain transfer ratio between 70 and 90 %, mostly depending on epoxy layer thickness [38, 62]. The uncertainty of this ratio is significant and epoxy layer thickness is somewhat difficult to determine. Therefore, epoxy strain relaxation remains one of the key factors in the determination of the uncertainty of the displacement actually experienced by the sample itself. In this work, epoxy strain relaxation is omitted and full displacement values measured by the capacitive sensor are used for the determination of strain values, generally resulting in a small overestimation of uniaxial strain.

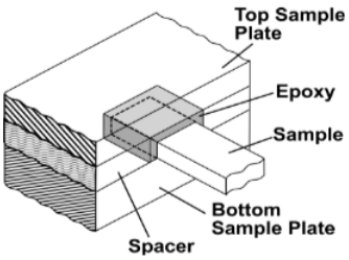


**Figure 2.5.** The 'sandwich' sample mounting method, offering excellent strain homogeneity. Adapted from Ref. [54].

### 2.1.6 Differential thermal expansion

When performing low-$T$ measurements, the difference in thermal expansion (contraction) between the titanium strain cell and mounted single crystalline sample results in the sample being strained when no voltages are applied. The thermal expansion effect of titanium is relatively minor compared to that of aluminium, copper and steel. When the temperature of titanium is lowered from room temperature to 4 K, its linear dimensions are reduced by 0.15 %. This is identical to that of $Ba(Fe_{1-x}Co_x)_2As_2$ along its $a$ axis [63], a benchmarking material used in this work. It differs, however, from the thermal expansion of bismuth or ZrSiS. The $a$ axis of bismuth is reduced by 0.28 % when cooling from room temperature to 4.2 K [64], which would effectively result in a uniaxial tension of $0.28\,\% - 0.15\,\% = 0.13\,\%$ experienced by the bismuth sample. In the case of ZrSiS, the $a$ axis is reduced by 0.08 % when cooling from room temperature to 100 K [53, 65], resulting in a uniaxial compression of 0.07 %. These changes in axis length are calculated from temperature-dependent lattice constant values, which have been measured in previous studies through strain dilatometry, X-ray diffraction and neutron diffraction [53, 64, 65]. With the sample strained through differential thermal expansion, the new zero-voltage strain value essentially becomes the starting point from which the sample can be uniaxially tensioned and compressed with the usual displacement. This means larger tensile and compressive strains can be achieved for bismuth and ZrSiS, respectively.

If this means the desired strain range is no longer achievable, there are multiple ways to remedy this. A shorter sample or a larger strain cell would facilitate a larger strain range. Straining a mounted sample at room temperature, making use of the greater available strain range, tends to move the zero-voltage point slightly towards the compressive or tensile direction, depending on the way the sample was strained. Alternatively, voltage can be applied to the piezoelectric stacks after the mounting process is finished but with the epoxy just applied. After the epoxy has cured, reducing the voltage back to zero will induce a uniaxial strain that ideally cancels out the amount that would have been experienced by the sample at the desired measuring temperature. This method is quite hazardous as improper handling of the cell at high voltages can shock the user. Lastly, sample plates of a material other than titanium can be used. Copper-based alloys will tension the sample more, while molybdenum or tungsten plates will compress it more.

The main goal of this work is to perform qualitative and explorative measurements. Without having performed our own lattice constant measurements, with the data of temperature-dependent lattice constant information often being unavailable, and with the compensating of differential thermal expansion effects being quite challenging and unreliable, it was decided these effects would be omitted in the analysis of the data. However, strain ranges used have generally been maximized in order to probe as much of the phase diagrams of materials as possible.

### 2.1.7 Bowtie mounting method

The bowtie mounting method refers to the use of a flat, bowtie-shaped piece of material as a platform on which a sample can be glued, as shown in Fig. 2.6. The bowtie is generally made out of titanium and is mounted on a Razorbill cell instead of the usual sample plates. Spacer rings are used to raise the bowtie sightly, preventing the screws from bottoming out. The shape of the bowtie concentrates the applied force, resulting in larger strains at the neck. In this setup, the sample length $L$ is not taken as the distance between glued ends like in the conventional method, but is instead a characteristic parameter of the platform itself referred to as $L_{\text{eff}}$. The bowties used in our work are provided by the research group of Steffen Wiedmann from Radboud University. They are made of titanium and have an $L_{\text{eff}}$ of 3.4 mm, as determined by Park *et al.* through $\varepsilon_{\text{disp}} = d/L_{\text{eff}}$ with strains measured optically and through finite element analysis calculations [66]. This is the room temperature value, but $L_{\text{eff}}$ is not expected to change significantly with cooling to 2 K. $L_{\text{eff}}$ can however vary depending on where exactly the ends of the bowtie are fastened to the cell, but as this distance between the screws is a constant in the Razorbill cells, and as the neck of the bowtie is consistently centered, this variation should not cause significant deviations. The $L_{\text{eff}}$ is also used when assessing the spring constant of the bowtie. Estimations by Park *et al.* show that the bowtie can safely be used with the CS100 and CS120 cells [66].

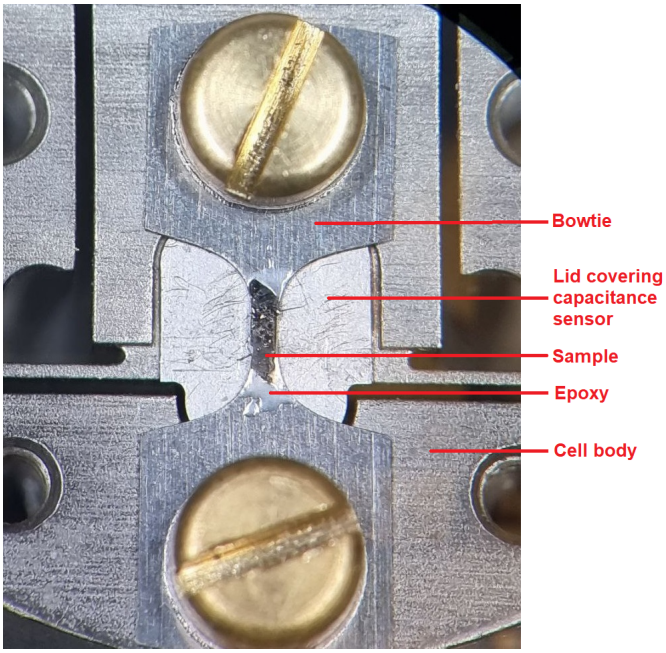


**Figure 2.6.** A titanium bowtie attached to a CS100 strain cell, mounted with an $IrTe_2$ sample. The bowtie is 17 mm long, 8 mm wide and 0.2 mm thick, with its neck 0.5 mm wide.

As the bowtie is made out of titanium and the sample must be electronically isolated from the cell, an insulating layer of epoxy is necessary. This epoxy is needed to attach the sample to the bowtie regardless, but will induce an uncertainty in the amount of strain experienced by the sample. To characterize the strain transmission from the bowtie to the sample, the strain transmission length $\lambda$ is used [28]: $\lambda = \sqrt{Ct_s t_e/G}$, where $C$ is the relevant elastic modulus of the sample, $t_s$ is the sample thickness, $t_e$ is the epoxy thickness, and $G$ is the shear modulus of the epoxy. Assuming the length of the sample is much greater than $\lambda$, high strain homogeneity and proper strain transmission is achieved within the sample when the width $w$ of the sample is either much less or much greater than $\lambda$. Inserting typical values for the parameters with $G = 1.7$ GPa, $C = 100$ GPa, and $t_s = t_e = 10$ $\mu$m gives $\lambda = 76$ $\mu$m [66]. With the $w$ of our samples being around 500 $\mu$m, it is clear that small epoxy and sample thicknesses are important in bowtie measurements, as

a 100 $\mu$m sample thickness would already lead to a $\lambda$ of 243 $\mu$m, nearing the sample width. Ideally, sample thickness is reduced as much as possible through cleaving, in order to grant wiggle room to the other parameters. The decision to cleave thinner or not depends on the availability of samples, as it may break the sample.

The elastic limit of grade 2 titanium used in this work is 0.2 %. Higher strains will cause non-elastic deformation and can have effects on the strain transmitted to the sample, reducing reproducibility. This limits the amount of strain that can be applied to a sample using the CS120 at room temperature. At 2 K though, the CS120 can only apply 6 $\mu$m displacement, keeping strains within the elastic regime of the bowtie.

### 2.1.8 $Ba(Fe_{1-x}Co_x)_2As_2$ as a benchmark material

$Ba(Fe_{1-x}Co_x)_2As_2$ is an underdoped iron pnictide that has been established as a highly strain-tunable material through a number of uniaxial strain studies performed in the past [38, 62, 67, 68]. While hydrostatic pressure lowers the Néel temperature $T_N$ of $Ba(Fe_{1-x}Co_x)_2As_2$ when $x \sim 0.05$ [38], uniaxial compression along its tetragonal [110] axis actually raises it [38, 62, 68]. It was also found that the superconducing transition temperature $T_c$ is lowered with uniaxial strain along the [110] axis. These properties, combined with the availability of crystals at the Van der Waals-Zeeman Institute, made $Ba(Fe_{1-x}Co_x)_2As_2$ an excellent benchmark material for our uniaxial strain experiments.

Here, we present the results of our uniaxial strain study on $BaFe_{1.95}Co_{0.05}As_2$ strained along the tetragonal [110] axis. Each result is compared to the corresponding result obtained by Malinowski *et al.* [62]. The curves in Fig. 2.7(a) show the temperature dependence of the resistivity as measured by Malinowski *et al.* with strain along the [110] axis ranging from -0.38 % compression to 0.22 % tension. The squares point out the Néel temperature and are obtained by taking the local minima of the first derivatives of the curves. Fig. 2.7(b) and (c) show the data obtained in our work, with the sample under compression and tension, respectively. A clear trend in $T_N$ can be observed, agreeing well with the literature.

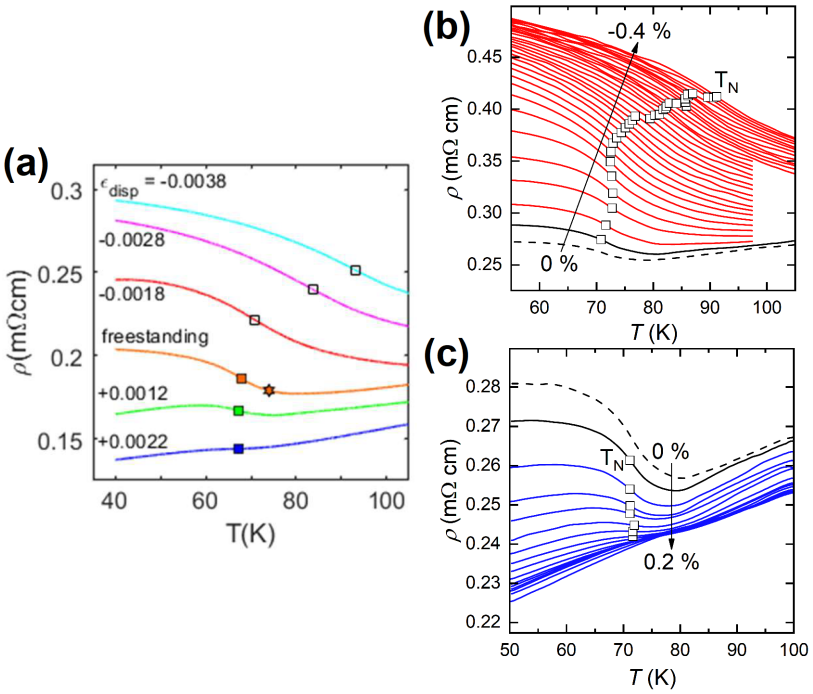


**Figure 2.7.** Temperature sweeps of the resistivity of $BaFe_{1.95}Co_{0.05}As_2$ at varying uniaxial strains along the [110] axis. Squares point out the value of $T_N$ for each curve. (a) shows data obtained by Malinowski *et al.*, (b) and (c) show 10 point average smoothed data obtained in our work. In (b) and (c), the solid black line shows the first measurement at zero strain and the dashed black line shows the last measurement at zero strain. The red (compressive) and blue (tensile) strain resistivity curves show a linear offset as strain departs from zero. The start value and the maximally achieved strain values are indicated. (a) is adapted from the supplemental material of Ref. [62].

The trend is observed more clearly in Fig. 2.8, where the phase diagram of the dependence of $T_N$ on uniaxial strain is displayed. (a) shows data from Malinowski *et al.*, while (b) shows the data of our work.

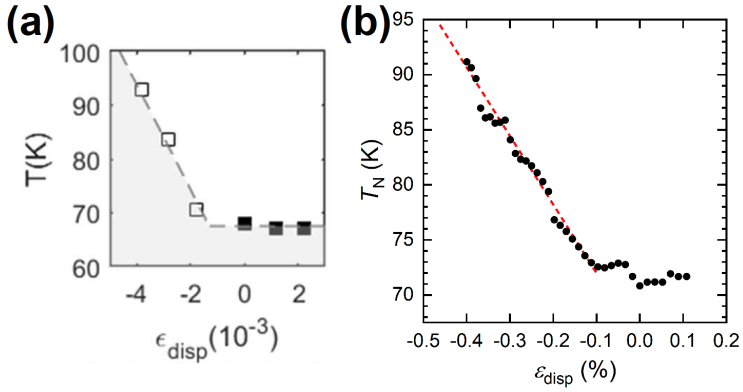


**Figure 2.8.** The $T_N(\varepsilon_{disp})$ phase diagrams for data from Malinowski *et al.* (a) and our data (b). The dashed lines serve as a guide for the eye. (a) is adapted from the supplemental material of Ref. [62].

Fig. 2.9(a) and (b) show the superconducting transition under tension with data from Malinowski *et al.* and our work, respectively. Our data displays what appears to be a double transition, possibly resulting from a doping inhomogeneity. Still, we observe the lowering of the normal resistivity, but it appears our amount of uniaxial strain was insufficient to start observing a significant reduction in $T_c$. This is different for the transition under compression shown in (c) and (d), where we find the expected increase in normal resistivity, but also a significant decrease in $T_c$, in agreement with the data of Malinowski *et al.* The decrease in $T_c$ with compression appears to be smaller in our data (1 K in (d) and 4 K in (c)), but the reduced difference in normal resistivity between the compression curves of the larger strain values is reflected in the literature data. It implies that the difference in strain experienced by our sample compared to that of Malinowski *et al.* is small ($\sim$ 0.1 %) relative to the difference in decrease of $T_c$. The difference in strain is perhaps the result of a difference in differential thermal expansion or epoxy strain relaxation between our experiment and that of the literature. This non-linear strain effect on $T_c$ is something we also observe for $T_N$ close to zero strain (Fig. 2.8).

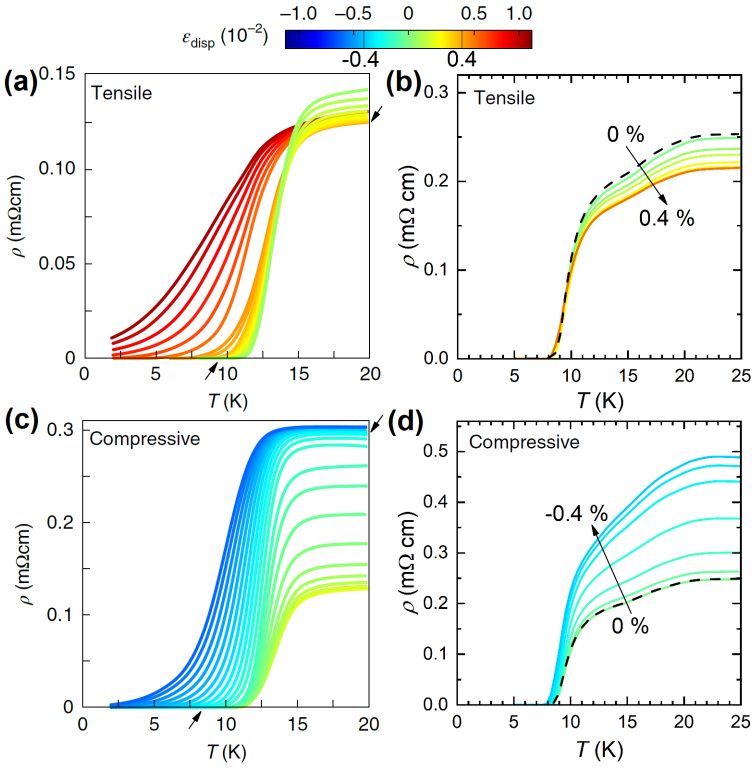


**Figure 2.9.** The superconducting transitions of $BaFe_{1.95}Co_{0.05}As_2$ under uniaxial strain. The small arrows at the normal and superconducting states in the figures of Malinowski *et al.* (a) and (c) point out the curves corresponding to a strain value of $\pm 0.4$ %, which is the highest strain achieved for a curve in our figures (b) and (d). (a) and (c) are adapted from Ref. [62].

With the successful reproduction of the literature data, we conclude that our strain cell and sample mounting method work as intended, and recommend using $Ba(Fe_{1-x}Co_x)_2As_2$ as a uniaxial strain experiment benchmark material.

## 2.2 Other techniques

### 2.2.1 Four-point resistance measurement

All resistance measurements described in this work have been performed using the four-point resistance measurement configuration. This setup involves two voltage contacts between two current contacts. Measuring current and voltage separately this way eliminates the contact and wire contributions to the resistance and provides a more accurate representation of the resistance of the sample. We use RS Pro (or DuPont 4929N) silver conductive paint to create contacts between samples and 30 $\mu$m diameter gold wires. In this work, contacts are placed in a way that the current flow direction is always along a principal axis, often also the strained and long axis of the sample.

A typical DC current value applied to our samples is about 500 $\mu$A. The choice for this value is motivated by the balance between measurement noise and sample heating. A larger resistance $R$ leads to a relatively smaller amount of noise in measured data. Resistivity $\rho$ is a material property, and $\rho = RA/l$ with $l$ being the distance between voltage contacts on the sample. As this means that samples with a larger cross section $A$ will have a smaller $R$, a larger current is necessary as it helps mitigate the noise effects. Contrarily, for long, thin samples a smaller current will suffice. A current that is too large will heat the sample up and can thereby significantly affect important parameters such as the superconducting transition temperature. Samples with a smaller $A$ will heat up faster. Ultimately, a current value high enough to account for noise and low enough to not heat up the sample is desired.

### 2.2.2 Laue X-ray diffraction

Laue X-ray diffraction is a commonly used technique where a broad spectrum beam of X-rays is pointed at a clean, flat surface of a stationary single crystal. Reflected (or 'backscattered') rays result in a diffraction pattern that can be fitted using a program like Clip, OrientExpress or Diamond. This way the orientation of the principal axes of the probed crystal can be determined. We used Laue X-ray diffraction on almost every crystal we studied, as knowing the orientation was critical to performing proper uniaxial strain measurements. The device used was a Diffractis 582 made by Enraf Nonius Delft.

### 2.2.3 Quantum Design Physical Property Measurement System

The Physical Property Measurement System (PPMS) designed by Quantum Design is the cryostat that has been used the most in the research outlined in this work. It consists of a 9 T superconducting magnet and a He-4 pulse tube cryocooler, with a sample chamber temperature range of 1.8 to 400 K. The sample chamber has a diameter of 2.6 cm allowing for the insertion of some types of Razorbill strain cells mounted on a multifunction probe. Twelve built-in electrical leads at the bottom of the sample chamber couple to a number of different probes. More than 20 different measurement options are compatible with the PPMS. The one we used most is the DC resistance option, closely followed by the rotator option. All options integrate seamlessly with the Quantum Design MultiVu software environment. Sequences can be programmed to automate measurement cycles and may be tailored to work with third party programs active on a different PC setup.

### 2.2.4 High magnetic fields

Our measurements on ZrSiS and unstrained $LaO_{0.8}F_{0.2}BiS_{2-x}Se_x$ were performed at the High Field Magnet Laboratory (HFML) in Nijmegen. The lab hosts several large Bitter magnets composed of multiple coils, with each coil made up of stacked plates crafted from a copper-silver alloy. Static magnetic fields of 33 T and even 38 T can be reached, depending on the magnet. The setups have a bore of 3.2 cm which allows the insertion of a $^4$He cryostat. If fitted with a $^3$He system, the cryostat insert supports measurements down to 0.3 K, while a flow cryostat allows for good temperature control for measurements in the range of 1.4 to 300 K. Each cryostat insert fits a probe that may carry a rotator or a Razorbill CS100 strain cell.

# 3 Uniaxial strain effects on the Fermi surface and quantum mobility of the Dirac nodal-line semimetal ZrSiS

ZrSiS has been identified as an exemplary Dirac nodal-line semimetal, in which the Dirac band crossings extend along a closed loop in momentum space. Recently, the topology of the Fermi surface of ZrSiS was uncovered in great detail by quantum oscillation studies. For a magnetic field along the tetragonal $c$ axis, a rich frequency spectrum was observed stemming from the principal electron and hole pockets, and multiple magnetic breakdown orbits. In this chapter we use uniaxial strain as a tuning parameter for the Fermi surface and the low energy excitations. We measure the magnetoresistance of a single crystal under tensile (up to $0.34\,\%$) and compressive (up to $-0.28\,\%$) strain exerted along the $a$ axis and in magnetic fields up to 30 T. We observe a systematic weakening of the peak structure in the Shubnikov-de Haas frequency spectrum upon changing from compressive to tensile strain. This effect may be explained by a decrease in the effective quantum mobility upon decreasing the $c/a$ ratio, which is corroborated by a concurrent increase in the Dingle temperature.

## 3.1 Introduction

When investigating the correlated and topological properties of crystalline materials their Fermi surface is often studied, because knowledge of the low-energy excitations close to the Fermi level can foster a fundamental understanding of the electronic physics at play. In the case of topological matter, Dirac nodal-line semimetals (NLSMs) provide an excellent playground [65, 69–72]. In these systems the valence and conduction bands cross each other in a closed loop (the nodal line) inside the Brillouin zone. The topological character of these materials has been established in quantum oscillation experiments [6, 73–76]. The small density of states near the Fermi level can help shine light on the correlated character, as this is predicted to reduce the screening of the long-ranged Coulomb interaction [77], making NLSMs more susceptible to various types of order such as superconductivity or magnetism [7, 8, 78].

NLSMs have been experimentally investigated in the recent past, for instance $PtSn_4$ and $PbTaSe_2$ [70, 71]. In these two materials the Fermi level is shared by a nodal line and topologically trivial bands. The latter makes it more challenging to search for correlation effects in a topological material, as the quasiparticle behaviour of the crystal is not governed solely by the electronic states on the nodal line. Conversely, in the NLSM ZrSiS the nodal line is the only band feature near its Fermi level. The dispersion of the bands extends linearly for a relatively large energy range (0–2 eV), with only a small gap ($\sim$ 0.02 eV) in the Dirac spectrum as a result of spin-orbit coupling. This gives rise to a cage-like 3D Fermi surface and results in the physical behaviour of ZrSiS being governed by practically only the topological aspects of its electronic structure [72]. This makes ZrSiS a very appealing choice for studying correlated topological matter.

In previous research ZrSiS was studied by means of quantum oscillations (QOs), identifying its extremal Fermi surface cross sections [73–76]. In the $Z$-$R$-$A$ plane, these are the fundamental $\alpha$ and $\beta$ pockets. Subsequent work also includes QOs as a result of magnetic breakdown (MB), and compares them to density functional theory (DFT) calculations [53, 79, 80]. MB occurs in ZrSiS when a sufficiently high magnetic field causes quasiparticles to tunnel between the different fundamental pockets on the nodal line, overcoming the small gap introduced by spin-orbit coupling [50]. In ZrSiS, this gap (and the nodal-line state) is topologically protected by both the mirror- and inversion symmetry of the crystal structure [81]. Recently, the physical behaviour of ZrSiS has been probed using hydrostatic pressure as a tuning

parameter with pressures as high as 57 GPa [82]. The observed changes in the Fermi surface properties suggests the presence of a pressure-driven topological quantum phase transition [81–83]. Closely related to hydrostatic pressure, another powerful experimental tool for exploration of the topological properties of band structures is the application of uniaxial pressure. In the elastic regime of the sample, the applied stress relates linearly to the resulting strain. This uniaxial strain response of materials that have exceptional topological band-structure features has been of great interest in the past few years. Strain has been used to demonstrate tunability of Dirac states [84, 85], shift phase transition temperatures of materials [38, 62, 86], induce topological phase transitions [47, 86, 87], and lift the degeneracy of Fermi surface pockets [88]. As regards ZrSiS, electronic structure calculations have predicted significant effects of uniaxial strain on the Fermi surface, notably a large increase of the MB gap. [89] These calculations have been made for tensile strains between 1 and 4 %, but only for strains along the $c$ axis. We remark, such high strain values are difficult to realize experimentally.

In this chapter, we report on the effect of uniaxial strain on the Fermi surface of ZrSiS. A single crystal of ZrSiS was mounted onto a Razorbill CS100 cryostrain cell and its magnetoresistance (MR) was measured as a function of temperature under uniaxial stress applied along the $a$ axis in magnetic fields up to 30 T. Together with a related study on ZrSiSe [9], this is the first experiment in which a CS100 strain cell was used to measure a sample at fields this high. Strain-induced changes in the Shubnikov-de Haas (SdH) oscillations present in the MR data were analyzed using fast Fourier transforms (FFTs) and the resulting frequency spectra at each temperature- and strain value were compared. We clearly identify the $\beta$ peak at 418 T, which has been absent in previous SdH studies [53, 79]. Moreover, the contribution of the fundamental $\beta$ orbit to the conductivity of the sample relative to the contribution of the $\alpha$ orbit is found to be enhanced in the uniaxially compressed state. Compressive strain also increases the FFT amplitudes of the MB peaks, with some of the linear combinations of fundamental frequencies only being found in the data of the compressed state. In each case, tensile strain demonstrates the opposite effect. DFT-based band structure calculations for strain along the $a$ axis corroborate our results.

## 3.2 Experiment

ZrSiS single crystals were grown in a carbon-coated quartz tube using stochiometric amounts of each element together with a small amount of $I_2$. The tube was then vacuum sealed and heated to 1100 °C for one week. The applied temperature gradient was 100 °C. After extracting the crystals they were wrapped in Zr foil and annealed under high vacuum at 600 °C for three weeks. The crystal structure and composition were verified using powder X-ray diffraction and energy-dispersive X-ray spectroscopy (EDX).

The crystals were cut into small bar-shaped samples with dimensions of 1–1.5 $\times$ 0.2 $\times$ 0.1 mm$^3$ ($a \times b \times c$ axis). Thin titanium and gold layers were evaporated on four lines across the samples in order to create proper contact pads for the wiring. A sample was mounted on the strain cell (CS100, Razorbill Instruments Ltd [28, 54]) using Araldite glue, in a way that uniaxial stress could be applied along the $a$ axis and a magnetic field could be applied along the $c$ axis. For a detailed description of the mounted cell set-up see Fig. 3.5 of appendix 3.A. Four 25 $\mu$m gold wires were arranged according to the four-point probe method to measure the resistance with a current along the $a$ axis. The wires were connected to the contact pads on the sample using DuPont 4929N silver conductive paint. Sample resistance was measured with a Stanford Research Systems SR865A Lock-In amplifier at a constant current excitation of 2 mA. The uniaxially applied stress was measured via a precalibrated capacitive sensor inside the strain cell using an Andeen-Hagerling 2700A capacitance bridge. The uniaxial strain $\varepsilon_{\text{disp}} = \Delta L/L$ experienced by the sample was then derived from the applied displacement $\Delta L$ (a few $\mu$m) and the shortest distance $L$ between the two glued ends of the sample (see Fig. 3.5 of appendix 3.A). In-depth information on strain homogeneity, limitations and reading errors can be found in the Razorbill CS1x0 Product Datasheet [54].

All transport measurements were performed in a $^4$He bath cryostat with a base temperature of 1.4 K. The magnetic field sweeps were carried out using a resistive Bitter magnet at the High Field Magnet Laboratory (HFML) at Radboud University with the magnetic field direction along the $c$ axis of the crystal.

## 3.3 Results and Analysis

The sample's longitudinal resistance $R_{xx}$ is shown against temperature $T$ in Fig. 3.1(a). This curve taken upon cooling reveals a residual resistance ratio (RRR) value of 36, which proves to be sufficiently high for observing pronounced SdH oscillations. Fig. 3.1(b) shows $R_{xx}$ against sample strain $\varepsilon_{disp}$ at $T = 1.4$ K and $B = 5$ T. Negative strain values correspond to compression, while positive strain values correspond to tension. Uniaxial stress was applied along the $a$ axis. The data show that there is no significant change in $R_{xx}$ with strain. This implies that there is no elasto-magnetoresistance (EMR) present in this material under these conditions. A set of MR data is shown in Fig. 3.1(c), consisting of six individual field sweeps at different strain values along the $a$ axis (curves are offset for clarity), with $T = 1.4$ K and $B \parallel c$. The chronological order of the sweeps starts with a zero strain measurement and is followed by the increasing compression measurements, shown in red. Then, the increasing tension measurements in blue were performed, ending with another zero strain measurement (dashed black line). Both compressive and tensile strain demonstrate a systematic evolution in curve shape with strain. The curves of the two zero strain measurements overlap well, which indicates having stayed within the elastic strain regime of the sample. In Fig. 3.6 of appendix 3.B the difference in $R_{xx}(B)$ between the strained curves and the zero strain curve shows the tunability of the quantum oscillations through the use of uniaxial strain along the $a$ axis.

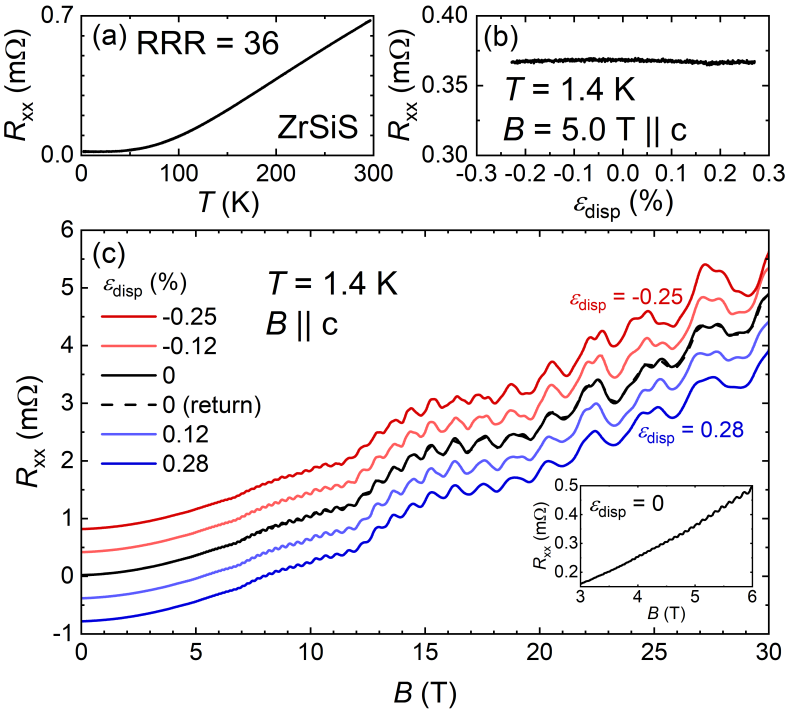


**Figure 3.1.** (a) Cool down $R(T)$ curve. The longitudinal resistance $R_{xx}$ in mΩ of the ZrSiS sample against temperature $T$ in K. The residual resistance ratio of the sample is 36. (b) Longitudinal resistance $R_{xx}$ in mΩ against the applied uniaxial strain $\varepsilon_{disp}$ along the $a$ axis [100], at 1.4 K and 5 T. Negative strain means compression, positive strain means tension. (c) Longitudinal resistance $R_{xx}$ in mΩ against the applied magnetic field $B$ in Tesla for negative and positive strain at 1.4 K. The curves have been offset for clarity, with the strain for each curve going from negative to positive in a descending fashion. A final zero strain measurement (dashed black line) falls onto the solid black line and verifies having stayed within the elastic regime. The inset shows SdH oscillations of the zero strain measurement being present at $B$ = 4 T.

In order to investigate the temperature dependence of the MR at different strain values a second run of strain measurements was performed, the raw MR data of which are shown and discussed in Fig. 3.7 of appendix 3.C. In Fig. 3.2(a–c) the derivative of these MR with respect to the inverse magnetic field $1/B$ is shown against $1/B$ in $\mathrm{T}^{-1}$, at the minimum (1.4 K) and maximum (8.0 K) temperature

and at strain values of $\varepsilon_{\text{disp}} = -0.28\,\%$, zero and $0.34\,\%$. Here the other temperature curves ($2.2\,\text{K} \leq T \leq 6.0\,\text{K}$) have been omitted to more clearly demonstrate the temperature and strain effects. The FFT analysis of the corresponding derivatives at all measured $T$ is shown in Fig. 3.2(d–f). The FFT magnetic field range was chosen to be $5 - 30$ T and the Hann window function was used. The frequency peaks in Fig. 3.2(d) have been labeled using the fundamental quasiparticle orbits $\alpha$ and $\beta$ (shown in the inset), their harmonics and their linear combinations [53]. Low-frequency orbits ($\delta, \gamma$) have also been identified, but the focus remains on the higher frequencies. Interestingly, the FFTs show a clear enhancement in frequency peak structure towards compressive strain $\varepsilon_{\text{disp}} = -0.28\,\%$, whereas a tensile strain of $\varepsilon_{\text{disp}} = 0.34\,\%$ shows the opposite effect. Frequency peaks that are visible at multiple strain values are linked with vertical gray dashed lines. Similar features are observed in the FFTs of the derivatives of the MR data of Fig. 3.1c. See Fig. 3.8 of appendix 3.D.

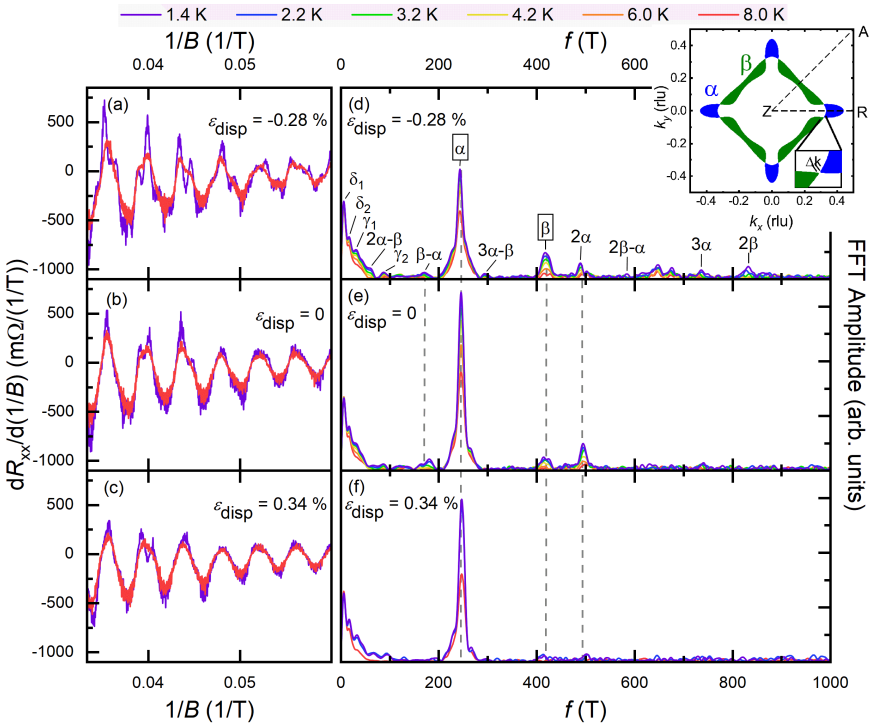


**Figure 3.2.** (a–c) Derivative plots of $R_{xx}$ against $1/B$ at varying $T$, for $0.28\,\%$ compression, zero strain and $0.34\,\%$ tension. Only the $T$ curves 1.4 K and 8 K are shown here for clarity. (d–f) FFT plots of the derivative data at corresponding $T$ (indicated by the different colors) and strain values. The identification of the peak frequencies is given in (d). Vertical dashed lines link peaks of orbits in the $Z$-$R$-$A$ plane under compression to those at different strain values, if visible. The inset shows the two distinct electron (green, $\beta$) and hole (blue, $\alpha$) pockets in the $Z$-$R$-$A$ plane of ZrSiS, in the zero strain state. These pockets are separated by a small gap in momentum space $\Delta k$ that arises due to spin-orbit coupling. Inset figure taken from Ref. [53], courtesy of the authors.

Fig. 3.2 evidently shows a large change in proportion of the FFT amplitude between the two fundamental frequencies in the $Z$-$R$-$A$ plane. We also note that under a uniaxial compression of $\varepsilon_{\text{disp}} = -0.28\,\%$ the $\alpha/\beta$ FFT amplitude ratio has a value less than half (4.5) of that compared to the zero strain case (9.8).

Next we derive the quasiparticle cyclotron mass $m_c$ of the fundamental frequencies $\alpha$ and $\beta$ for different magnetic field ranges. We use the standard thermal

damping factor of the Lifshitz-Kosevich formula $R_T = X/\sinh(X)$, where $X = 14.69 m_c T/\langle B\rangle$ [50, 90], with an average field $\langle B\rangle = 2/(B_{min}^{-1} + B_{max}^{-1})$. The results are reported in Table 3.1. For the full range, $B = 5$ – 30 T for $\alpha$ and 10 – 30 T for $\beta$, the zero strain $m_{c,\text{full range}}$ values correspond well to those of previous research [53, 75, 79]. The compressive strain mass values appear to be slightly lower than at zero strain, but given the error margin this is not a significant difference.

**Table 3.1.** Fundamental orbits and their frequencies at zero, $-0.28$ % compressive and $0.34$ % tensile strain. Cyclotron masses in $m_e$ acquired for different magnetic field ranges. Full range is 5 – 30 T for the $\alpha$ and 10 – 30 T for the $\beta$ pocket. The $m_{c,\text{varying }\langle B\rangle}$ values are taken from the field-dependent study (see text and Fig. 3.3). The entries in the rightmost column are obtained in the range 4 – 11 T and are used for the determination of $T_D$ (see text).

| Orbit | $f$ (T) | $m_{c,\text{full range}}$ | $m_{c,\text{varying }\langle B\rangle}$ | $m_{c,4-11\text{ T}}$ |
|---|---|---|---|---|
| $\alpha_0$ | 245 | $0.15 \pm 0.01$ | $0.20 \pm 0.04$ | $0.16 \pm 0.01$ |
| $\alpha_{\text{comp}}$ | 243 | $0.13 \pm 0.01$ | $0.18 \pm 0.04$ | $0.16 \pm 0.01$ |
| $\alpha_{\text{tens}}$ | 247 | $0.15 \pm 0.01$ | $0.21 \pm 0.02$ | $0.16 \pm 0.01$ |
| $\beta_0$ | 418 | $0.42 \pm 0.05$ | $0.51 \pm 0.10$ | – |
| $\beta_{\text{comp}}$ | 419 | $0.39 \pm 0.02$ | $0.40 \pm 0.06$ | – |
| $\beta_{\text{tens}}$ | 415 | – | $0.53 \pm 0.03$ | – |

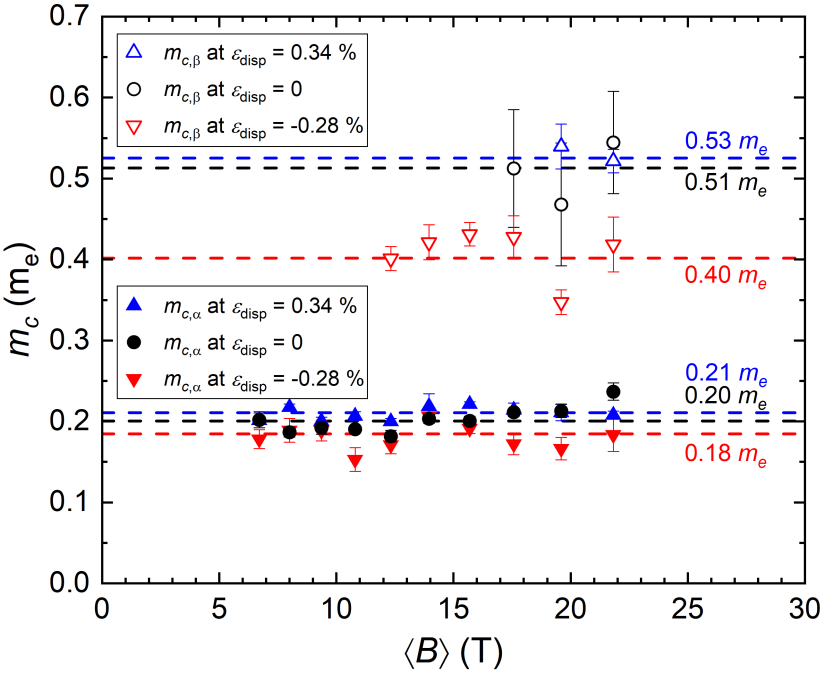


**Figure 3.3.** Quasiparticle cyclotron masses of the $\alpha$ and $\beta$ orbits obtained from the $T$-dependence of the FFT amplitudes with varying average field $\langle B \rangle$. The dashed lines present the average $m_c$ values. The error bars are given by the standard error of the $m_c$ fit parameter.

In order to investigate the field induced mass enhancement along the nodal line reported in Ref.[79], we have calculated FFTs as described above, but at a shifting magnetic field range with a constant width $0.03174\ \mathrm{T}^{-1}$ in $1/B$, see appendix 3.E. The deduced cyclotron mass values for the $\alpha$ and $\beta$ orbits are plotted as a function of $\langle B \rangle$ in Fig. 3.3. The data do not reveal a sizeable field dependence of $m_c$, indicating field induced correlations effects are very weak or absent. The field averaged $m_c$ values at zero, compressive and tensile strain, indicated by the horizontal dashed lines in Fig. 3.3, are listed in Table 3.1 as well. Again the compressive strain mass values appear to be systematically sligthly lower than at zero strain, notably for the $\beta$ orbit, but the error bar is large. We remark that the nodal-line mass enhancement reported in Ref.[79] was obtained for the 600 T orbit, a frequency then attributed to the $\beta$ pocket. However, according to Ref. [53] this frequency has to be attributed

to the magnetic breakdown orbit $2\beta - \alpha$. The $\beta$ orbit has a frequency of 418 T (see Fig. 3.2(d–f)). The FFT amplitudes of the MB orbits obtained in this work are too small to perform a proper field-dependent cyclotron mass analysis.

In order to obtain the Dingle temperature $T_{\mathrm{D}}$ for the $\alpha$ orbit we show in Fig. 3.4 the semilog plot of $\mathrm{D} = \Delta R B \sinh(\xi T/\Delta E_N)$ against $1/B$ at $T = 1.4$ K and different strain values (see Ref. [91]). Here, $\Delta R$ is the SdH oscillation amplitude of the Landau level (LL) at the corresponding $B$-value, calculated from $R_{\mathrm{xx}}$ by subtracting a background determined by a simple second-order polynomial fit. LLs between 4 and 11 T were used, as in this field range the $\alpha$ orbit almost completely dominates the oscillation amplitude. $\Delta E_N(B) = heB/2\pi m_c$ is the energy gap between the $N$th and $(N+1)$th LL, where $m_c$ is the cyclotron mass for the $\alpha$ orbit at a field range of 4 to 11 T (listed in the fifth column of Table 3.1), $e$ is the electron charge and $h$ is the Planck constant. $\xi$ is a constant defined as $\xi = 2\pi^2 k_B$ with $k_B$ being Boltzmann's constant. The $T_{\mathrm{D}}$ for each strain value can be directly calculated from the slope of the corresponding linear fit to the data [50, 91]. The inset of Fig. 3.4 reports the obtained $T_{\mathrm{D}}$ values of 6.2 K under compression, 9.1 K at zero strain and 10.9 K under tension. $T_{\mathrm{D}}$ can be used to acquire a quantitative estimate of the quantum mobility of the $\alpha$ orbit charge carriers, using the relation $\mu_q = (e\hbar/2\pi k_B m_c T_{\mathrm{D}})$ [75]. This gives a $\mu_q$ value of $2.1 \times 10^3$, $1.5 \times 10^3$ and $1.2 \times 10^3$ $\mathrm{cm^2 V^{-1} s^{-1}}$ for compressive, zero and tensile strain, respectively.

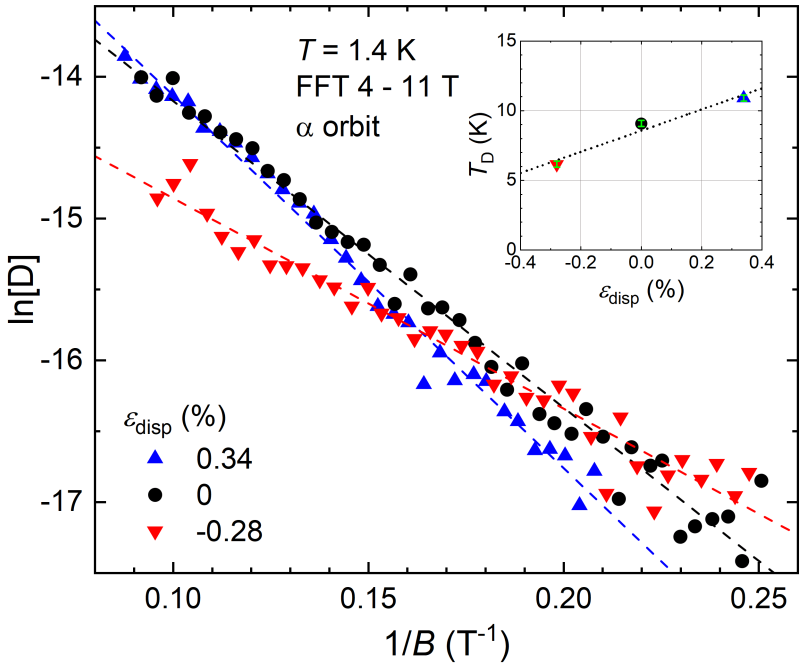


**Figure 3.4.** Dingle plot of the $\alpha$ orbit at three different strain values (evaluated as in Ref. [91]). ln[D] (defined in the text) is plotted as a function of $1/B$. The Dingle temperatures $T_{\mathrm{D}}$ are calculated from the slope of the linear fits (dashed lines). Inset: $T_{\mathrm{D}}$ as a function of $\varepsilon_{disp}$. The error bars are small and shown in green. The dotted line is a linear fit.

## 3.4 Discussion

This work reports the first results of uniaxially strained ZrSiS at fields up to 30 T. The identified frequency peaks in Fig. 3.2(d–f) can be compared to the FFT spectrum in the literature. The observed fundamental frequencies $\alpha$ and $\beta$ ($f = 245$ and 418 T respectively) correspond well to the literature values (see Table 3.2 of appendix 3.F). There is no significant frequency shift as a result of uniaxial strain (see Table 3.1). Using the Onsager relation [50] $F = (\Phi_0/2\pi^2)A_{\mathrm{ext}}$, this implies no significant change in area of any of the measured extremal Fermi surface cross sections. Magnetic breakdown (MB) peaks are situated at similar frequencies as in de Haas-van Alphen (dHvA) oscillation data analyzed in previous work [53].

A remarkable feature of our SdH data is the presence of the $\beta$ peak at 418 T, which was not observed in previous transport studies [53, 79]. It is clearly visible in the zero-strain FFT spectrum, and its amplitude increases under compression. This indicates an increase in the quantum mobility. Note that the $\beta$ orbit has been observed in a dHvA study by measuring torque [53].

MB peaks also are more significant under uniaxial compression: $2\alpha - \beta$ and $3\alpha - \beta$ are not visible in the zero-strain and uniaxially tensioned state. In fact, tensile strain has a completely opposite effect. It suppresses all frequency peaks consisting of orbits that lie on the Dirac nodal line, implying a decrease in quantum mobility for these orbits. This decrease is corroborated by the Dingle temperatures for the $\alpha$ orbit, with $T_{\mathrm{D}}$ increasing with tensile strain and decreasing with compressive strain.

$T_D$ and the quantum mobility are usually determined by the impurity and crystal defect concentration. We do not expect the change of $T_D$ is due to a change in crystal defects, since our measurements are performed in the elastic regime. However, in a layered material under strain or hydrostatic pressure the quantum mobility will depend on the $c/a$ ratio of the crystal lattice. With the distance between the layers decreasing, the inter-layer scattering will increase, which will result in a lower in-plane carrier mobility. For ZrSiS this was recently demonstrated by combined magnetotransport and X-ray diffraction measurements under hydrostatic pressure [81]. In this study, the quantum mobility of the $\alpha$ orbit (designated $\beta$ in [81]) was reported to show an initial decrease at a rate of 30 $\mathrm{cm^2V^{-1}s^{-1}}$/GPa. At the same time the $c/a$ ratio decreases by 0.0005 /GPa. In the case of uniaxial pressure applied along the $a$ axis we may consider $c/\sqrt{ab}$, rather than $c/a$. Using Poisson's ratio to calculate the lattice parameters under strain (see appendix 3.G) we find that $c/\sqrt{ab}$ amounts to 2.277, 2.272 and 2.267 at $-0.28$ % compressive, zero and 0.34 % tensile strain, respectively. The corresponding values of $\mu_q$ are $2.1 \times 10^3$, $1.5 \times 10^3$ and $1.2 \times 10^3$ $\mathrm{cm^2V^{-1}s^{-1}}$, calculated using the Dingle temperature as shown in the last paragraph of the Results section. The overall decrease of $c/\sqrt{ab}$ and $\mu_q$ matches the observed changes in the hydrostatic pressure experiment. Thus we ascertain the increase in quantum mobility can directly be linked to the increase of the $c/a$ ratio.

Another interpretation of the increase in prominence of the MB peaks under uniaxial compression is a decrease in the MB gap size caused by strain. As the MB gap size decreases, an exponentially smaller $B$ is needed in order to cause tunneling events [50]. This will lead to a lower onset magnetic field for the MB orbits and

should, therefore, be visible in the FFT spectra. However, within our experimental resolution we did not detect any differences in the onset field. This is supported by DFT-based band structure calculations that we carried out at zero, compressive and tensile strain applied along the $a$ axis, see appendix 3.H. The main results are presented in Fig. 3.11, where the Fermi surface and the magnetic breakdown gap are presented at different strain values. Notably in Fig. 3.11(b), it is shown that at these low strain levels significant modifications of the Fermi surface and size of the MB gap are absent.

Finally, we remark that quasiparticle orbits that go around the entire nodal loop are not observed. These orbits are referred to as full MB orbits and, in the $Z$-$R$-$A$ plane of ZrSiS, consist of eight tunneling events [79]. Full MB has been clearly observed in previous work [53, 79] and gives rise to high frequency quantum oscillations ($f \sim 8000$ T).

## 3.5 Summary

To summarize, we have presented a comprehensive uniaxial strain study of ZrSiS at low temperatures and at fields up to 30 T. We measured the resistance and analyzed the SdH oscillations to find frequency peaks of extremal Fermi surface cross sections in the FFT spectra that correspond well to literature values [53]. The fundamental $\beta$ peak in our work is more prominent than in previous SdH research [53, 79, 80], and is found to be enhanced relative to the $\alpha$ peak in the uniaxially compressed state. In this state, the MB peaks also are more significant, showing certain linear combinations of quasiparticle orbits not visible in the zero-strain and uniaxially tensioned state. Contrary to compressive strain, tensile strain suppresses all frequency peaks consisting of orbits that lie in the $Z$-$R$-$A$ plane, implying a decrease in quantum mobility for these orbits. This decrease is supported by the calculated Dingle temperatures for the $\alpha$ orbit and attributed to a lowering of the $c/a$ ratio. DFT-based band structure calculations under strain along the $a$ axis substantiate that the FFT frequencies of the $\alpha$, $\beta$ and MB orbits do not change at these low strain values. Therefore, future uniaxial strain research on the Dirac nodal-line semimetal ZrSiS should be directed towards the application of considerable larger strain values: $|\varepsilon_{\text{disp}}| \gg 0.3\,\%$. We note that a related strain study has recently been performed on ZrSiSe (Ref. [9]).

## 3.6 Acknowledgments

We acknowledge the support of the HFML-RU/NWO-I, member of the European Magnetic Field Laboratory (EMFL). This work was supported by the Dutch Research Council (NWO) as part of the TopCore consortium (OCENW.GROOT.2019.048). This work used the Dutch national e-infrastructure with the support of the SURF Cooperative using grants no. EINF-5380 and EINF-7851. L.M.S. was supported by the Princeton Center for Complex Materials, a National Science Foundation (NSF)-MRSEC program (DMR-2011750) and the Gordon and Betty Moore Foundation's EPIQS initiative (grant number GBMF9064). We thank Dr. Yingkai Huang for providing ZrSiS crystals for low magnetic field measurements.

# Appendices

## 3.A Strain cell set-up

Fig. 3.5 shows the completed sample mounting set-up for the ZrSiS sample measured in this work. The strain cell used was the Razorbill CS100. The bar-shaped sample (thickness $\sim$ 120 $\mu$m) is shown to be glued between the titanium sample plates using Araldite glue with a 24 hour curing time. In order to prevent an electrical short, four insulated 70 $\mu$m copper wires were placed between the sample and each sample plate right after the glue was applied. The thinner 25 $\mu$m gold wires were attached to the sample on the titanium-gold sputtered contact pads using DuPont 4929N silver conductive paint. Using the four-point probe method the sample resistance is measured. The wires are attached to the Razorbill WP100 wiring platform on the left, and a piece of double-sided tape on the right.

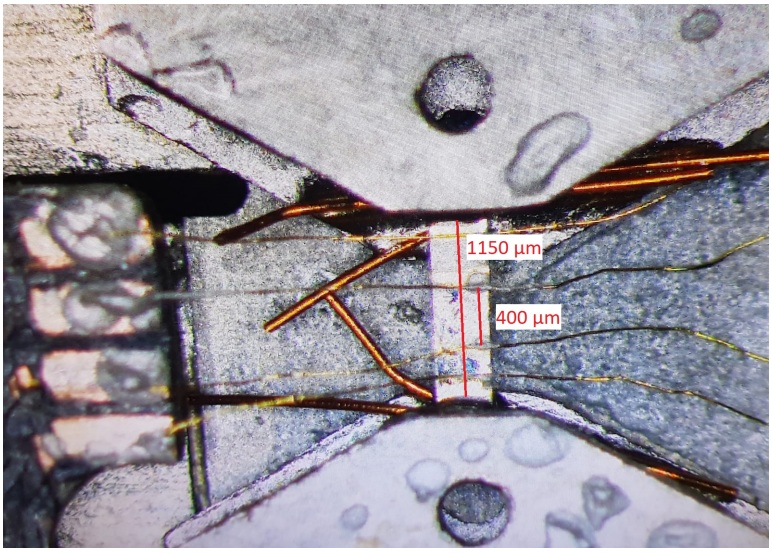


**Figure 3.5.** The ZrSiS single crystal mounted on the Razorbill CS100 strain cell, with electrical wires arranged according to the four-point probe method. The crystal's *ab* plane faces up and the magnetic field is applied along the *c* axis. The longer red bar indicates the shortest distance $L$ between the two glued ends of the sample, while the shorter red bar indicates the distance between the two voltage contacts.

## 3.B Magnetoresistance of strained ZrSiS relative to the zero strain measurement

The difference in longitudinal resistance between the strained curves and the zero strain curve in Fig. 3.1 is defined as $\Delta R_{xx} = R_{xx,\varepsilon} - R_{xx,\varepsilon_0}$. This $\Delta R_{xx}$ is plotted against the magnetic field $B$ in Fig. 3.6, for the four different strain values corresponding to those of Fig. 3.1. The oscillations in the $\Delta R_{xx}$ shown here indicate the tunability of the quantum oscillations through the use of uniaxial strain along the $a$ axis.

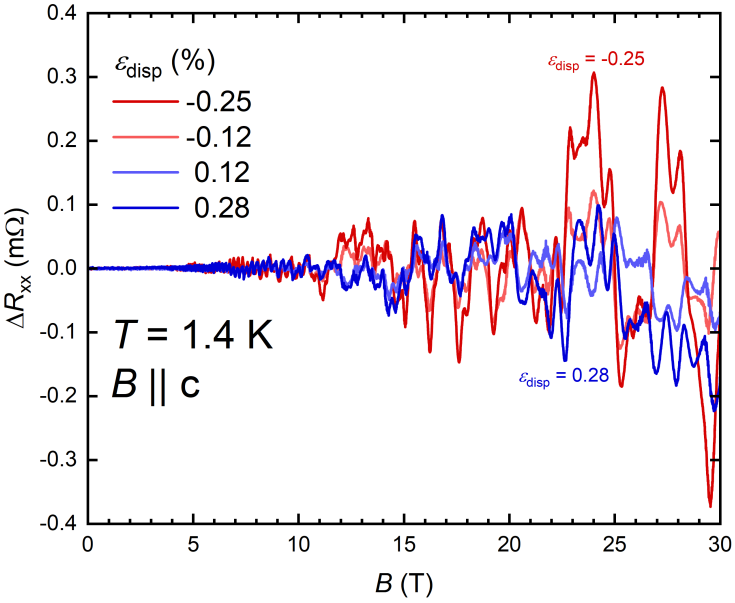


**Figure 3.6.** Difference in longitudinal resistance $\Delta R_{xx}$ in mΩ compared to the zero strain curve shown in Fig. 3.1, against the applied magnetic field $B$ in Tesla for negative and positive strain at 1.4 K.

## 3.C Magnetoresistance curves of temperature-dependent strain measurements

The longitudinal magnetoresistance acquired by sweeping the magnetic field parallel to the *c* axis from 0 to 30 T, at six different temperatures and three different strain values, is displayed in Fig. 3.7. Negative strain means compression, positive strain means tension. The three sets of strain curves have been offset by 1 mΩ for clarity. Curves with higher oscillation amplitudes correspond to lower-temperature data. Note the large increase in background magnetoresistance of the curves taken under tensile strain at 3.2, 4.2 and 6.0 K, possibly as a result of non-elastic deformation. These latter three curves were not used in the analysis of the FFT spectrum of ZrSiS under strain in Fig. 3.2.

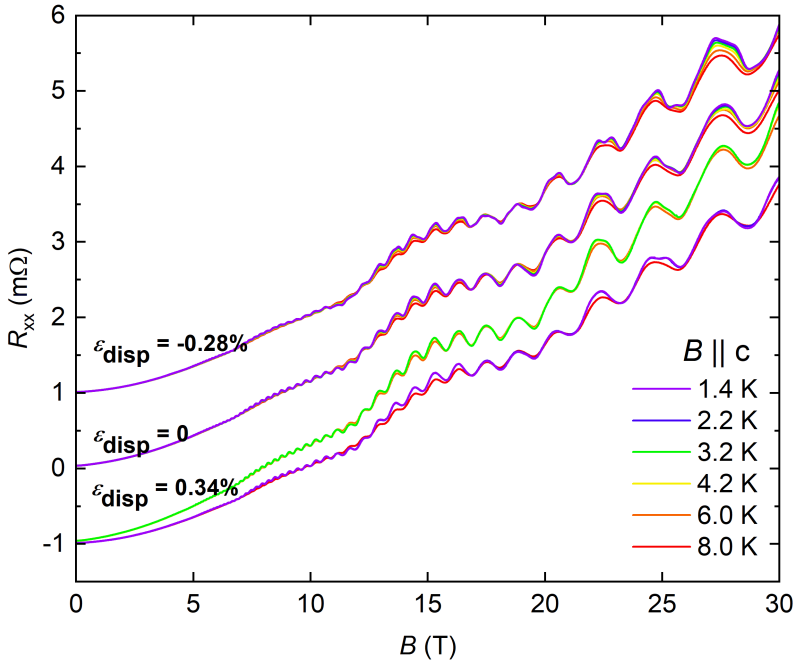


**Figure 3.7.** Magnetoresistance at varying temperature (1.4 to 8.0 K) and different strain values. These curves are used to produce Fig. 3.2 The curves for the different strains have been offset for clarity. Curves with higher oscillation amplitudes correspond to lower-temperature data.

## 3.D FFT plot of the data shown in Fig. 3.1

The FFT plot of Fig. 3.8 shows that, just like for the $T$-dependent run shown in Fig. 3.2, uniaxial strain along the $a$ axis has a systematic effect on the frequency peak structure. Again a weakening of the peak structure is observed upon changing from compressive to tensile strain.

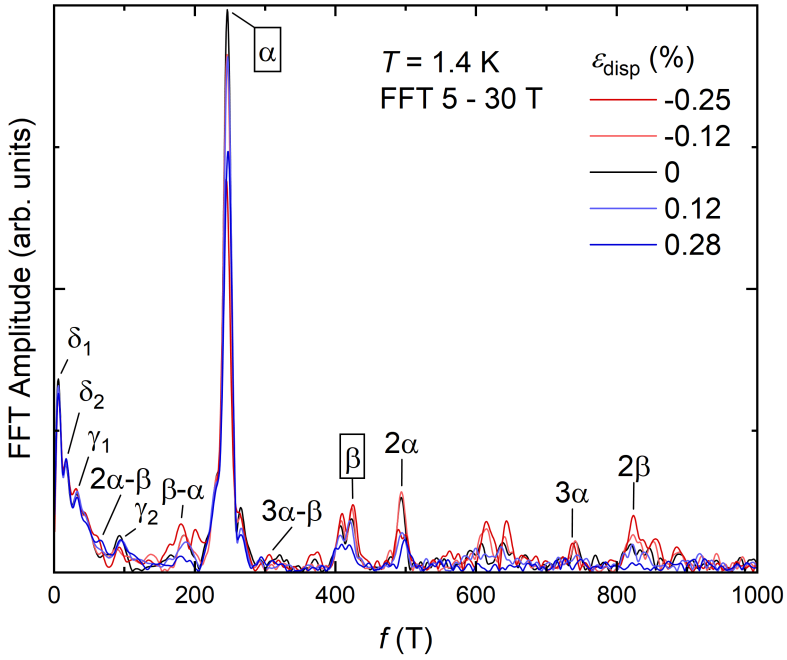


**Figure 3.8.** FFT plot of the data shown in Fig. 3.1. The FFTs were taken in the same way as described for Fig. 3.2, with first derivatives and a magnetic field range of $5 - 30$ T using the Hann window function.

## 3.E Extraction of cyclotron mass using the Lifshitz-Kosevich fit

The cyclotron mass for a quasiparticle orbit frequency is obtained by fitting the temperature evolution of the FFT peak amplitude to the thermal damping factor of the Lifshitz-Kosevich formula $R_T = X/\sinh(X)$, where $X = 14.69 m_c T/\langle B\rangle$. The value for the average field here is defined as $\langle B\rangle = 2/(B_{min}^{-1} + B_{max}^{-1})$. Fig. 3.9 shows the fitting process of the compressed $\alpha$ orbit and zero strain $\beta$ orbit data for different field ranges and therefore different $\langle B\rangle$. Note that for the zero strain $\beta$ orbit data the small FFT amplitudes make taking the proper peak value difficult and lead to the relatively large $m_c$ fitting error shown in Fig. 3.3.

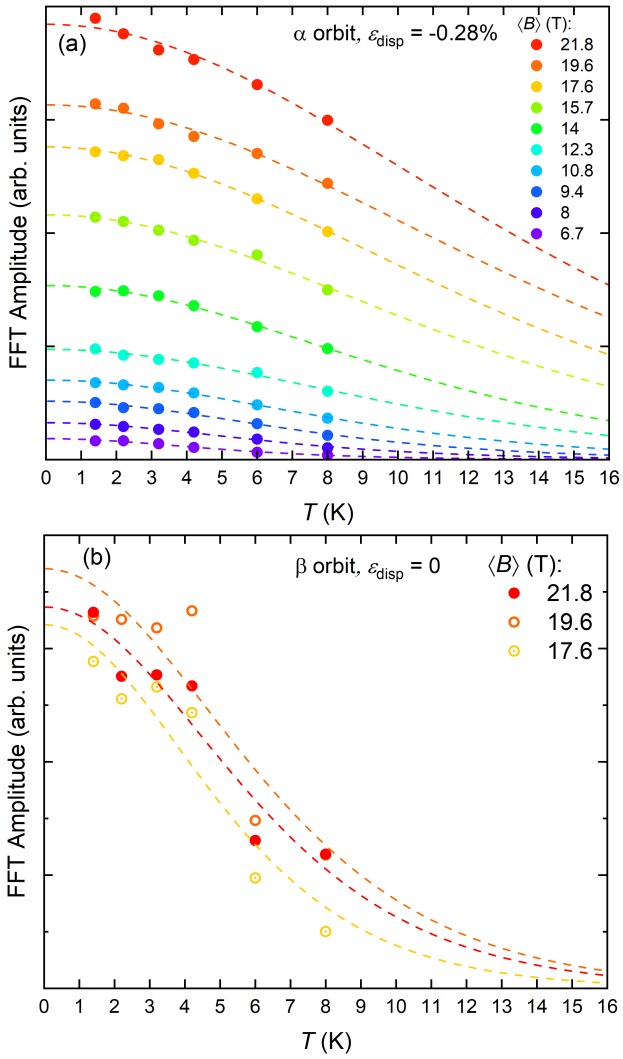


**Figure 3.9.** Temperature dependence of the FFT amplitude of the (a) $\alpha$ pocket at $0.28\,\%$ compression and (b) $\beta$ pocket at zero strain for different field ranges. The different ranges result in different average fields with $\langle B\rangle = 2/(1/B_{max} + 1/B_{min})$ and are indicated by the different colors (in (a), curves from top to bottom correspond to descending $\langle B\rangle$ values). Ranges were taken with equal width in $1/B$. Dashed lines are Lifshitz-Kosevich fits used to extract the cyclotron mass $m_{c,\alpha}$ of the orbit. These fits are used to produce Fig. 3.3 Other cyclotron masses were obtained in the same way.

## 3.F Comparing of observed quasiparticle orbit frequencies to literature

Table 3.2 lists each observed quasiparticle orbit frequency in this work and compares their values with those listed in the work of Müller *et al.* (Ref. [53]) and the frequencies obtained from their density functional theory (DFT) calculations.

**Table 3.2.** The identified orbits and their observed frequencies, compared to the frequencies observed by Müller *et al.* (Ref. [53]) and the frequencies obtained from their DFT calculations. The fundamental frequencies are highlighted in bold. Harmonics such as $2\alpha$ and $2\beta$ have been omitted.

| Orbit | $f$(T) | $f_{\text{Müller}}$(T) | $f_{\text{DFT}}$(T) |
|---|---|---|---|
| $\delta_1$ | **7** | 8 | 7 |
| $\delta_2$ | **16** | 16 | 17 |
| $\gamma_1$ | **31** | 22 | 57 |
| $2\alpha - \beta$ | 72 | 60 | - |
| $\gamma_2$ | **88** | 90 | 156 |
| $\beta - \alpha$ | 173 | 180 | - |
| $\alpha$ | **245** | 240 | 240 |
| $3\alpha - \beta$ | 317 | 300 | - |
| $\beta$ | **418** | 420 | 518 |
| $4\alpha - \beta$ | - | 540 | - |
| $2\beta - \alpha$ | 591 | 600 | - |
| $\alpha + \beta$ | 663 | - | - |

## 3.G Elastic properties of ZrSiS

Poisson's ratios for ZrSiS are determined in the same way as in Schindler *et al.* (Ref. [88]) using Voigt notation. The values for the stiffness tensor $C$ of ZrSiS calculated by de Jong *et al.* (Ref. [92]) are $C_{11} = 255$, $C_{12} = 69$, $C_{13} = 77$, $C_{33} = 187$, $C_{44} = 84$ and $C_{66} = 122$ GPa, at zero pressure and zero temperature. Tension along the $a$ axis results in compression along the $b$ axis, with Poisson's ratio

$$\nu_{21} = \frac{C_{12}C_{33} - C_{13}^2}{C_{11}C_{33} - C_{13}^2} \tag{3.1}$$

and also results in compression along the $c$ axis, with Poisson's ratio

$$\nu_{31} = \frac{(C_{11} - C_{12})C_{13}}{C_{11}C_{33} - C_{13}^2}. \tag{3.2}$$

This results in $\nu_{21} = 0.17$ and $\nu_{31} = 0.34$.
In its unstrained tetragonal state, the lattice parameters of ZrSiS are $a = b = 3.556$ Å and $c = 8.180$ Å. $a = b = 3.542$ Å and $c = 8.049$ Å. These are the values obtained by Müller *et al.* (Ref. [53]) by using X-ray diffraction on samples grown with the same method, by the same group (Schoop lab at Princeton University). In this study, the sample is strained up to $\varepsilon_{\text{disp}} = -0.28\,\%$ compression and $\varepsilon_{\text{disp}} = 0.34\,\%$ tension along the $a$ axis. See Table 3.3 below for changes in lattice parameters and volume with strain. The percentual changes in $c/\sqrt{ab}$ and their corresponding $\mu_q$ values with tensile strain show a trend that closely matches that of $c/a$ and $\mu_q$ with hydrostatic pressure in Gu *et al.* (Ref. [81]). We use $c/\sqrt{ab}$ instead of $c/a$ to account for the fact that $a \neq b$ under uniaxial strain.

**Table 3.3.** The effect of uniaxial strain along the $a$ axis on the lattice parameters and unit cell volume of ZrSiS. The negative compressive and positive tensile strain values from Fig. 3.2 been used, together with the calculated Poisson's ratios.

| $\varepsilon_{\text{disp}}$(%) along $a$ | $a$(Å) | $b$(Å) | $c$(Å) | V(Å$^3$) | ΔV(%) | $c/\sqrt{ab}$ | $\Delta(c/\sqrt{ab})(\%)$ |
|---|---|---|---|---|---|---|---|
| 0 | 3.542 | 3.542 | 8.049 | 100.981 | 0 | 2.272 | 0 |
| -0.28 | 3.532 | 3.544 | 8.057 | 100.853 | -0.13 | 2.277 | 0.21 |
| 0.34 | 3.554 | 3.540 | 8.040 | 101.153 | 0.17 | 2.267 | -0.25 |

## 3.H Band structure calculations of ZrSiS under strain

The Fermi surfaces of four structures with different sets of lattice parameters were obtained with density functional theory (DFT). The results are based on the all-electron full-potential augmented plane-wave (FLAPW) formalism, as implemented in the SPEX code (Friedrich *et al.*, Ref. [93]). We used the generalized-gradient approximation (GGA) in the PBE parametrization (Perdew *et al.*, Ref. [94]). Spin-orbit coupling was included in the calculations in a second-variation scheme. The bases for the calculations were constructed by setting the maximal angular momentum $l_{max}$ as 11, 8, and 8 for the muffin-tin parts of Zr, Si, and S, respectively, and $k_{max} = 3.99\,\text{bohr}^{-1}$ for the interstitial part. The Brillouin zone integration was performed on a $14 \times 14 \times 14$ Monkhorst-Pack **k**-point mesh. The data for the Fermi surface plots were generated by the Wannier90 code [95]. We used Wannier90 to interpolate the bands around the Fermi level at a plane with $k_z = 0.5$ rlu, and $k_{\{x,y\}} \in [-0.5, 0.5]$ rlu, with $101 \times 101$ **k**-point mesh, where "rlu" refers to "relative (reciprocal) lattice unit". The Wannier90 interpolated bands were subsequently interpolated by cubic interpolation 4 times and 10 times (thus $4 \times (101 \times 101)$ or $10 \times (101 \times 101)$ **k**-point mesh after cubic interpolation) for both panels of Figure S7.

The lattice parameters of the four structures are shown in Table 3.4. The internal positions were kept fixed for the four structures as: $Z_{Zr} = 0.7308$ and $Z_S = 0.6225$.

**Table 3.4.** The four structures with different sets of lattice parameters used to obtain the different Fermi surfaces of ZrSiS. Structure 1 uses values obtained from the Materials Project (Ref. [96]) and structure 2 uses values obtained by Müller *et al.* (Ref. [53]). Structures 3 and 4 are the values from Müller under compression and tension, respectively, detailed in subsection G.

| | Mat. Proj. (structure 1) | Müller (structure 2) | Compressed (structure 3) | Tensioned (structure 4) |
|---|---|---|---|---|
| $a$ (Å) | 3.554 | 3.542 | 3.532 | 3.554 |
| $b$ (Å) | 3.554 | 3.542 | 3.544 | 3.540 |
| $c$ (Å) | 8.118 | 8.049 | 8.057 | 8.040 |

Fig. 3.10 shows the calculated DFT-based band structures of ZrSiS for the four structures mentioned in Table 3.4. Fig. 3.11(a) shows the corresponding 2D Fermi surfaces in the Z-R-A plane in reciprocal lattice units (rlu). Fig. 3.11(b) shows the MB gap for each structure more closely. Note that there is no significant change in MB gap size: the Fermi surfaces slightly shift relative to each other, but the gap size stays the same. The zero-strain results of the calculations are also in excellent agreement with those performed by Müller *et al*. and Pezzini *et al*. (Ref. [53] and Ref. [79])

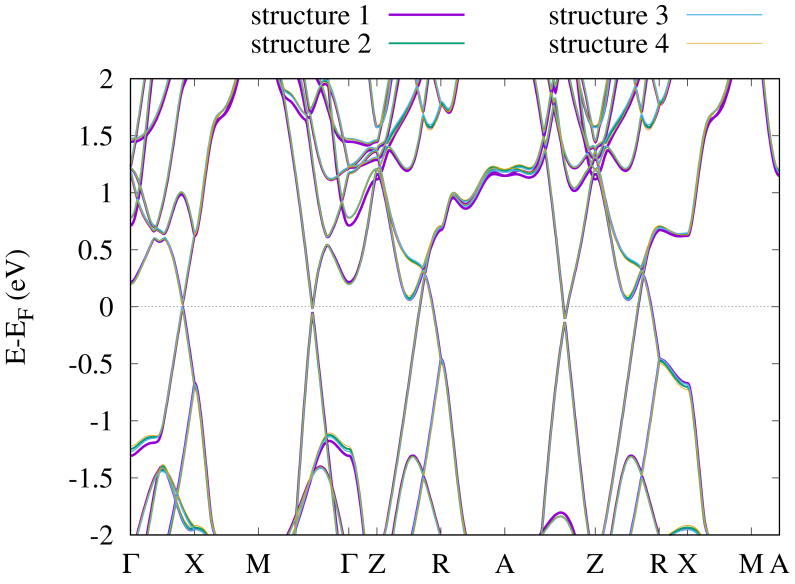


**Figure 3.10.** Calculated DFT-based band structures of ZrSiS for the four structures mentioned in Table S3.

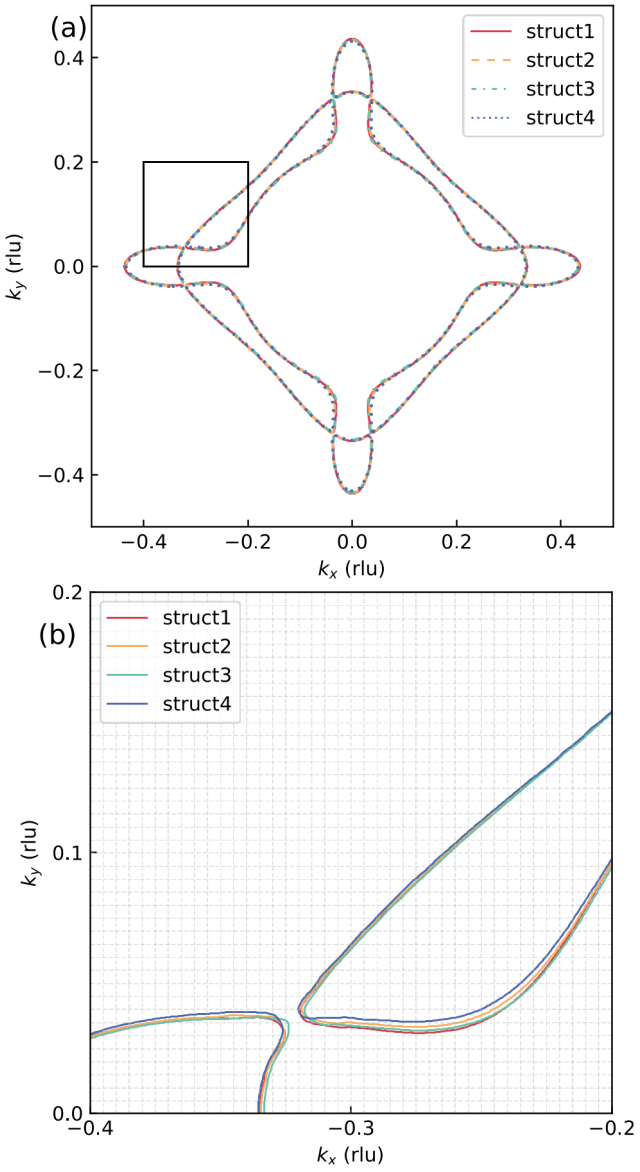


**Figure 3.11.** The 2D Fermi surfaces in the Z-R-A plane corresponding to the band structures of Fig. 3.10 are shown in (a). The area enclosed by the black square is displayed larger in (b).

# 4 Characterizing the upper critical field of the layered superconductor $LaO_{0.8}F_{0.2}BiS_{2-x}Se_x$ ($x = 0.5$ and $x = 1.0$)

## 4.1 Introduction

A new family of layered superconductors was discovered in 2012 by Mizuguchi *et al.*, composed of alternately stacked blocking layers and $BiCh_2$ (Ch = S, Se) conducting bilayers, see Fig. 4.1 [97]. The discovery opened up a new dimension to the field of low-dimensional superconductivity, adding to the cuprates and Fe-based superconductors. Typically, $BiCh_2$-based superconductors are of the $REOBiCh_2$ type (RE = Rare Earth), which is a band insulator. Sufficiently substituting O sites with F makes the system semimetallic and leads to superconductivity at low temperatures ($T_c = 2$–$10$ K) through electron-carrier doping [98–103]. In this chapter, we report investigations of the compound $LaO_{0.8}F_{0.2}BiS_{2-x}Se_x$ with $x = 0.5$ and $x = 1.0$. With this amount of F-doping no superconductivity emerges for $x = 0$, even at low temperatures. However, as shown in Fig. 4.2, substituting S with Se provides a chemical pressure that causes there to be less in-plane disorder, leading to a bulk superconducting state [98, 99, 103]. With access to the bulk superconducting state in these two materials that were made available to us by guest researcher Kazuhisa Hoshi from the group of Yoshikazu Mizuguchi in Tokyo Metropolitan University, and with previous characterization measurements performed on them at lower magnetic field strengths, we decided to pick these materials to further elucidate. More specifically, the goal of this work was to measure the resistance of $LaO_{0.8}F_{0.2}BiS_{2-x}Se_x$ ($x = 0.5$ and $1.0$) single crystals in magnetic fields up to 30 T and at temperatures down to $0.35$ K to then analyze their upper critical field $B_{c2}$. The superconducting properties of this material family have already been intensively investigated, yet the exact mechanism that is responsible for their extremely high $B_{c2}$ is still not fully understood.

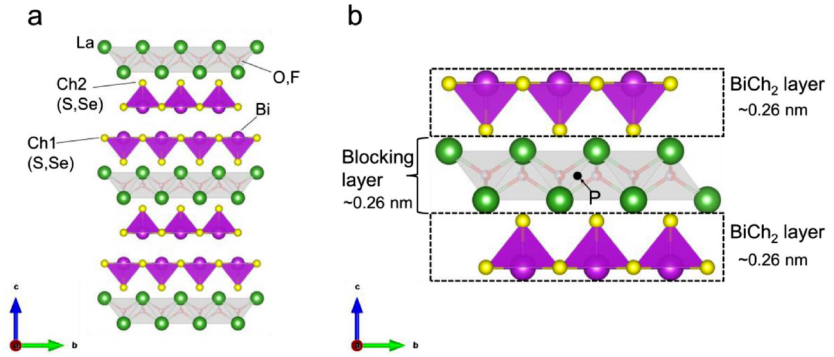


**Figure 4.1.** (a) Schematic crystal structure of $LaO_{0.8}F_{0.2}BiS_{2-x}Se_x$, with tetragonal space group $P4/nmm$. (b) shows two $BiCh_2$ layers and a LaO blocking layer. The symbol P in the LaO blocking layer points at the global inversion centre for the $LaO_{0.8}F_{0.2}BiS_{2-x}Se_x$ system, while the inversion symmetry is locally broken in each $BiCh_2$ layer. Figure adapted from Ref. [104].

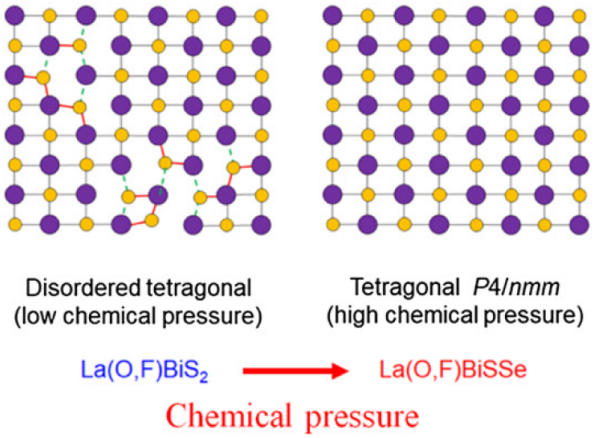


**Figure 4.2.** Chemical pressure effect of Se doping, changing the material from a disordered to an ordered tetragonal phase. Figure adapted from Ref. [105].

In type-II superconductors, $B_{c2}$ is mainly determined by the paramagnetic pair-breaking effect and the orbital pair-breaking effect. The paramagnetic

pair-breaking effect is a result of spin polarization attributed to the Zeeman effect. At sufficiently high magnetic fields, enough magnetic energy (the Zeeman energy) is available to flip an electron spin between the up and down states, exceeding the binding energy of the Cooper pairs, destroying superconductivity. The orbital pair-breaking effect is due to vortex formation. In the presence of a magnetic field, Abrikosov vortices are formed. These vortices consist of a normal-state core with a surrounding supercurrent which carries a certain amount of kinetic energy. An increasing magnetic field will introduce more vortices. If the total kinetic energy of all the vortices exceeds the binding energy of a Cooper pair, the paired electrons are decoupled and the material enters the normal state.

The lower one of the two limits generally decides the value of the observed $B_{c2}$. For spin-singlet superconductors, the paramagnetic limit (Pauli limit) is given by the relation $B_{\mathrm{P_{wc}}} = 1.86\ T_c$ when assuming the weak-coupling limit [106]. Magnetic penetration depth measurements on $Bi_4O_4S_3$ [107] and $NdO_{1-x}F_xBiS_2$ ($x = 0.3$ and $0.5$) [108], together with specific heat measurements on $LaO_{0.5}F_{0.5}BiSSe$ [109, 110], suggest that these materials are fully gapped s-wave superconductors with a strong-coupling nature – the force holding together the superconducting electron pairs is unusually large. Using the SC-gap ratio $2\Delta(0)/k_BT_c = 5$ found in Ref. [110], a strong-coupling limit would result in a paramagnetic limit for $B_{c2}$ given by the relation $B_{\mathrm{P_{sc}}} = 2.5k_BT_c/\sqrt{2}\mu_B \sim 2.63\ T_c$ [106]. As for the orbital limit, $B_{c2}$ at $T = 0$ is often based on the initial slope of $B_{c2}$ at $T_c$ and the relation $B_{\mathrm{WHH}} = 0.69T_c(-dB_{c2}/dT)_{T_c}$ in the dirty limit taken from Werthamer-Helfand-Hohenberg (WHH) theory [111]. The dirty limit, in which the coherence length $\xi$ is comparable to or larger than the mean free path $l$, is assumed due to the undeniable existence of atomic defects in our crystals [105].

$LaO_{0.8}F_{0.2}BiS_{2-x}Se_x$ has a centrosymmetric, tetragonal crystal structure with locally broken inversion symmetry in the $BiCh_2$ layer, see Fig. 4.1. This local inversion asymmetry induces Rashba-type spin-orbit coupling, which is expected to lock the spin direction onto the $ab$ plane, thereby suppressing the paramagnetic pair-breaking effect and enhancing $B_{c2}$ [112]. The spin polarisation that is attributed to this local Rashba spin-orbit coupling was directly observed by spin and angle resolved photoemission spectroscopy (spin ARPES) for $LaO_{0.55}F_{0.45}BiS_2$ [113]. Another property of $LaO_{0.8}F_{0.2}BiS_{2-x}Se_x$ that is expected to enhance the orbital limit is its layered structure, as 2D systems and layered superconductors tend to

have an out-of-plane coherence length $\xi_\perp(T)$ at $T = 0$ that is smaller than the layer thickness [104].

The in-plane spin-locking effect of Rashba spin-orbit coupling tends to weaken interlayer (Josephson) coupling and enhance the 2D nature of superconductivity. With $B \parallel ab$, Ref. [104] proposed a situation similar to that of Ref. [114] with $MoS_2$, in which a reduction in Josephson coupling between superconducting $BiCh_2$ layers causes Josephson vortices to penetrate the LaO blocking layer and induce the orbital pair-breaking effect. The mechanism by which this happens is thought to be analogous to that of the conventional BCS state: the depairing of the electrons happens when the kinetic energy associated with the supercurrents of the Josephson vortices exceeds their condensation energy. Demonstrating whether or not this Josephson vortex state (also known as the complex-stripe phase) is established in $LaO_{0.8}F_{0.2}BiS_{2-x}Se_x$ can be done experimentally in three ways. Firstly, when the $B_{c2}(T)$ curve shows an upturn as it approaches low $T$, it can be interpreted as a crossover from the conventional BCS (or Abrikosov) phase to the Josephson vortex state, see Fig. 4.3 [114, 115]. A transition to the so-called helical phase is then expected to follow up at a higher magnetic field region of the phase diagram [115], manifesting as a downturn in the dependence of $B_{c2}$ on $T$. This helical phase is a consequence of the Josephson vortices penetrating between the blocking layers, effectively weakening the Josephson coupling and introducing independent superconducting states in the $BiCh_2$ layers [115].

Secondly, the out-of-plane coherence length $\xi_\perp(0)$ can be evaluated and compared to the thickness of the blocking layer. In the case of the Josephson vortex state, $\xi_\perp(0)$ is to be smaller than the blocking layer thickness, but greater than half of it. Lastly, Josephson vortices can be confirmed by measuring a change from 3D to 2D behavior. This can be done through the fitting of the angle dependence of $B_{c2}$ with the anisotropic 3D Ginzburg-Landau (GL) model and the 2D Tinkham (TH) formula [10]. The best fit of the two would imply the dimensionality of the material.

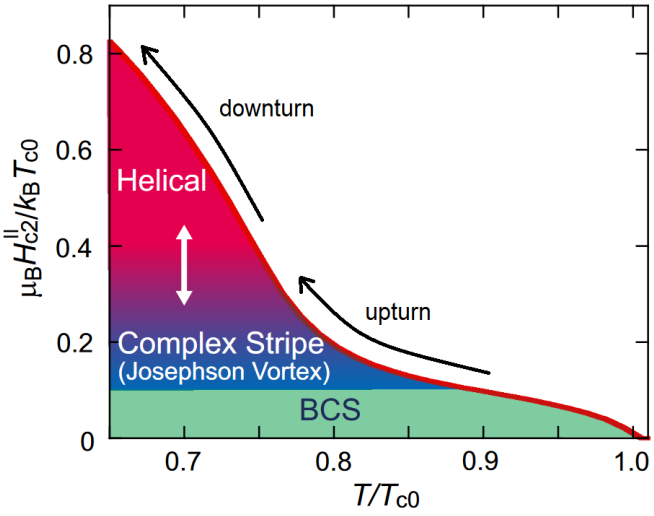


**Figure 4.3.** Normalized phase diagram displaying the dependence of the in-plane upper critical field on the temperature. As the temperature is lowered, an upturn in the behavior of the in-plane upper critical field is linked to the entering of the complex-stripe phase. Further lowering of the temperature is then met by a downturn, linked to the entering of the helical phase. Figure adapted and edited from Ref. [115].

Hoshi *et al.* performed static and pulsed field measurements on $LaO_{0.5}F_{0.5}BiS_{2-x}Se_x$ ($x = 0.22$ and $0.69$) and observed the described upturn behavior of $B_{c2}(T)$, but no clear transition to the helical phase [104]. A $\xi_{\perp}(0.47)$ of 0.22 ($x = 0.22$) and 0.23 nm ($x = 0.69$) was found, smaller than the blocking layer thickness of 0.26 nm. At $T = 2.5$ and $T = 3.5$ K for the respective doping amounts, both $B_{c2}(\theta)$ data were fit best with the anisotropic 3D GL model, implying 3D dimensionality.

With the experimental groundwork laid out and a potential explanation for the behavior of the $B_{c2}$ of $REOBiCh_2$ materials postulated, we aimed to further elucidate the relevant mechanisms and characterize the $B_{c2}$ of $LaO_{0.8}F_{0.2}BiS_{2-x}Se_x$ ($x = 0.5$ and $1.0$). The resistance of the materials was measured at temperatures down to $T = 0.35$ K and static magnetic fields up to $B = 30$ T to construct a more complete picture of the $B_{c2}(T)$ phase diagram and perform an out-of-plane coherence length analysis. The angle dependence of $B_{c2}$ was fitted with the anisotropic 3D GL model and the 2D TH formula, providing a dimensional anal-

ysis of the two materials at $T = 0.35$ K. The behavior of our samples proves to be in line with previous, higher temperature measurements on other samples of the same batch. Those measurements were performed by Kazuhisa Hoshi (obtained through private communication) and Marc Salis, a PhD student in the group of Anne de Visser [116]. The low-$T$ data follows the upturned trend of high-$T$ data. With the $B_{c2}$ of both doping levels greatly exceeding the Pauli and WHH orbital limit, it can be assumed that both the paramagnetic and orbital pair-breaking effect are strongly suppressed. At $T = 0.35$ K, a significant downturn in the dependence of $B_{c2}$ on $T$ is still not observed. The out-of-plane coherence lengths were calculated from our obtained experimental parameters, giving $\xi_\perp(0) = 0.54$ nm for $x = 0.5$ and $\xi_\perp(0) = 0.46$ nm for $x = 1.0$. The dimensionality analysis provided no clear answer, as the angle-dependent data of both doping levels were not matched better by one fit or the other. These results strongly suggest that the Josephson vortex state is not realized in $LaO_{0.8}F_{0.2}BiS_{2-x}Se_x$. However, further research could perhaps provide a more decisive dimensionality analysis. Our results add to the existing wealth of knowledge on high $B_{c2}$ superconductors and the relationship between superconductivity and local inversion symmetry breaking.

## 4.2 Sample acquisition and characterization

The single crystals used in this study were provided by Kazuhisa Hoshi. They belong to a batch synthesized using a high-temperature flux method in a quartz tube in vacuum [117], as described in Ref. [104]. An energy-dispersive X-ray (EDX) analysis was performed to estimate the stoichiometric composition of the samples and showed their values to be consistent with the nominal composition. Typical sample dimensions were around $1 \times 1 \times 0.1$ mm$^3$ ($a \times b \times c$).

All resistance measurements were performed using the four-point probe method with the current flowing along the $ab$-plane. Characterization of the samples used in this study was first done in the PPMS using the rotator probe down to a temperature of 2 K. The observed superconducting transitions had a $T_c$ that corresponded well to the literature [103]: 2.88 K for $x = 0.5$ and 2.76 K for $x = 1.0$. The samples were rotated to identify the position in which the $ab$-plane of the samples was parallel to the magnetic field direction. Magnetic fields up to 9 T were then applied at 2 K to measure the $B_{c2}$ of the samples parallel to the $ab$-plane. This gave $B_{c2} = 5.6$ T for $x = 0.5$ and 3.4 T for $x = 1.0$, generally in line with previous measurements performed by Kazuhisa Hoshi and Marc Salis on other samples of

the same batch [116]. The values for $B_{c2}$ were acquired by taking the onset value of the superconducting-to-normal transition.

The remainder of the measurements in this work were performed in Nijmegen at the High Field Magnet Laboratory (HFML) in a $^4$He bath cryostat with a $^3$He base temperature of 0.35 K. The magnetic field sweeps were carried out using a resistive Bitter magnet. Fig. 4.4 shows the cool down measurement of the resistance of two samples measured in Nijmegen using the four-point probe method with 30 $\mu$m diameter gold wires. These were mounted on a rotator cryostat-insert together with a Hall probe that functioned as a field angle calibrator, see Fig. 4.5. The two samples shown in Fig. 4.4 provided the most clear data out of the sample set. Their analysis and data are therefore shown throughout the rest of this chapter. The $T_c$ values of the $x = 0.5$ and 1.0 samples are found to be 2.65 and 2.81 K, respectively. The superconducting transition of the $x = 0.5$ sample in Fig. 4.4 shows a jump near the bottom end of the transition. The measurements in Nijmegen were performed using a Stanford Research Systems SR865A Lock-In amplifier for an enhanced signal-to-noise ratio (SNR), as the measured sample resistance was small relative to the large contact resistance ($\sim$ 300 $\Omega$). This phase-sensitive detection method is an AC transport technique that can introduce odd lineshapes near superconducting transitions that are not observed with DC techniques [118]. In order to reduce the effect of the superconducting phase on the lineshape of our data, the data shown in Fig. 4.4 takes into account the in-phase ($X$) and quadrature ($Y$) components with $R = \sqrt{X^2 + Y^2}$, through which the phase dependency is removed. However, an odd-looking lineshape persists, possibly due to differences in $T_c$ between regions of the sample, inductive coupling caused by phase shifting near $T_c$, and/or signal-processing effects [118]. Although the lineshape is not ideal for further data analysis, we chose to try and take into account every possible interpretation of the data. If a line is drawn through the main drop of the transition, this intersects the $R = 0$ axis at a $T_c$ of 2.91 K, corresponding much better to the previous data from Salis and Hoshi. In the rest of this chapter, we keep acquiring $B_{c2}$ by taking onset values and all data shown has been analyzed with a great emphasis on consistency.

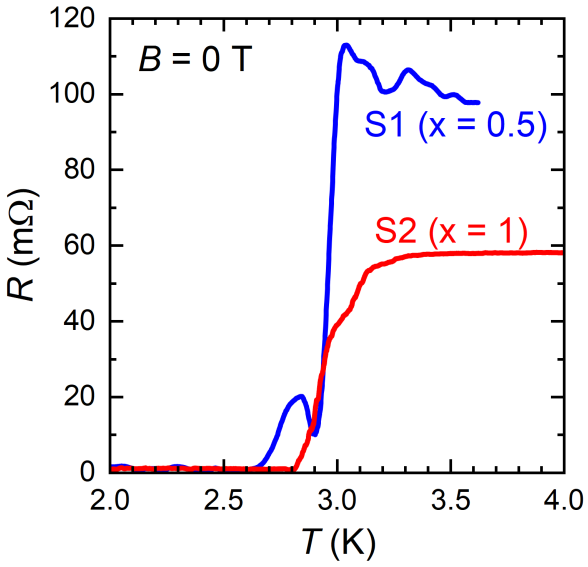


**Figure 4.4.** Cool down measurements of the resistance of $LaO_{0.8}F_{0.2}BiS_{2-x}Se_x$ (S1 $x = 0.5$ and S2 $x = 1.0$), performed in Nijmegen at zero external field.

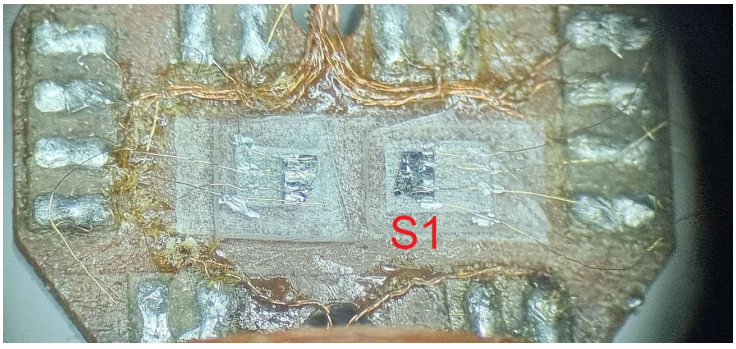


**Figure 4.5.** Sample 1 and a second sample mounted on the rotator insert and connected with gold wires. The Hall probe is positioned on the back side of the rotating sample platform.

## 4.3 Results and discussion

Fig. 4.6(a,b) shows a series of magnetic field sweeps of the resistance of both sample 1 (S1, $x = 0.5$) and sample 2 (S2, $x = 1.0$) at varying magnetic field angles and at a temperature of $0.35$ K. At a field angle of $0°$ the field is parallel to the out-of-plane $c$ axis, while at a field angle of $90°$ the field is parallel to the $ab$ plane. S1 and S2 both show a small angle mismatch of $1.5°$ with $88.5°$ being the angle at which the samples show the highest $B_{c2}$. Although the apparent resistance of S1 isn't 0 m$\Omega$ before starting the superconducting-to-normal transition, we still assume the sample to be in the superconducting state at $B = 0$ and $R \sim 20$ m$\Omega$. The same sample has shown an appropriate zero-resistance in its superconducting state during the characterization measurements in the PPMS. Non-zero resistance offsets below $T_c$ tend to be common in samples measured with AC transport techniques, so we believe this offset can be explained by signal-processing effects [118].

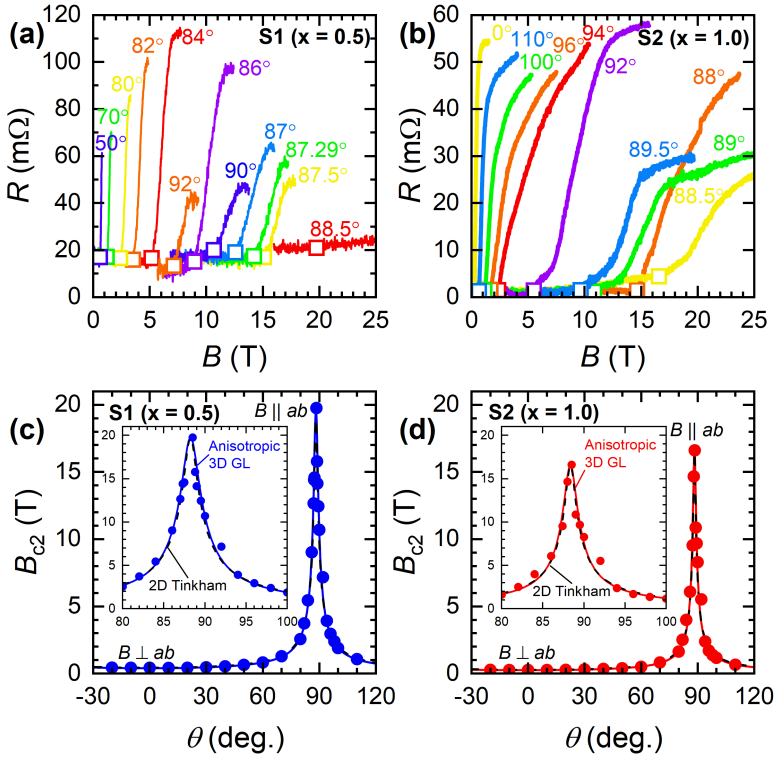


**Figure 4.6.** Dimensionality analysis of $LaO_{0.8}F_{0.2}BiS_{2-x}Se_x$ ($x = 0.5$ and 1.0). (a) and (b) show a series of magnetic field sweeps of the resistance of S1 ($x = 0.5$) and S2 ($x = 1.0$), respectively. The squares mark the onset of the superconducting-to-normal transition. The measurements were performed at $T = 0.35$ K. At a field angle of 0° the field is nominally parallel to the out-of-plane $c$ axis, while at a field angle of 90° the field is nominally parallel to the $ab$ plane. (c) and (d) show the dependence of $B_{c2}$ on the field angle by respectively plotting the onset values taken from (a) and (b). The insets of (c) and (d) show a smaller angle range of the same data and point out the fits to the anisotropic 3D Ginzburg-Landau (GL) model and the 2D Tinkham (TH) formula.

Fig. 4.6(c,d) shows the dependence of $B_{c2}$ on the field angle by respectively plotting the onset values taken from Fig. 4.6(a,b). To avoid cluttering, not all curves corresponding to the points shown in Fig. 4.6(c,d) are plotted in Fig. 4.6(a,b). The

data of both samples are fitted to the anisotropic 3D GL model and the 2D TH formula [10], given by:

$$\text{3D GL:} \quad \left(\frac{B_{c2}(\theta)\cos(\theta)}{B_{c2}^{\perp}}\right)^2 + \left(\frac{B_{c2}(\theta)\sin(\theta)}{B_{c2}^{\parallel}}\right)^2 = 1 \tag{4.1}$$

$$\text{2D TH:} \quad \left|\frac{B_{c2}(\theta)\cos(\theta)}{B_{c2}^{\perp}}\right| + \left(\frac{B_{c2}(\theta)\sin(\theta)}{B_{c2}^{\parallel}}\right)^2 = 1. \tag{4.2}$$

To take into account the angle mismatch, $\theta$ was replaced by $\theta + m$, with $m$ being the angle mismatch in degrees. With few datapoints around the maximum of the $B_{c2}$, it proved difficult to get a nice fit for both models. Therefore, a minimum for the peak value of the fits was set as a hard boundary, using the $B_{c2}$ value of the datapoint with the highest $B_{c2}$ (88.5°) as the minimum value. Both fits follow the data quite well, however, their difference is too small to be able to draw any conclusions regarding the dimensionality of the samples. Dimensionality analysis was performed on $LaO_{0.5}F_{0.5}BiS_{2-x}Se_x$ by Hoshi *et al.* [104] and shows the GL 3D and 2D TH fits to be more distinguishable. This is due to the value of the $B_{c2}^{\parallel}$ being much smaller than is the case in our data (3 T versus 20 T), making their $B_{c2}$ peak much less sharp. The rounded peak of the GL 3D fit and the cusp-like peak of the 2D TH fit are therefore hard to differentiate here. The low quality field angle data close to $B \parallel ab$ that has been omitted due to significant signal processing effects reduces the amount of available datapoints in Fig. 4.6(c,d), adding to the difficulty of assessing the match of the data to the fits.

Fig. 4.7(a,b) shows a series of magnetic field sweeps of the resistance of S1 and S2 at varying temperatures and a fixed field angle of $B \parallel ab$. In order to more clearly display the data in Fig. 4.7(a), the $R$ axis was normalized with respect to the normal-phase resistance of the $T = 1.32$ K curve and $R_0$ was offset so that the superconducting state consistently shows $R = 0$ mΩ. Again, we believe the non-zero resistance below $T_c$ can be explained by signal-processing effects [118].

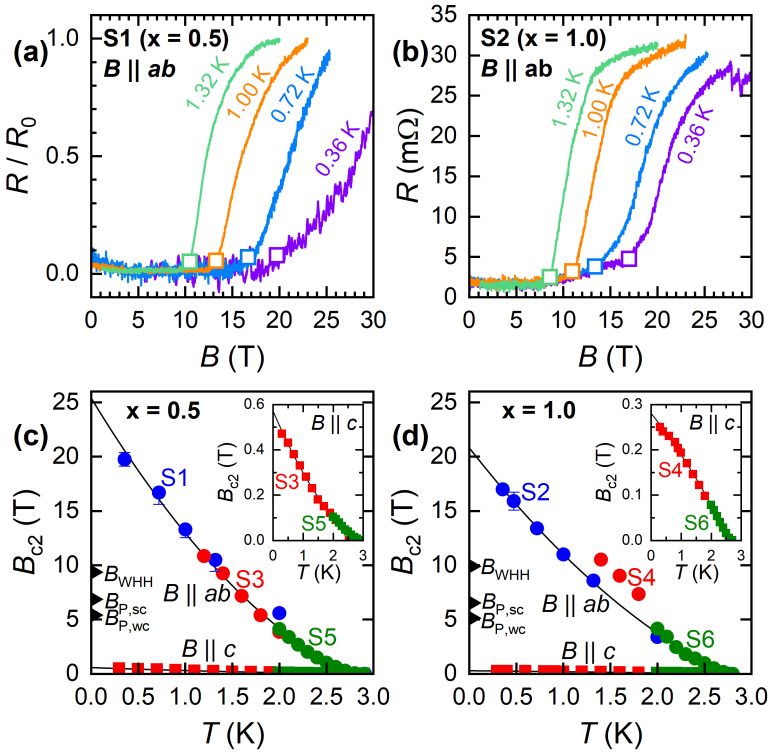


**Figure 4.7.** (a,b): Magnetic field sweeps of the resistance of S1 ($x = 0.5$) and S2 ($x = 1.0$), respectively. Now, a fixed field angle of $B \parallel ab$ is used, while the temperature is varied. Squares mark the onset of the superconducting-to-normal transition. Curves in (a) are normalized and offset. (c) and (d) show the $B_{c2}(T)$ phase diagram using data obtained in this work (blue), and data from Marc Salis (red, Ref. [116]) and Kazuhisa Hoshi (green, private communication). The solid black lines are second-order polynomial fits that function as a guide to the eye. The conventional limits are pointed out by black triangles on the left of each graph. These include the weak-coupling and strong-coupling Pauli limits ($B_{\mathrm{P_{wc}}}$ and $B_{\mathrm{P_{sc}}}$) and the orbital limit ($B_{\mathrm{WHH}}$). The insets use a smaller scale of the same data in order to display the trend of the $B \parallel c$ datapoints more clearly.

Fig. 4.7(c,d) shows the $B_{c2}(T)$ phase diagram for both doping levels for $B \parallel c$ and $B \parallel ab$. The datapoints are a compilation of the samples measured in this work (S1, S2), by Marc Salis in the Heliox 3-He refrigerator (S3, S4) [116], and by Kazuhisa Hoshi in the PPMS (S5, S6) (private communication). The

weak-coupling and strong-coupling Pauli limits ($B_{\mathrm{P_{wc}}}$ and $B_{\mathrm{P_{sc}}}$) and the orbital limit ($B_{\mathrm{WHH}}$) are calculated and included for both samples. It is immediately evident that all of these limits are easily broken, implying that the corresponding pair-breaking effects are greatly suppressed. In both samples at $B \parallel ab$ the second order polynomial trend appears to continue down to base temperature, showing no significant sign of a downturn.

In order to calculate the out-of-plane coherence lengths of the two samples at $T = 0$, the following expressions are used [104]:

$$\xi_{\parallel}(0) = \sqrt{\frac{\Phi_0}{2\pi B_{c2}^{\perp}(0)}} \tag{4.3}$$

$$\xi_{\perp}(0) = \frac{\Phi_0}{2\pi \xi_{\parallel}(0) B_{c2}^{\parallel}(0)} \tag{4.4}$$

where $\Phi_0$ is the flux quantum. $B_{c2}^{\perp}(0)$ and $B_{c2}^{\parallel}(0)$ are estimated from Fig. 4.7(c,d) by fitting the data to a second order polynomial fit and taking the value of $B_{c2}$ at $T = 0$. For $x = 0.5$, $B_{c2}^{\perp}(0) = 0.57$ T and $B_{c2}^{\parallel}(0) = 25.4$ T giving $\xi_{\parallel}(0) \sim 24$ nm and $\xi_{\perp}(0) \sim 0.54$ nm. For $x = 1.0$, $B_{c2}^{\perp}(0) = 0.28$ T and $B_{c2}^{\parallel}(0) = 20.8$ T giving $\xi_{\parallel}(0) \sim 34$ nm and $\xi_{\perp}(0) \sim 0.46$ nm. With the blocking layer thickness being $0.26$ nm, Josephson vortices are possible if $\xi_{\perp}(0)$ lies between $0.13$ and $0.26$ nm. See Fig. 4.8 for an example of how a Josephson vortex would run in the layered structure. Neither of our samples show a $\xi_{\perp}(0)$ that implies a 2D system and with it the presence of Josephson vortices.

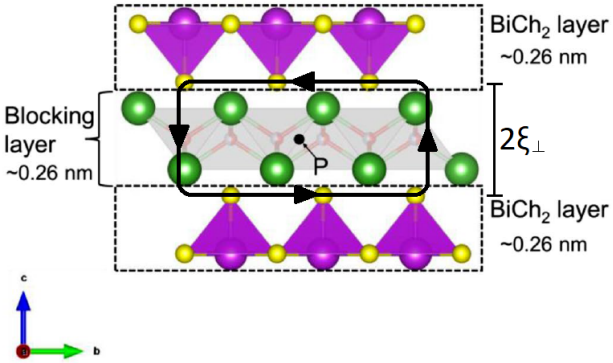


**Figure 4.8.** Schematic representation of a Josephson vortex penetrating the blocking layer with a $\xi_\perp(0)$ between 0.13 and 0.26 nm. Figured edited from Ref. [104]

The $B_{c2}(T)$ phase diagram presented in this work corresponds well to the literature when taking into account the differences in doping levels and the method of taking $B_{c2}$ values from field sweep data [103, 104]. The latter offers an explanation for the relatively large difference in $\xi_\perp$. In Ref. [104], $B_{c2}$ is defined as the intersection of the extrapolation of the $\rho_{ab}(B)$ curve and $\rho_n$ (the normal-state resistivity). In most studies, $B_{c2}$ values are estimated by taking the value of $B_{c2}$ at which the resistivity is 50% of the normal state value $\rho_n$ (the '50% criterion') [109, 119]. This is why the values of $B_{c2}$ obtained in Ref. [104] are likely overestimated, leading to underestimated values of $\xi_\perp$. Since this work uses the superconducting-to-normal transition onset values for $B_{c2}$, it is likely that the values for $\xi_\perp$ are somewhat overestimated. However, the fact that the $B_{c2}$ values for high-temperature data (samples S3-6) were already analyzed using the onsets made it – combined with the lineshapes of the temperature-dependent data of S1 – necessary to keep taking onset values for $B_{c2}$ in this work. Since the lineshapes of Fig. 4.7(b) lend themselves well to a 50% criterion analysis, we decided to compare the corresponding $B_{c2}^{\parallel}(0)$ to the $B_{c2}^{\parallel}(0)$ evaluated using the onset method. For S2, the 50% criterion gives a $B_{c2}^{\parallel}(0)$ of 24.0 T. This is more than 20.8 T, the $B_{c2}^{\parallel}(0)$ evaluated using the onset method, but gives a $\xi_\perp$ of 0.57 nm, still nowhere near the blocking layer thickness 0.26 nm. Taking all of the above into account, we consider it highly unlikely that the $\xi_\perp(0)$ of S1 or S2 is smaller than the thickness of the LaO blocking layer. With the likely underestimation of $\xi_\perp$ in Ref. [104] for $LaO_{0.5}F_{0.5}BiS_{2-x}Se_x$ ($x = 0.22$

and 0.69) and our presented values of $\xi_\perp$ for $LaO_{0.8}F_{0.2}BiS_{2-x}Se_x$ ($x = 0.5$ and 1.0), we reason that there is no presence of a complex-stripe phase in these $BiCh_2$-based superconductors.

Consequently, a possible explanation for the extremely large $B_{c2}$ of $BiCh_2$-based superconductors could be spin-triplet superconductivity. UCoGe and $UTe_2$ also exhibit large $B_{c2}$ values, showing the same kind of upturn in the $B_{c2}(T)$ phase diagram without subsequent downturn [120, 121]. In conventional Rashba superconductors that possess global inversion symmetry, spin-singlet and spin-triplet states can be mixed in the superconducting phase [122, 123]. It has also been shown that, in theory, a mixed-parity state can be achieved in a material by breaking the local inversion symmetry [124]. $BiCh_2$-based systems have been proposed to be one of these mixed-parity superconductors with a dominant triplet component and a subdominant singlet component [125]. This kind of mixture is also incompatible with the complex-stripe phase, as the latter can only emerge in spin-singlet systems without a mixture of spin-triplet superconductivity [126]. However, $BiCh_2$-based systems would be unique in that they would be the first parity-mixed superconductors that *are* centrosymmetric, or a 2D system [122, 123]. This keeps the $BiCh_2$-based superconductors in the spotlight and warrants more research with the aim to fully understand the role of local inversion symmetry breaking in the formation of the superconducting state.

## 4.4 Conclusion and outlook

We have reported a high magnetic field study of the $B_{c2}$ of $LaO_{0.8}F_{0.2}BiS_{2-x}Se_x$ ($x = 0.5$ and 1.0) with the aim to characterize this material family and learn more about the relationship between superconductivity and local inversion symmetry breaking. Specifically, we set out to examine the claim made by Hoshi *et al.* in Ref. [104] about how the Josephson vortex state (also known as the complex-stripe phase) could be the mechanism responsible for the extremely high $B_{c2}$. In that case, Josephson vortices may induce the orbital pair-breaking effect. We find that at $T = 0.35$ K our dimensionality analysis does not clearly show the materials to be best described by either 2D or 3D behavior. Our $B_{c2}(T)$ phase diagram demonstrates that the $B_{c2}$ values of both materials greatly exceed the conventional limits. Additionally, no downturn in the upwards trend in $B_{c2}$ as $T \to 0$ is observed, implying the absence of the helical phase. The calculated out-of-plane coherence lengths $\xi_\perp(0)$ are not small enough to suggest the presence of Josephson vortices.

In light of these results, we conclude that there is no presence of a complex-stripe phase in these $BiCh_2$-based superconductors. An alternative mechanism responsible for the high $B_{c2}$ in these materials could be a mixture of spin-singlet and spin-triplet superconductivity due to local inversion symmetry breaking, as also suggested by Hoshi $et\ al.$. Further research on $BiCh_2$-based systems could perhaps provide a more decisive picture regarding their dimensionality at low temperatures. Our results rule out the existence of a Josephson vortex state in these materials and thereby further narrow down the search for the mechanism responsible for the high $B_{c2}$ in $BiCh_2$-based superconductors.

# 5 Uniaxial strain effects on the Fermi surface of bulk bismuth

## 5.1 Introduction

Bismuth has proven over time to be an interesting material due its peculiar electronic properties. It has a very low carrier density, but still becomes superconducting at very low temperatures [127]. It has played an important role in the discovery of the Shubnikov-de Haas (SdH) and de Haas-van Alphen (dHvA) effects in the early 20$^{\text{th}}$ century, being the very first substance whose Fermi surface has been experimentally mapped out [50]. In combination with the Onsager relation, these effects led to the Fermi surface of most metallic elements being reconstructed by the 1970s [128]. With the analysis of topological properties of materials being a hot topic in condensed matter physics right now, bismuth again takes the stage. The band structure of bulk bismuth has a few key features: a direct band gap $E_g$ at the L point in the Brillouin zone, an indirect band gap $E_0$ at the T point and no other band crossings at the Fermi level, see Fig. 5.1 (figure adapted from [129]). Both of these gaps are inverted, meaning there is an even number of inverted gaps. This property gives rise to a topologically trivial value of the $Z_2$ invariant, leading to bulk bismuth being non-topological [130, 131]. The latter has been experimentally observed in angle-resolved photoemission spectroscopy measurements [132–134]. Transport studies performed on bismuth doped with antimony ($Bi_{1-x}Sb_x$) have demonstrated the presence of a semimetal-to-semiconductor (SMSC) [135] and a trivial to topological (TT) [4] transition, justifying the idea of bismuth being a compelling candidate for research on topological phase transitions.

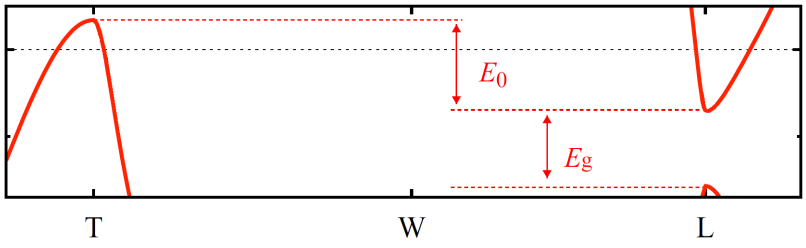


**Figure 5.1.** LDA band structure of bulk bismuth around the T and L points. The electron and hole pockets are shown together with the direct band gap $E_g$ and the indirect band gap $E_0$. Figure adapted from [129].

Local-density approximations (LDA) of DFT performed in the past have greatly overestimated the size of the band gaps of bismuth, which tends to be

a common characteristic of inverted gaps [136, 137]. Recently, quasiparticle self-consistent QS$GW$ calculations performed by Aguilera $et\ al.$ [129] have described a band structure of bismuth with gap sizes that are in a much better agreement with experiments: $E_g = 13$ and $E_0 = -33$ meV [138–144]. With the phase boundary at which bismuth becomes topologically nontrivial much closer, the paper presents that only modest amounts of 0.3 % and $-0.4$ % in-plane strain are calculated to be necessary to induce the SMSC and TT phase transition, respectively, see Fig. 5.2 [129]. With uniaxial strain being a potential tool, we aimed to experimentally explore the 3D topological properties of undoped bulk bismuth.

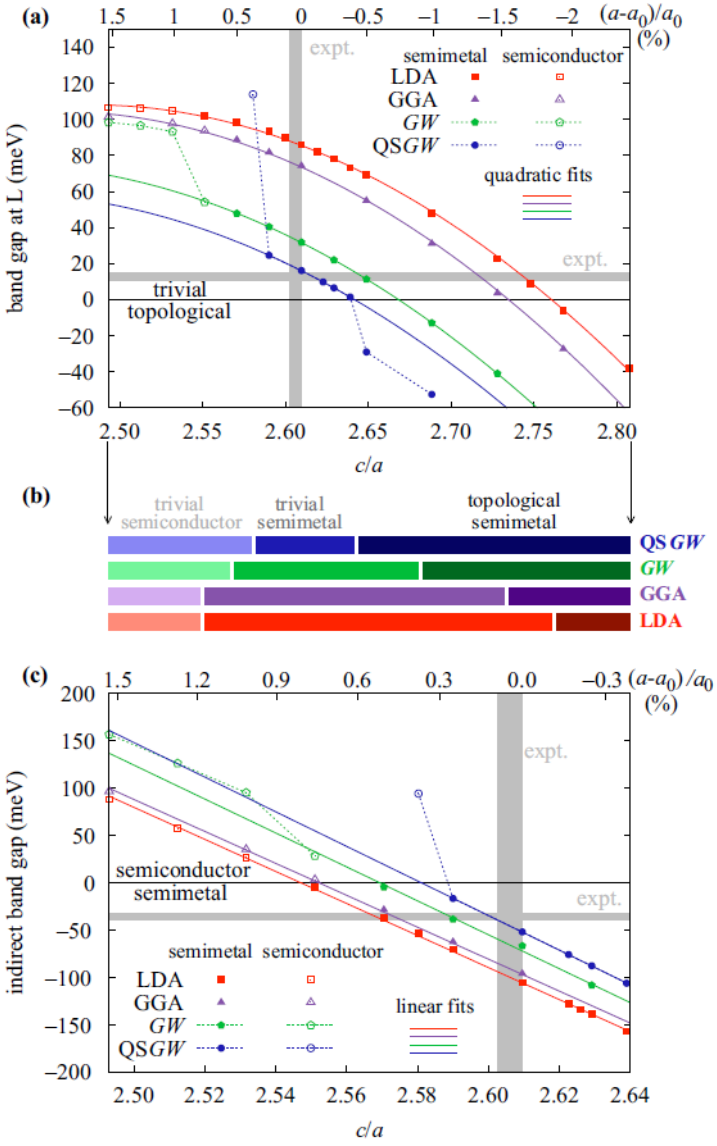


**Figure 5.2.** (a) LDA, GGA, *GW*, and QS*GW* calculations for the direct band gap $E_g$ of bulk bismuth at the L point for different in-plane strains. (b) The three relevant electronic phases as a function of strain. (c) LDA, GGA, *GW*, and QS*GW* calculations for the indirect band gap $E_0$ for different in-plane strains. Gray shaded areas represent ranges of experimental values in literature [64, 138–144]. Figure adapted from [129].

In this chapter we describe the crystal structure of bulk bismuth as hexagonal. The in-plane and out-of-plane lattice constants are $a_0$ = 4.5460 Å and $c_0$ = 11.862 Å with a $c_0/a_0$ ratio of 2.6093, measured at 298 K [64]. It owes its semimetallic character to the indirect overlap of the valence band at the T point and the conduction band at the L point. Consequently, the 3D Fermi surface of bismuth consists of three small ellipsoid electron pockets at L and one ellipsoid hole pocket at T, see Fig. 5.3. Note that the axes are defined as the binary, bisectrix and trigonal axes.

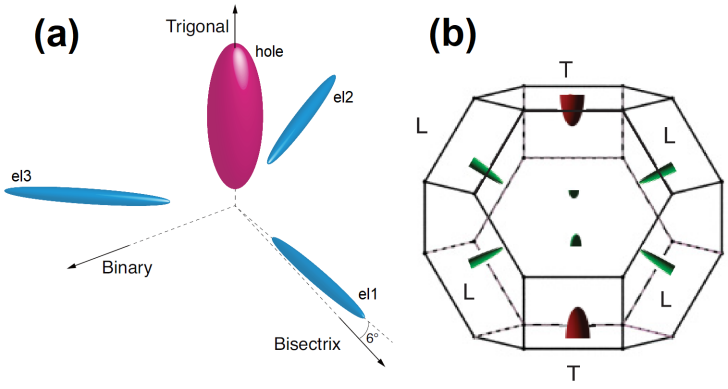


**Figure 5.3.** (a) Illustration of the 3D Fermi surface of bulk bismuth. The hole pocket in magenta is situated at the T point in the Brillouin zone along the trigonal axis. The three electron pockets in blue are situated at the equivalent L point with a $2\pi/3$ interval. The latter are tilted 6° away from the binary-bisectrix plane in the trigonal direction. Figure adapted from [145]. (b) Sketch of the Brillouin zone and Fermi surface of bismuth, with enhanced Fermi surface size to make it visible. The hole pocket is shown in red and the electron pockets are shown in green. Figure adapted from [146].

The effect of uniaxial strain on the band structure of bulk bismuth has been previously studied, yielding results that suggest large changes in extremal orbit area of the quasiparticle orbits with small amounts of strain [147, 148]. Strain-dependent shifts of the quantum limits of electron pockets have also been observed [149]. The calculations of Aguilera *et al.* [129] predict changes in the band structure – and with them, phase transitions – with strain as described earlier, however, changes in extremal quasiparticle orbit area are small for small amounts of strain. According to the calculations, 0.1 % uniaxial strain along the trigonal axis would translate to

0.0279 % in-plane strain, with no phase transition and small changes in extremal orbit area as a result (see Fig. 5.2 [129]). This makes identifying the effect of uniaxial strain on the band structure of bulk bismuth using electronic transport measurements challenging. With the existing literature data on bulk bismuth under strain being unsatisfying, we take a closer look and attempt to reproduce it before also performing a cyclotron effective mass analysis with the goal to observe small changes in the band gaps. The latter is based on a paper by Cankurtaran *et al.* [150], which concludes that the variation of the band gap at the L point has a considerable influence on the behavior of the cyclotron masses ($m_c$) of the (electron) charge carriers in semimetallic $Bi_{1-x}Sb_x$ alloys ($x < 0.07$). The authors use the Lax model (also known as the ellipsoidal non-parabolic model, ENP) [151] to link $m_c$ and $E_g$, which is described by

$$\alpha_{xx}k_x^2 + \alpha_{yy}k_y^2 + \alpha_{zz}k_z^2 + 2\alpha_{yz}k_yk_z = (2m_0/\hbar^2)E_F(1 + E_F/E_g) \quad (5.1)$$

where $x$, $y$ and $z$ refer to the binary, bisectrix and trigonal axes respectively, $\alpha_{ij}$ are the components of the inverse mass tensor $\hat{\alpha}$ for electrons from which $m_c$ can be derived and $E_F$ is the electron Fermi energy measured from the bottom of the conduction band. $m_c$ was already known to decrease with Sb doping, but it was found experimentally that $E_g$ decreases with Sb doping as well, as predicted by Golin in 1968 [152]. Hence a decrease in gap size would correlate with a decrease in cyclotron mass. Taking into account the calculations of Aguilera *et al.* [129], with uniaxial tension along the trigonal axis resulting in an in-plane compression, the strain should lead to a decrease in gap size at the L point and therefore a decrease in cyclotron mass.

We also investigated the effect of uniaxial strain on $Bi_{0.96}Sb_{0.04}$. This alloy is interesting because it slightly moves the band structure of bismuth towards that of antimony, thereby decreasing the size of both band gaps [153]. The smaller band gaps should lead to smaller strains being necessary to induce a phase transition, be it SMSC or TT.

Here we report the bulk bismuth crystal sample acquisition and characterization, followed by an attempt at reproducing literature values of 3D Fermi surface parameters. We find small systematic changes with strain, but have difficulty reproducing strain literature and linking our findings to the calculations put forward by Aguilera *et al* [129]. Larger strains exerted along the trigonal axis of both bulk bismuth and bismuth doped with antimony could shine more light on the experimen-

tal validity of the theoretical predictions and thereby the 3D topological properties of bismuth.

## 5.2 Sample acquisition and characterization

Our bismuth single crystals were obtained through Goodfellow and through MaTeck [154, 155], where they were grown using the Bridgman method. Both quotations were for single large pieces of bismuth crystal with at least 3 mm thickness (trigonal axis) and about 8 mm diameter (bisectrix-binary plane). We used the Laue x-ray back reflection method to determine the exact orientation of the bisectrix and binary axis of both crystals, see Fig. 5.4.

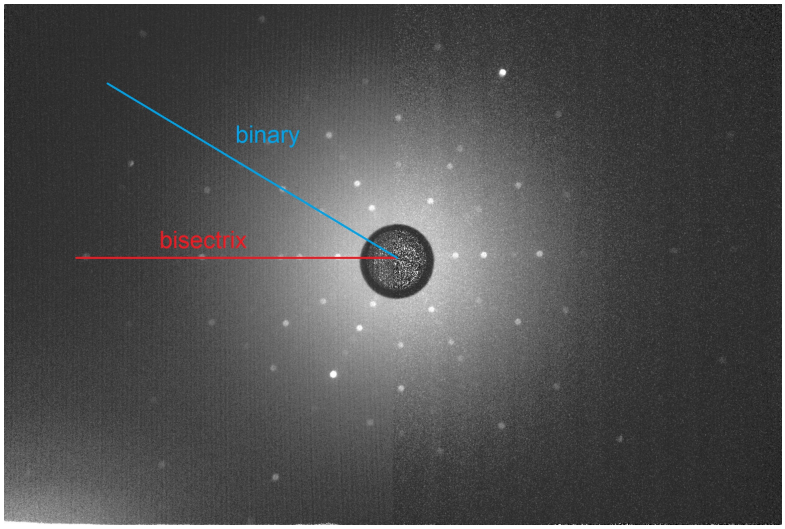


**Figure 5.4.** Laue photo made in the direction of the trigonal axis of the MaTeck bismuth crystal. The symmetric bisectrix and asymmetric binary axis are shown in red and blue, respectively.

The crystals were spark-cut into small bar-shaped samples with dimensions of $3 \times 0.4 \times 0.18\ \mathrm{mm}^3$ ($a \times b \times c$), see Fig. 5.5. Here, $a$, $b$ and $c$ correspond to different crystal axes depending on the sample, see Table 5.1. $a$ is always the strain and current flow direction, while $c$ is always the direction along which a magnetic field

is applied when measuring magnetoresistance unless measuring the dependence of the sample resistance on a varying magnetic field angle.

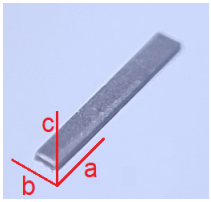


**Figure 5.5.** A photo of one of the bismuth samples with typical dimensions, labeling the $a$, $b$ and $c$ axes.

**Table 5.1.** The orientation of each sample reported in this chapter.

| | Bi#1,2,3 $Bi_{0.96}Sb_{0.04}$#1 | Bi#4,5,6,MT1,MT2 $Bi_{0.96}Sb_{0.04}$#2,4 | Bi#7 | Bi#8 $Bi_{0.96}Sb_{0.04}$#3 |
|---|---|---|---|---|
| $a$ ($\parallel \varepsilon, I$) | bisectrix | binary | trigonal | binary |
| $b$ | trigonal | trigonal | bisectrix | bisectrix |
| $c$ ($\parallel B$) | binary | bisectrix | binary | trigonal |

Because of the low carrier density of bismuth, defects can play a large role in the visibility of QOs in the magnetoresistance. In order to determine the purity of the samples and get a rough idea of the density of defects such as dislocations, the residual resistance ratio (RRR) was determined using $\mathrm{RRR} = R(300\,\mathrm{K})/R(2\,\mathrm{K})$, see Fig. 5.6 and Table 5.2. These characterization measurements were performed using a transport-measurement puck in the PPMS with the four-point probe method. The strain measurements were also performed in the PPMS, using the Razorbill CS100 strain cell as described in the experimental section of this thesis.

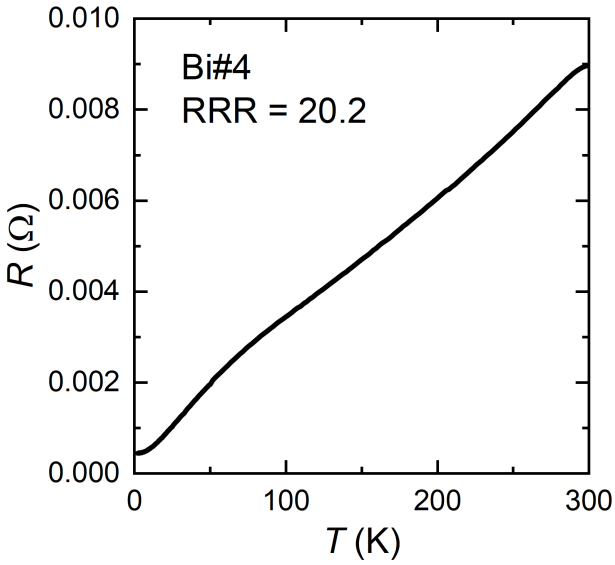


**Figure 5.6.** Temperature sweep of the resistance of Bi#4. The RRR for this sample is 20.2.

**Table 5.2.** RRRs belonging to the bismuth samples reported in this chapter.

| Bi sample | #1 | #2 | #3 | #4 | #5 | #6 | #7 | #8 | #MT1 | #MT2 |
|---|---|---|---|---|---|---|---|---|---|---|
| RRR | 7.7 | 13.1 | 8.1 | 20.2 | 8.2 | 7.3 | 8.0 | 3.3 | 22.3 | 21.9 |

The RRR values of our samples were rather disappointing compared to those in the literature obtained from the same commercial provider (MaTeck), with literature values ranging from 230 to 600 [156–158]. Perhaps the spark-cutting introduced a defect structure on the edges of the samples, which can be removed by etching. We etched a number of samples to attempt to increase the RRR by dowsing them in a solution consisting of 30 % $HNO_3$ for 2 minutes [159]. In a GoodFellow sample, this resulted in a sample with clean, shiny surfaces and increased the RRR from about 6 to 9. In our MaTeck samples, this never resulted in a RRR higher than 30. Both MaTeck samples described in this chapter (Bi#MT1,MT2) had been etched.

Our $Bi_{0.96}Sb_{0.04}$ samples were obtained from a batch of crystals grown by Yingkai Huang. The samples were spark-cut with the orientation

$a \times b \times c$ = bin × trig × bis, with the same dimensions as for the Bi samples. Three samples ($Bi_{0.96}Sb_{0.04}$#1,2,3) were characterized on the puck before being measured on both the rotator probe and the CS100 in the PPMS. See Fig. 5.7 for the cool down measurement of the resistance of $Bi_{0.96}Sb_{0.04}$#1,2,3.

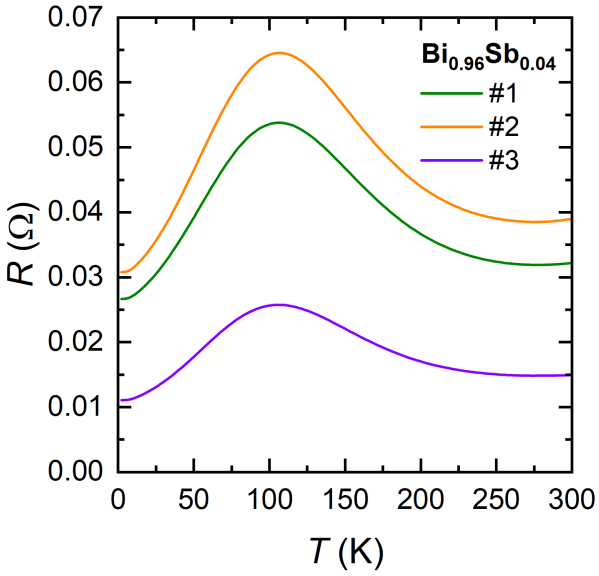


**Figure 5.7.** Temperature sweeps of the resistance of $Bi_{0.96}Sb_{0.04}$#1, #2 and #3.

## 5.3 Results and discussion

### 5.3.1 Bi QO frequencies under uniaxial strain

Fig. 5.8 shows a series of field sweeps up to 9 T of the longitudinal (along the $a$ axis) magnetoresistance of four bismuth samples with a varying orientation. The sweeps were performed under varying amounts of uniaxial strain at a temperature of 2 K. Each sample was mounted in the CS100 strain cell and positioned in the PPMS in the same manner, as described in the previous section. SdH oscillations are observed for each sample. The reason the data of these four samples are displayed is because they show the clearest QOs for their orientation. The strain values are displayed in the chronological order of the measurements performed, ending with

a zero-strain return measurement to demonstrate having stayed within the elastic regime of the samples. There are slight differences in strain values between samples due to differences in glue locations. These lead to differences in strained sample length $L$, but they are small enough to make a good qualitative comparison between the orientations.

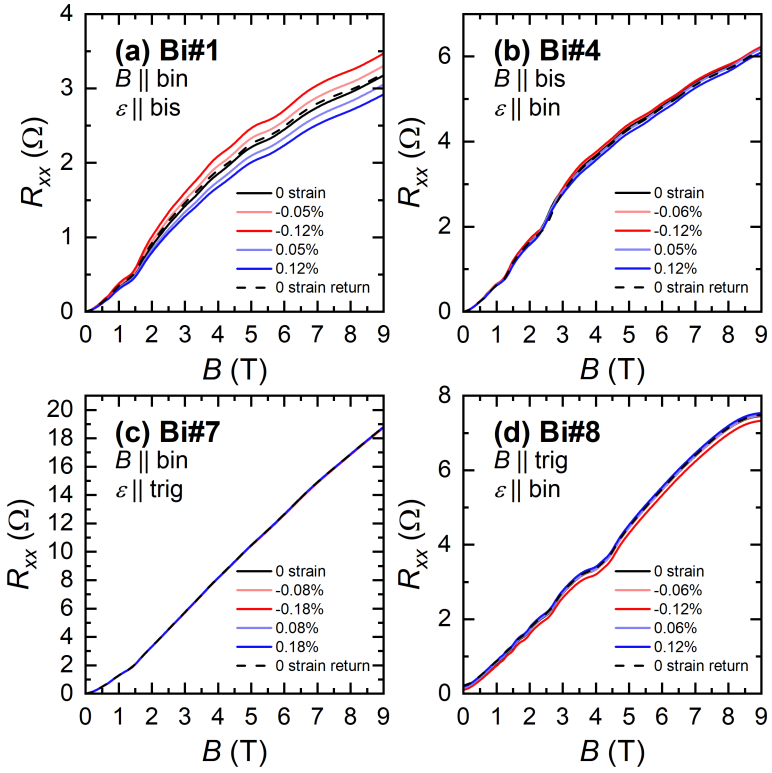


**Figure 5.8.** Field sweeps up to 9 T of the longitudinal magnetoresistance of four Bi samples, each with a different combination of field and strain orientations. These orientations are shown in Table 5.1. The temperature was held constant at 2 K. Uniaxial compressive strain is shown in red, while uniaxial tensile strain is shown in blue. A final zero strain measurement (dashed black line) consistently falls onto the solid black line and verifies having stayed within the elastic regime of the samples.

Fig. 5.9 shows the derivative of the MR series of Fig. 5.8 with respect to the inverse magnetic field against $1/B$.

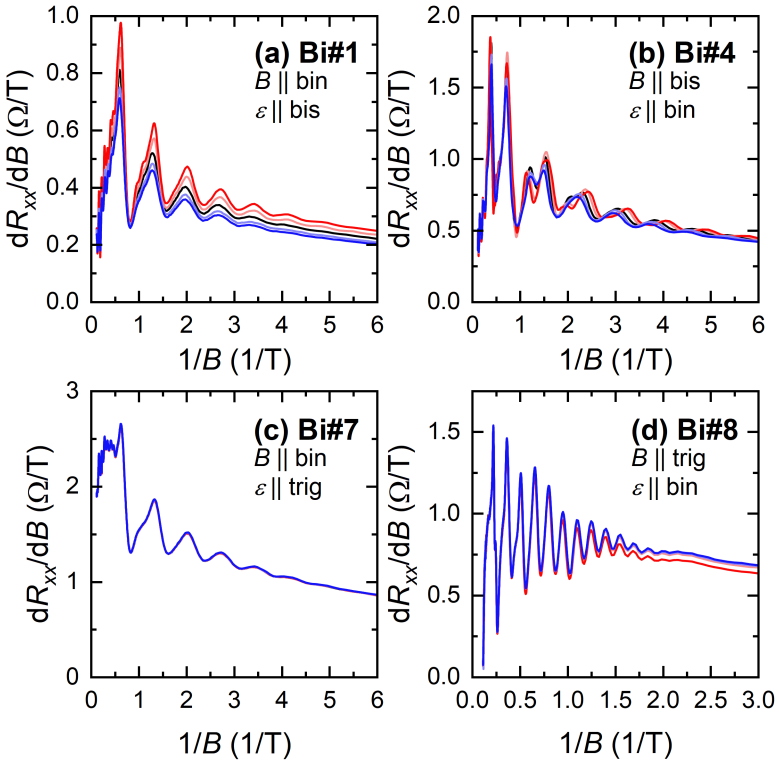


**Figure 5.9.** Derivative plots of the values for $R_{xx}$ in Fig. 5.8 against $1/B$. The same colors correspond to the same strain values. The displayed field range is 0.17 – 9 T for (a–c) and 0.33 – 9 T for (d). The curves in (c) are almost entirely overlapping.

Fast Fourier transforms (FFTs) were performed on the derivative data resulting in Fig. 5.10. The Hann window function was used and the FFT magnetic field range was varied depending on orientation and Fermi surface pockets probed. As is visible in Fig. 5.9, S1, S4 and S7 clearly show different QO frequencies in the high-field region compared to the low-field region. Ranges were chosen in a way to best analyze the peak frequencies of the pockets. For Bi#1 and Bi#7, a range of 0.2 – 9 T was used for the low-field region including electron pockets 2 and 3 (el2 and el3,

see Fig. 5.3), while a range of 1.7 – 9 T was used for the high-field region including electron pocket 1 (el1) and the hole pocket. For Bi#4, a range of 0.2 – 3 T was used for the low-field region and with it all three electron pockets, while a range of 3.3 – 9 T was used for the high-field region and with it the hole pocket. For Bi#8, only one range was used: 0.5 – 9 T to analyze all pockets. The peak frequencies obtained from Fig. 5.10 are listed in Table 5.3 in T where they are compared to literature values. These are the frequencies belonging to the zero-strain data. The first harmonic of el2 and el3 for Bi#1 and Bi#7 is clearly visible in the data but is not included in the table. The error of the frequency values is taken to be the maximum peak frequency difference between two different samples of that orientation. The literature values are shown in brackets and are the median of the different values shown in Table 1 of Bhargava *et al*. [160]. Note that the el1 and hole pockets under $B \parallel$ bin and the electron and hole pockets under $B \parallel$ trig have the same value in our data (contrary to the literature) because the width of the FFT peaks makes it impossible to distinguish two different frequencies for those pockets. With $B$ along the trigonal axis, the electron pocket frequency doesn't appear to align well with the literature, but one paper did find a frequency that lies closer to our work: 6.37 T [161]. The three largest frequency values found also appear to differ from literature values, but the reason for this discrepancy is unknown. The discrepancy is consistent among samples and is almost certainly too large to be the result of angle misalignment.

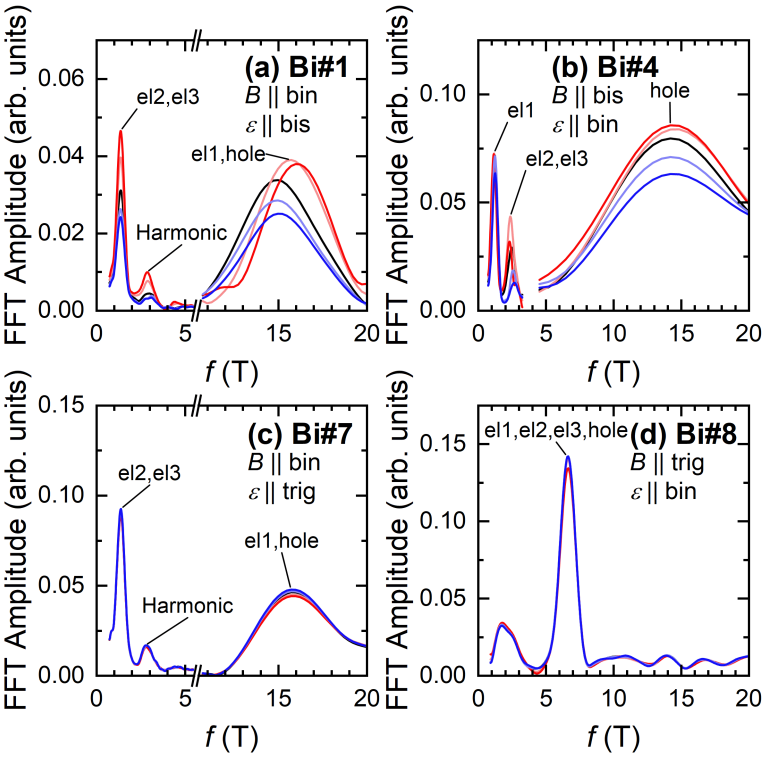


**Figure 5.10.** FFT plots of the derivative data of Fig. 5.9. The same colors correspond to the same strain values. The leader lines label the frequency peaks to their related electron and hole pockets in that orientation. FFTs taken with both low-field and high-field ranges are merged together in (a–c). Note the horizontal axis break in (a) and (c).

**Table 5.3.** Quasiparticle orbits and their oscillation frequencies in T at zero strain and three different magnetic field orientations. Literature values belonging to Ref. [160] are shown in brackets. Electron and hole pocket frequencies are in reality not exactly the same value, but differ slightly as shown in the literature values.

| | $B$ \|\| bin (T) | $B$ \|\| bis (T) | $B$ \|\| trig (T) |
|---|---|---|---|
| el1 | $15.12 \pm 0.73$ (20.41) | $1.19 \pm 0.02$ (1.22) | 6.64 (8.33) |
| el2 | $1.37 \pm 0.01$ (1.40) | $2.52 \pm 0.03$ (2.40) | 6.64 (8.33) |
| el3 | $1.37 \pm 0.01$ (1.40) | $2.52 \pm 0.03$ (2.40) | 6.64 (8.33) |
| hole | $15.12 \pm 0.73$ (20.83) | $13.27 \pm 0.98$ (20.83) | 6.64 (6.35) |

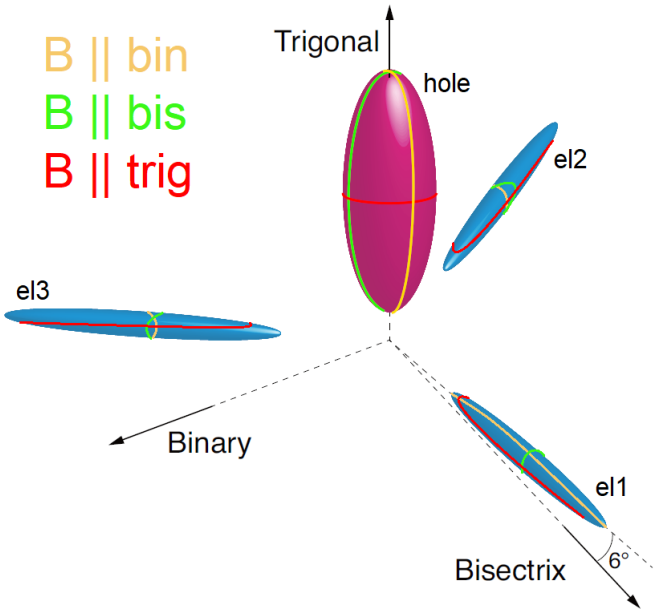


**Figure 5.11.** Illustration of Fig. 5.3(a) showing the 3D Fermi surface of bulk bismuth, with extremal orbit areas of Table 5.3 in different colors. A larger oscillation frequency corresponds to a larger extremal orbit area.

Two strain-induced effects can be seen in the FFTs of Fig. 5.10. The first effect is an apparent increase in FFT amplitude with in-plane compressive strain and decrease with in-plane tensile strain for Bi#1 and Bi#4. The inverse happens when

these strains are applied along the out-of-plane direction like in Bi#7. As discussed in the ZrSiS chapter, this change in FFT amplitude can perhaps be attributed to changes in the quantum mobility for the orbits. The effect of these strains on the $c/a$ ratio is in line with the reasoning: in-plane compressive strain increases the ratio, thereby increasing the quantum mobility, while out-of-plane compressive strain decreases the ratio, thereby decreasing the quantum mobility.

The other strain-induced effect is the frequency shift visible for the el1/hole peak of Bi#1 and the el2/el3 peak of Bi#4. The latter appears to be a small systematic shift, but attempts to reproduce this result did not succeed. On the contrary, the relatively large systematic shift for the el1/hole peak in Bi#1 was observed in every sample of that orientation. Fig. 5.12 shows this frequency shift for Bi#1, 2 and 3. As this peak is linked to the frequency of both the el1 and hole pockets, it is unclear which of the two is responsible for the shift. Bi#4 does not show signs of its hole pocket frequency changing with strain, so due to the rotational symmetry of the hole pocket it would be intuitive to designate responsibility of the shift to el1. However, if the hole pocket frequency would remain the same while that of el1 would change, peak splitting would be expected. No peak splitting is observed in the el1/hole peak of Bi#1. This may perhaps be because the shift is too small to sufficiently pull the two peaks apart for the FFT to not visualize them as a single peak. A higher quality sample could improve peak prominence enough for these peaks to be visualized separately. In any case, our measurements don't correspond at all to those obtained by Brandt *et al*. [148], where changes in extremal orbit areas of up to 40 % are observed with an application of only 0.11 % in-plane uniaxial tension.

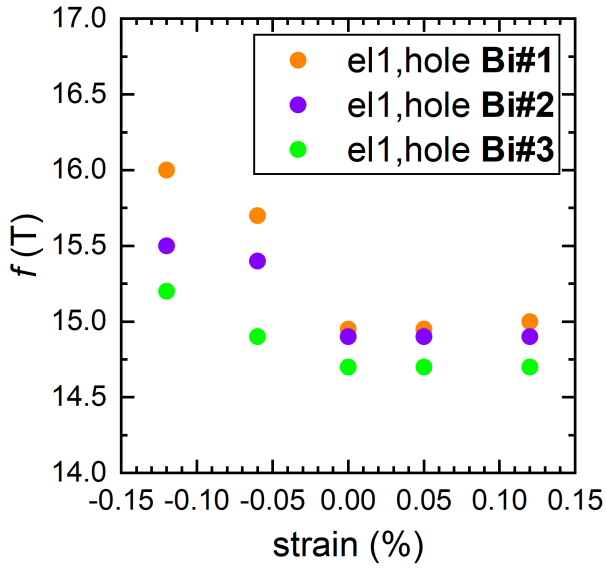


**Figure 5.12.** Frequency shift with uniaxial strain of the peak related to the el1/hole pockets of the samples Bi#1, #2 and #3. The direction of $B$ is along the binary axis, while uniaxial strain is applied along the bisectrix.

In order to compare our data to that of Hosoi *et al.* [149], we took the second derivative of the MR series of Fig. 5.8 with respect to the inverse magnetic field, see Fig. 5.13. We were not able to reproduce the data of Hosoi *et al.* shown in Fig. 5.13(b), as we find an opposite change in oscillation amplitude with compression and tension, and we don't see a change in the quantum limit of the e2/e3 pockets. This is also evident from our FFT data (Fig. 5.10(a)), as we don't see a frequency shift in the peak belonging to those pockets. The shift in the quantum limit to a lower inverse magnetic field demonstrated by Hosoi *et al.* implies an enlarging e2/e3 pocket which would show itself in the frequency peak spectrum.

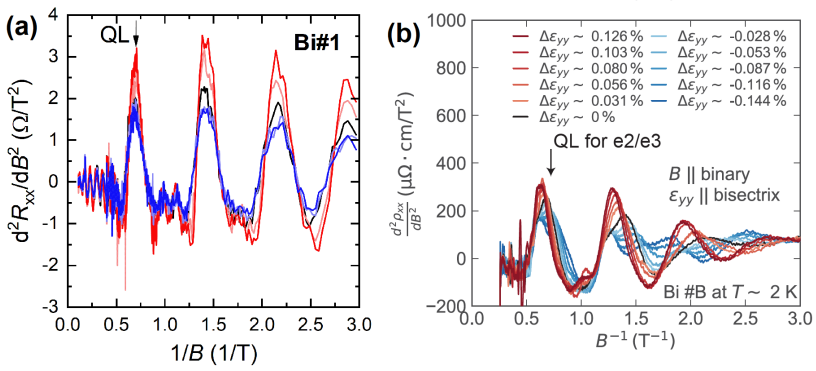


**Figure 5.13.** (a) Second derivative plots of the values for $R_{xx}$ in Fig. 5.8 against $1/B$. The same colors correspond to the same strain values. The quantum limit of the el2/el3 pockets is indicated by the left-most large peak, here 0.69 $1/T$ (or 1.45 T). The direction of $B$ is along the binary axis, while uniaxial strain is applied along the bisectrix. (b) The same plot as in (a) but with data obtained by Hosoi *et al.* Adapted from Ref. [149]. An important note is that (a) and (b) use opposite colors to describe strain amounts: in (a) red means compression, while in (b) red means tension.

### 5.3.2 Bi cyclotron masses under uniaxial strain

A cyclotron effective mass analysis was performed on Bi#6 and Bi#MT2. Fig. 5.14(a) shows the temperature dependence of the low-field FFT peaks of Bi#6 under 0.12 % uniaxial compression along the binary axis, which includes the el1 peak and the el2/el3 peak. The Hann window function was used and the FFT magnetic field range was 0.2 – 9 T. The FFT peak amplitudes of Fig. 5.14(a) and all other strain values of Bi#6 are fit with the Lifshitz-Kosevich formula to produce Fig. 5.14(b). Note that for the el2/el3 peak only the uniaxial compression data offered prominent enough peaks to perform a cyclotron mass analysis on. The $m_c$ values obtained from these fits are shown in Fig. 5.14(c). Here, the $m_c$ values for Bi#6 are shown in purple and for Bi#MT2 in orange. The el2/el3 peak of the latter was also not prominent enough for an $m_c$ analysis. It also appears that the $m_c$ of the el1 pocket of Bi#MT2 does not change with uniaxial strain along the binary axis. On the other hand, the $m_c$ values of both el1 and el2/el3 of Bi#6 do appear to systematically change with that same strain, though only by small amounts.

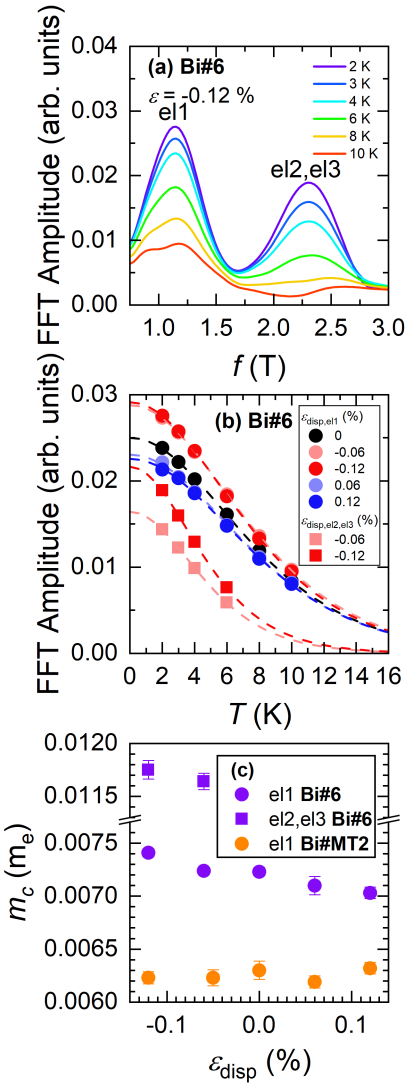


**Figure 5.14.** (a) FFT plot for Bi#6 at a uniaxial compresion of -0.12 % and varying temperature. The direction of $B$ is along the bisectrix, while uniaxial strain is applied along the binary axis. (b) Lifshitz-Kosevich fitting of the FFT peak amplitude values of both peaks in (a), including other strain values. The amplitudes belonging to the el1 peak are shown as circles while those belonging to the el2/el3 peak are shown as squares. Red means uniaxial compression and blue means uniaxial tension. (c) Cyclotron masses under uniaxial strain of the el1 and el2/el3 peaks of both the Bi#6 data shown in (a,b) (purple) and of Bi#MT2 (orange). In both samples the direction of $B$ is along the bisectrix, while uniaxial strain is applied along the binary axis.

Our results are again not reconcilable with those of Brandt *et al.* [148], as their work describes a 50 % increase in the $m_c$ of the el1 pocket with only 0.15 % uniaxial tension in the same orientation. If going by the work of Cankurtaran *et al.* [150], the decrease we found in $m_c$ of the el1 pocket of Bi#6 with in-plane uniaxial tension would supposedly mean an increase in gap size at the L point. This is contrary to the work of Aguilera *et al.* [129], where a decrease is predicted. However, the observed change in $m_c$ of Bi#6 was not reproducable in Bi#MT2. We note that the calculations performed by Aguilera *et al.* assume a constant volume, which is in reality not the case. Additionally, in the work of Aguilera *et al.* the strain is uniformly in-plane, whereas the strain in our $m_c$ analysis is uniaxially in-plane. We aimed to perform another $m_c$ analysis using the same orientation as Bi#7, but the PPMS being out of order for the remainder of the project prevented this from being achieved. The Bi#7 sample did not show any significant changes in the resistance data with uniaxial strain along the trigonal axis, so there is little reason to assume an $m_c$ analysis of another sample with this orientation would be fruitful, though.

### 5.3.3 $Bi_{0.96}Sb_{0.04}$ QO frequencies under uniaxial strain

Fig. 5.15(a) shows the longitudinal magnetoresistance up to 9 T of three different $Bi_{0.96}Sb_{0.04}$ orientations. The sweeps were performed in the PPMS on a sample puck at 2 K without any strain. SdH oscillations are observed, but only for the hole pocket. This is in agreement with the literature, as the electron pockets of bulk bismuth are expected to disappear completely with 3.45 % Sb doping [150]. The increased hole pocket size displayed in Fig. 5.15(c) with Sb doping compared to undoped bismuth can be attributed to the change in the Fermi energy, which is determined by the charge neutrality [162].

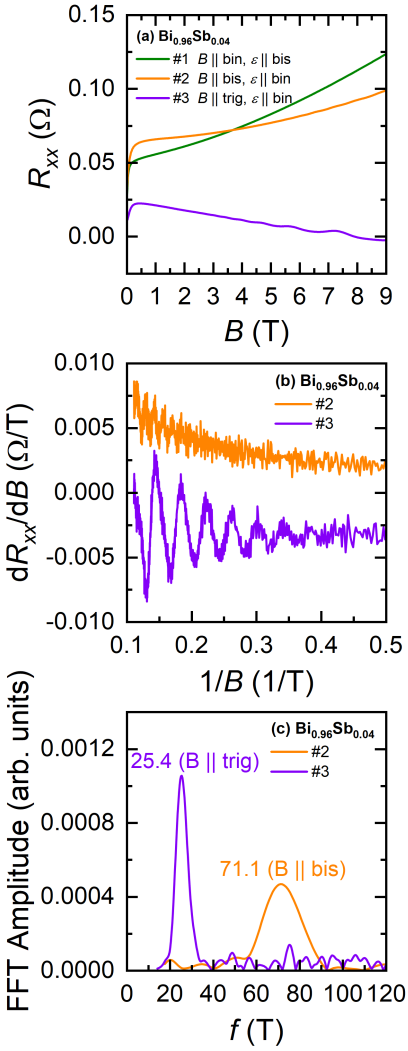


**Figure 5.15.** (a) Field sweeps up to 9 T of the longitudinal magnetoresistance of three $Bi_{0.96}Sb_{0.04}$ samples, each with a different combination of field and strain orientations, though no strain has been applied in these measurement runs. The experimental configurations are shown in Table 5.1. The temperature was held constant at 2 K. (b) Derivative plots of the values for $R_{xx}$ of sample #2 and #3 in (a) against $1/B$. (c) FFT plot for the derivative data of #2 and #3 in (b). Both of the peaks shown correspond to the hole pocket of the related sample.

Fig. 5.16 shows the dependence of the hole pocket frequency on the magnetic field angle in the bisectrix-trigonal plane for $Bi_{0.96}Sb_{0.04}$#2, with the current along the binary axis. The maximum frequency lies along the bisectrix with $76.1 \pm 1.1$ T and the minimum frequency along the trigonal axis with $26.8 \pm 0.13$ T. In order to see if the hole pocket has retained its elliptical shape, we fit the data to the polar form of the ellipse equation:

$$r(\theta) = \frac{ab}{\sqrt{(bcos(\theta + x))^2 + (asin(\theta + x))^2}} \tag{5.2}$$

where $r(\theta)$ is the radius of the ellipse measured from its center with $\theta$ measured from the long axis, $a$ the long axis diameter, $b$ the short axis diameter, and $x$ a correction to the orientation. The value for $x$ found by our fit is $4.6 \pm 0.4$ degrees. This is a plausible angle mismatch when considering sample preparation and strain cell probe mounting. The data corresponds well to the literature, with a slightly larger hole pocket than data of $Bi_{0.97}Sb_{0.03}$ from de Boer *et al.* and a similar long/short axis ratio of 2.8 (see Fig.S2(c) of Ref. [163]).

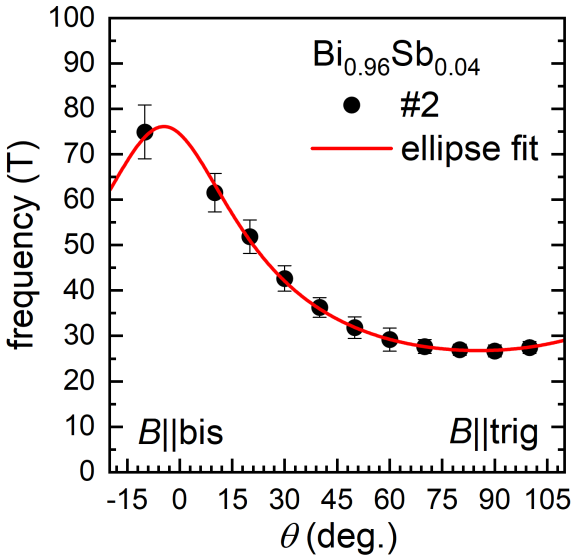


**Figure 5.16.** The hole pocket frequency of $Bi_{0.96}Sb_{0.04}$#2 against magnetic field angle, rotated in the bisectrix-trigonal plane. No strain has been applied.

Fig. 5.17 shows the samples $Bi_{0.96}Sb_{0.04}$#2 and #4 under uniaxial strain along the binary axis at a temperature of 2 K. An opposite systematic change in FFT amplitude with strain is found when compared to undoped bismuth with the same orientation. No significant frequency shift with strain is observed at these strain amounts. The difference in hole pocket frequency compared to the previous measurements on the same sample #2 can be attributed to an angle mismatch, but the change from 76.1 to 49 T would imply a 16.6 degree mismatch which is large. $Bi_{0.96}Sb_{0.04}$#4 also shows this 'lowered' hole pocket frequency. Electron pocket frequencies are absent for both samples, implying no phase transition has taken place.

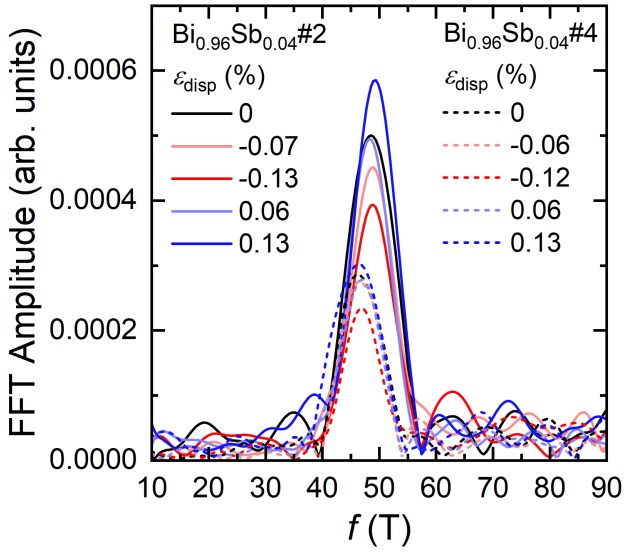


**Figure 5.17.** FFT plots of uniaxial strain data of $Bi_{0.96}Sb_{0.04}$#2 and #4, at a temperature of 2 K. All peaks belong to the same hole pocket of each sample. Red means uniaxial compression and blue means uniaxial tension. The direction of $B$ is along the bisectrix, while uniaxial strain is applied along the binary axis.

## 5.4 Conclusion and outlook

We have reported a uniaxial strain study on bulk Bi and $Bi_{0.96}Sb_{0.04}$ that aimed to bridge previous experimental works [148, 149] and theoretical data [129], thereby shining light on the 3D topological properties of bismuth under strain. Two systematic strain effects were observed, the first of which is a change in FFT amplitude attributed to a change in quantum mobility. The second effect is a frequency shift in the el1/hole peak of bismuth strained along the bisectrix with the field direction along the binary axis, likely due to a change in the el1 pocket size. This would imply a lifting of the electron pocket degeneracy which is in line with the literature. However, other experimental strain literature results could not be reproduced. The evolution of the electron and hole pockets with Sb doping is shown to correspond well to literature, but no strain effects are observed in $Bi_{0.96}Sb_{0.04}$. With no apparent TT or SMSC phase transitions in either Bi or $Bi_{0.96}Sb_{0.04}$, further work on this subject is required to fully elucidate the 3D topological properties of strained

bismuth. DFT calculations that do not assume the volume to stay constant are of interest, while experimentally higher strain values (3x) could corroborate our found systematic effects. Better sample quality through perhaps annealing could offer a more accurate FFT analysis. Finally, a strain study on different Sb doping amounts such as $Bi_{0.97}Sb_{0.03}$ could be more helpful in demonstrating the strain tunability of the band structure of bismuth.

# 6 Explorative uniaxial strain studies on selected quantum materials

## 6.1 Introduction

There are a number of materials that we have performed strain measurements on that did not yield sufficiently compelling results to warrant their own chapter. All experiments were done on single crystalline samples with dimensions that allowed for mounting onto the Razorbill CS100 or CS120 uniaxial strain cells, using either the conventional or bowtie mounting method. Crystals were acquired either through crystal growth at the Van der Waals-Zeeman Institute by dr. Yingkai Huang, through collaborations with external crystal growers, or purchased from HQ Graphene [164]. The decision to study these specific materials was driven by two main reasons. Firstly, most were motivated directly by interesting results in the literature. Secondly, some materials were chosen simply because they were readily available and/or already extensively studied by our research group.

Careful investigation of the materials in this chapter has the potential to shine light on the interplay between the superconducing and charge density wave phase ($NbSe_2$, $ZrTe_3$), in-situ strain tunability of phase transitions ($IrTe_2$), uniaxial strain effects on the (quantum) mobility of nodal-line semimetals (ZrSiTe), superconducting-domain engineering of nematic superconductors ($LaO_{0.8}F_{0.2}BiSSe$), and magnetic and electronic properties of fundamental materials (graphite). It is noted that we also performed uniaxial strain measurements on $Sr_{0.17}Bi_2Se_3$ and $ZrTe_5$. However, the results of these two studies are omitted. Results of the former reflected the minute effects and insignificant character of the results obtained in the strain study described in Ref. [165], while the brittle, needle-like crystal property of our $ZrTe_5$ samples made it so they did not lend themselves well enough to uniaxial strain measurements in the Razorbill strain cells. Recent uniaxial strain experiments performed by Schindler *et al.* have nevertheless been successful, demonstrating strain tunability of the chemical potential shift in $ZrTe_5$ [166].

It was found that, relative to the literature, results of the studies described in this chapter generally display insignificant strain effects. In the case of $NbSe_2$, this is directly in disagreement with the literature [167]. Reasons for inconsistency between hypothesis and results mentioned in this chapter are the possibility that the sample experiences insufficient strain to display the expected behavior, the crystal softness prevents proper uniform distribution of the applied stress, or that the hypothesis is in a way flawed.

## 6.2 $2H$-$NbSe_2$

### 6.2.1 Background

$2H$-$NbSe_2$ is a transition metal dichalcogenide (TMD) with a layered hexagonal crystal structure, see Fig. 6.1. Charge order observed in high-$T_c$ cuprate superconductors such as YBCO [19] has led to TMDs being suggested to serve as a platform for charge order research [168], particularly $NbSe_2$. $NbSe_2$ exists in several different forms, but bulk $NbSe_2$ generally crystallizes into the most stable $2H$ phase. Here, $H$ stands for hexagonal and 2 refers to the number of Se-Nb-Se layers in a unit cell. In this chapter we deal with $2H$-$NbSe_2$ and will from now on refer to it simply as $NbSe_2$. When cooling, a charge density wave (CDW) distortion emerges below $T_{cdw} = 33$ K due to strong electron-phonon coupling [14], followed by a superconducting phase below $T_c = 7.2$ K. The charge-ordered phase is threefold rotationally symmetric and consists of $3 \times 3$ supercells. Charge density waves and superconductivity both are Fermi surface instabilities and low-$T$ collective orders in solids. They are commonly believed to compete with each other [18, 169].

Recent studies utilizing scanning tunneling microscopy (STM) demonstrated the strain tunability of the charge-ordered phase, reporting a change from tridirectional ('3Q') to unidirectional ('1Q') charge ordering with strain [170, 171]. The stability of both of these ordering geometries is detailed in a model for the charge density wave order in $NbSe_2$ developed by Flicker and van Wezel [172, 173]. The model allowed for the authors to fully reproduce available experimental observations, including STM uniaxial strain results. It predicts that externally applied uniaxial strain contributes anisotropically to the phonon energy and that in-plane bulk strains in the order of 0.1 % are enough to transition from 3Q to 1Q charge ordering. With a quantum critical transition between the two charge order geometries in such close vicinity, the usefulness of $NbSe_2$ as a model system is reaffirmed.

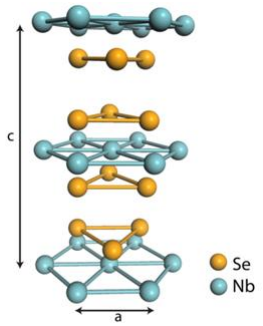


**Figure 6.1.** Crystal structure of 2$H$-$NbSe_2$. The relevant crystal axes $a$ and $c$ are displayed. Figure adapted from Ref. [174].

Recent research performed by Wieteska *et al.* aimed to corroborate the aforementioned model through electronic transport measurements of uniaxially strained $NbSe_2$ single crystals [175]. It was found that $T_c$ did not change with in-plane compressive (tensile) strains smaller than 0.1 % (0.2 %), but that it decreased strongly with larger strains at a rate of 2.5 K/% (1.3 K/%). No significant change in $T_{cdw}$ is observed. The authors additionally performed density functional theory calculations, the result of which suggests that the 1Q charge-ordered phase introduces a larger CDW gap in the for BCS superconductivity most relevant Fermi surface pocket than in the 3Q phase. Applying uniaxial strain and thereby transitioning to 1Q charge ordering would thus lead to a lower density of states at the Fermi level, consequently leading to a decrease in $T_c$. The absence of a change in $T_{cdw}$ is attributed to insufficient measurement sensitivity. The findings for $T_c$ are reconcilable with the model of Flicker and van Wezel, but the model predicts an increase in $T_{cdw}$ of about 1 K with 0.05 % in-plane uniaxial compression and 2 K with 0.05 % in-plane uniaxial tension [173], which Wieteska *et al.* did not confirm in their measurements.

The aim of the study described in the remainder of this subsection was to reproduce the results obtained by Wieteska *et al.*, as they show a relatively substantial effect on the $T_c$ of $NbSe_2$. Additionally, a change in $T_{cdw}$ with strain could perhaps be observed.

### 6.2.2 Results

Laue diffraction was performed on a $NbSe_2$ single crystal provided by dr. V. Sirenko of the Verkin Institute in Kharkov, Ukraine, in order to identify the $a$ axis, see Fig. 6.2. The crystals were then cut into $1.5 \times 0.5 \times 0.1$ mm$^3$ ($l \times w \times t$) bars along the $a$ axis and subsequently characterized with a 300 to 2 K cool down resistance measurement on a PPMS sample puck inside the PPMS. The cutting of the crystals was done using a scalpel, as the sparkcutter failed to make clean cuts through the rather soft crystal. The three best performing samples were carefully lifted from the puck and then mounted on the CS100 strain cell one at a time.

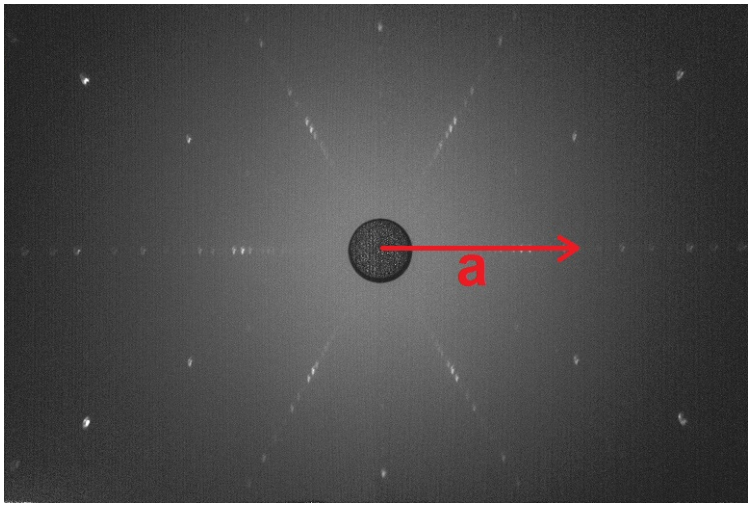


**Figure 6.2.** Laue backscattering diffraction image of a $NbSe_2$ single crystal used for sample orientation. The red arrow indicates the $a$ axis of the crystal. The direction of the $c$ axis is normal to the image.

Fig. 6.3 shows the superconducting transition in the $R(T)$ curve of each of the three samples, at various amounts of uniaxial strain along the $a$ axis. The direction of the current was parallel to the strain direction. No significant change in $T_c$ is observed in our strained samples. Only sample 1 shows a strain effect that can be deemed systematic, with $-0.26$ % compression leading to an increase of $T_c$ of 0.03 K from 7.26 K at zero strain and 0.28 % tension leading to a decrease of $T_c$ of 0.01 K. Similar strain values in the work of Wieteska *et al.* led to substantial

decreases of about 0.7 and 0.4 K, respectively [175]. See Fig. 6.4 which displays the strain dependence of $T_c$ for our sample 1 and the samples of Wieteska *et al.* [175].

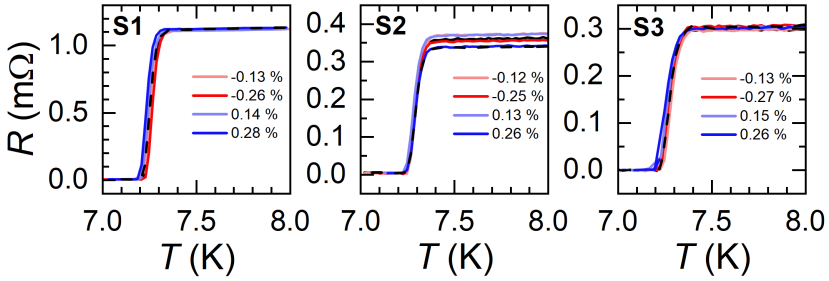


**Figure 6.3.** $R(T)$ curves of three $NbSe_2$ single crystal samples showing the superconducting transition $T_c$. The uniaxial strain is applied along the $a$ axis, parallel to the current direction. Compression is shown in red, tension is shown in blue. The solid black curve is the first zero strain measurement in the measurement series, the dashed black curve is the last.

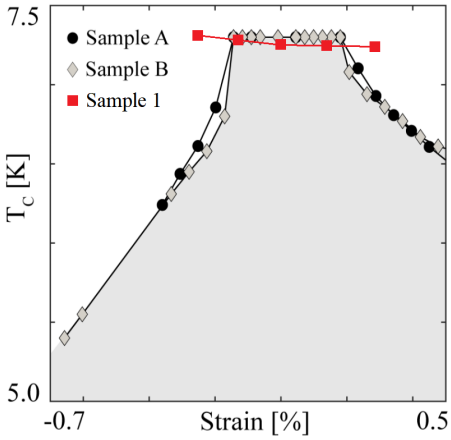


**Figure 6.4.** Strain dependence of $T_c$ for two samples of Wieteska *et al.* (black and grey) and our sample 1 (red). Figure adapted and edited from Ref. [175].

Fig. 6.5 shows the charge density wave transition in the first derivative of the resistance data of sample 3. The clear visibility of the transition in the resistance data reaffirms the high quality and low amount of disorder of the samples [21]. The

shape of the resistance curve features a small increase in resistance as it enters the CDW phase, which is attributed to a lowered density of states at the Fermi level due to the opening of the CDW gap described previously [173, 175]. No significant change in $T_{cdw}$ is observed. As mentioned in the previous section, the model of Flicker and van Wezel predicts an increase in $T_{cdw}$ with strain. Taking the relevant strain values of $-0.27$ % and $0.26$ %, this is predicted to lead to an increase in $T_{cdw}$ of between 8 and 12 K. With the prominent transition, our measurement sensitivity is easily sufficient to conclude that there is no such shift in $T_{cdw}$ in our sample.

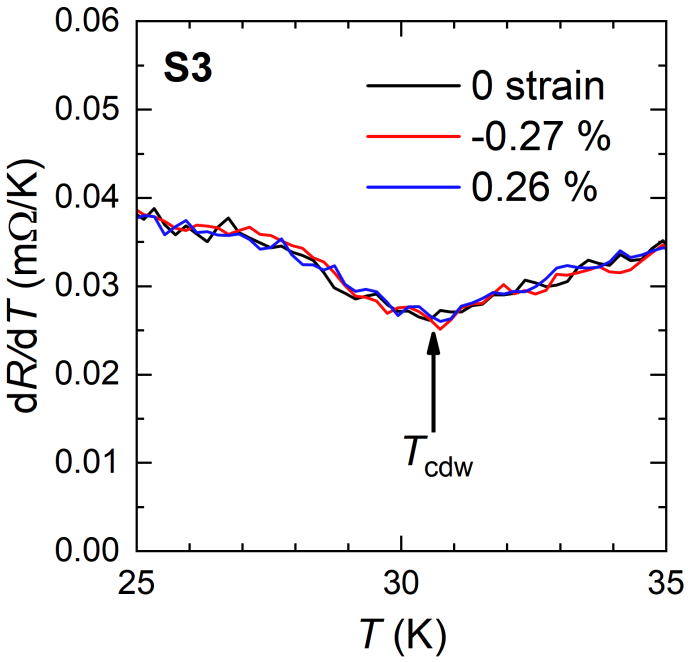


**Figure 6.5.** First derivative of the $R(T)$ curve of $NbSe_2$ sample 3 between 25 and 35 K showing the charge density wave transition $T_{cdw}$. This data was obtained in the same measurement run as the data for sample 3 shown in Fig. 6.3.

The data provided by the measurements performed in this study cannot be reconciled with that shown in Wieteska *et al.*, as no significant shift in $T_c$ with strain is found. A predicted shift in $T_{cdw}$ is also absent in our data, while a significant

shift is predicted by the model of Flicker and van Wezel [173]. A possible explanation for this could be the softness of the layered $NbSe_2$ crystal, leading to applied uniaxial stress not properly and uniformly straining the sample. Wieteska *et al.* did not comment on softness problems.

A few remarks should be made. Firstly, additional strain measurements have been performed in our group on different $NbSe_2$ samples of the same batch by bachelor student Steven Levelt, this time using the larger CS120 cell [176]. The same type of measurement was performed with strains up to $\pm 0.4\,\%$. Still, no shift in $T_c$ or $T_{cdw}$ was observed. Secondly, more strain measurements have been independently performed on a different batch of $NbSe_2$ single crystals by Jasper Linnartz at the Radboud University in Nijmegen. The same type of strain cell (CS100), sample dimensions and strain direction were used, again resulting in no significant changes in resistance data (J. Linnartz and S. Wiedmann, private communication). Lastly, we note that the work of Wieteska *et al.* that dates from 2019 is at the time of writing still only available on arXiv. Attempts to establish correspondence for an exchange of results have gone unanswered.

## 6.3 $IrTe_2$

### 6.3.1 Background

$IrTe_2$, like $NbSe_2$, is a transition metal dichalcogenide. It has a trigonal structure with the space group $P\bar{3}m1$. $IrTe_2$ is predicted to be a Dirac semimetal with a Dirac point slightly above the Fermi level [177], implying high tunability of its electronic behavior. When cooling down from room temperature, $IrTe_2$ undergoes a structural phase transition into a charge-ordered monoclinic (C2/m) phase below $T_s = 280$ K [178–180]. Unlike in $NbSe_2$, the structural transition to charge-ordered phases in $IrTe_2$ is not attributed to the formation of CDWs, but instead to Ir–Ir dimer formation [179, 181, 182], as a CDW gap is not found in experimental studies [183–185], and $IrTe_2$ lacks the typical sinusoidal structure modulation [186]. When cooling down further, more charge-ordered phases are additionally introduced, characterized by their reciprocal space modulation vector $\mathbf{q} = (1/n, 0, -1/n)$. Here, $n$ varies according to $n = 3m+2$ $(m = 1, 2, 3, ...)$. With decreasing temperature $m$ increases and thereby the amount of dimers and coexisting charge-ordered phases. However, when the temperature approaches zero the pattern breaks and $n = 6$ becomes the stable charge-ordered phase, see Fig. 6.6

for the most relevant crystal structures. This q6 phase, better known as the $6 \times 1$ phase, is proposed to be the ground state of $IrTe_2$ and is typically very difficult to observe experimentally. In this phase, dimer formation and with it Ir to Te charge transfer are maximized, resulting in unidirectional charge order and a Lifshitz transition that allows for access to bulk-Dirac-like states [167, 179, 187–189]. In the work of Nicholson *et al.* uniaxial tension along the $a$ axis of $IrTe_2$ is shown to stabilize the $6 \times 1$ phase at room temperature, allowing for it to be studied spectroscopically and demonstrating the power of strain as a tuning parameter that influences phase transitions and topology in 2D-like semimetals [167].

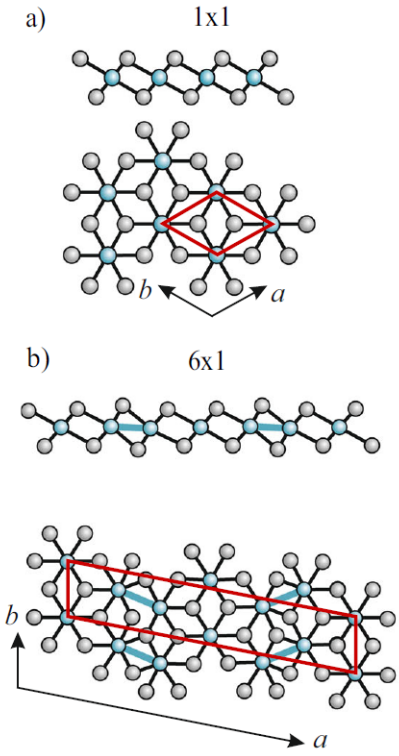


**Figure 6.6.** Crystal structure of $IrTe_2$. The top and side views are shown of the (a) room temperature ($1 \times 1$) phase and (b) the stable charge-ordered ($6 \times 1$) phase. The unit cells are marked by red lines. In (b), the formation of Ir-Ir dimers is depicted with blue lines. Adapted from Nicholson *et al.* [167].

Research performed by Pyon *et al.* has demonstrated that a stabilized superconducting phase at $T = 3.1$ K can be induced by suppressing dimer formation through Pt doping ($Ir_{1-x}Pt_xTe_2$ with $x \geq 0.04$), see Fig. 6.7 [190, 191]. In transport data, the structural transition at 280 K is shown to be pushed down to lower temperatures through the doping [183, 191]. Eventually the transition does not take place at all anymore and the superconducting phase is stabilized, signifying the absence of dimers alltogether and with it the absence of charge-ordered phases, thus validating the existence of competition between charge order and superconductivity [167, 182, 192]. It was proposed by Nicholson *et al.* that contrary to uniaxial tension which was found to stabilize the charge ordered ground state, uniaxial compression along the $a$ axis may stabilize superconducting behavior instead [167]. This would imply strain tunability of the superconducting phase in $IrTe_2$, mimicking the effect of Pt doping and further elaborating the understanding of uniaxial strain as a tuning parameter in topological materials.

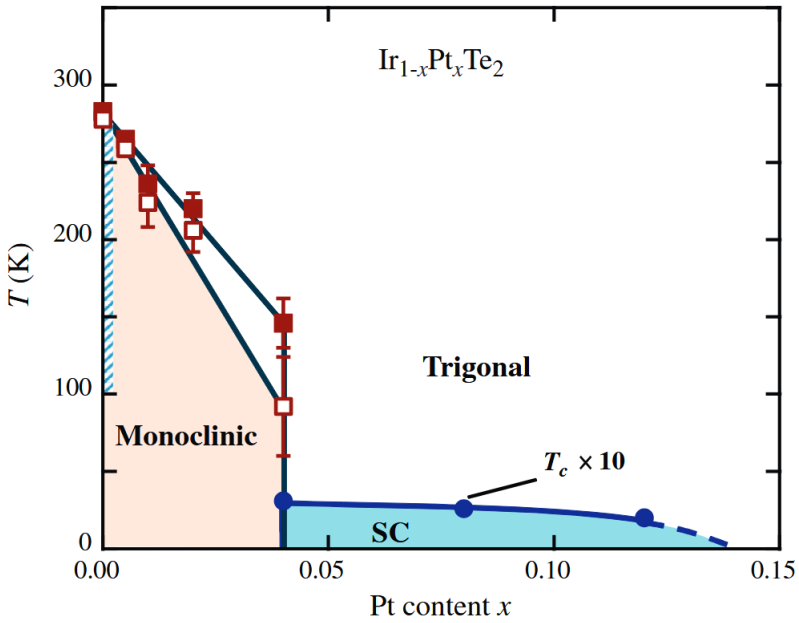


**Figure 6.7.** Phase diagram of $Ir_{1-x}Pt_xTe_2$. Closed and open squares represent $T_s$ upon heating and cooling, respectively. Closed circles represent the $T_c$ for the bulk superconducting phase SC. The hatched area indicates the temperature range in which the resistivity of $Ir_{1-x}Pt_xTe_2$ has a broad hysteretic character. Adapted from Pyon *et al.* [191].

The aim of the study described in the remainder of this subsection was to acquire electronic transport data of $IrTe_2$ uniaxially strained along the $a$ axis. Taking into account the findings of Nicholson *et al.* and Pyon *et al.* [167, 190], we hoped to see a shift in $T_s$ with strain. Uniaxial tension could increase the $T_s$ to the point where the material is in the $6 \times 1$ phase at room temperature and the transition is no longer measured. Uniaxial compression could decrease the $T_s$ sufficiently in order to completely prevent the structural phase transition from happening. Consequently, the superconducting phase would possibly be stabilized at a temperature $T > 1.8$ K, measurable in the PPMS.

### 6.3.2 Results

$IrTe_2$ single crystals were grown by Yingkai Huang at the Van der Waals-Zeeman Institute using the self-flux technique described in Ref. [183]. Laue diffraction was performed to identify the $a$ axis, see Fig. 6.8. The largest samples that were able to be obtained through sparkcutting had a length of 0.8 mm ($w = 0.4$ mm, $t = 0.1$ mm), leading to them not fitting in the strain cells in the conventional manner. The bowtie method on the CS100 was used instead, see Fig. 6.9.

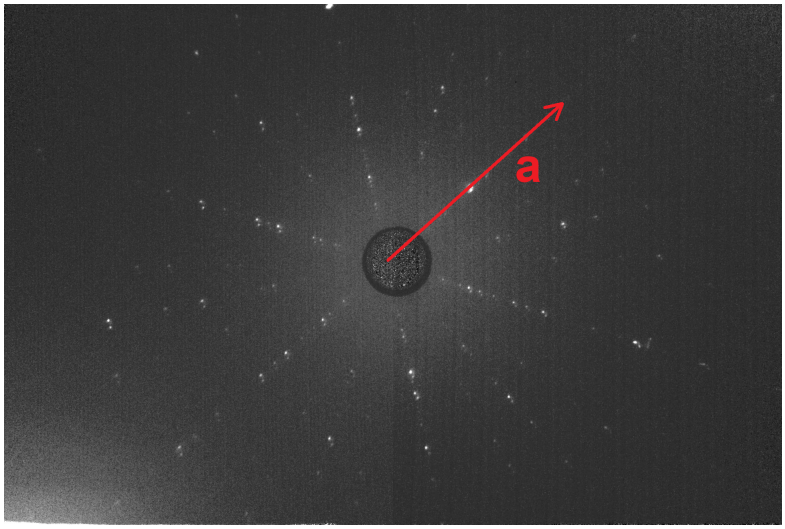


**Figure 6.8.** Laue backscattering diffraction image of an $IrTe_2$ single crystal showing the trigonal structure and used for sample orientation. The red arrow indicates the $a$ axis of the crystal. The direction of the $c$ axis is normal to the image.

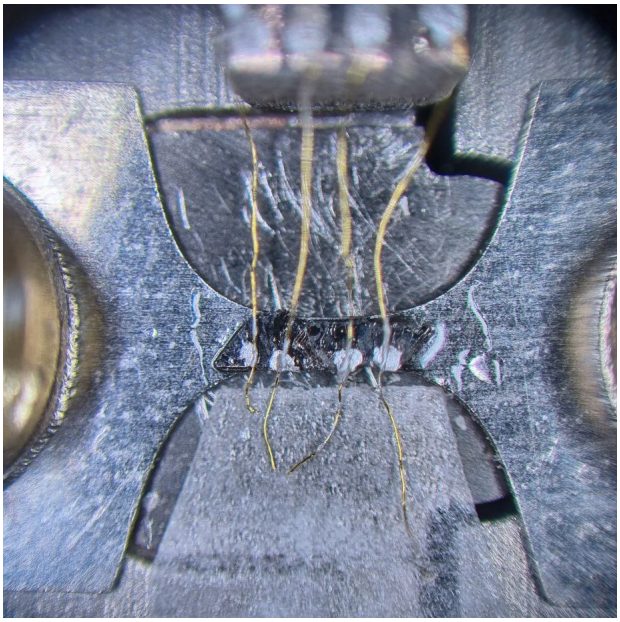

**Figure 6.9.** $IrTe_2$ sample mounted on the CS100 strain cell using the bowtie method. The length of the sample is 0.8 mm.

Fig. 6.10 shows the $R(T)$ curve of $IrTe_2$. The legend displays the top-to-bottom chronological order in which the measurement runs were performed. The structural phase transition is clearly visible at $T_s = 272$ K, manifesting as a sharp increase in sample resistance. The expected hysteretic behavior of the phase transition (see Ref. [183, 190, 191]) is observed as the return to the standard $1 \times 1$ room temperature phase takes place at $T = 287$ K. No superconducting transition and no significant change in $T_s$ with uniaxial strain along the $a$ axis are observed. The strain values are lower than usual due to the use of the bowtie method, but Nicholson *et al.* describe encountering non-elastic deformation at uniaxial tension values larger than 0.2 % [167]. Additionally, the strain values are larger than those reported in Nicholson *et al.*, so the absence of a shift in $T_s$ cannot be attributed to insufficient strain. Strain measurements were performed in the same manner on two other samples, but these are omitted due to the messy and inconclusive nature of their obtained data. Future experiments that aim to measure the transport properties of $IrTe_2$ under uniaxial strain should preferrably be carried out on samples

that are long enough for the conventional mounting method in order to further corroborate the data obtained in this work. Attempts by the group of Anna Isaeva of TU Dresden to grow sufficiently long crystals unfortunately did not lead to a successful outcome (private communication).

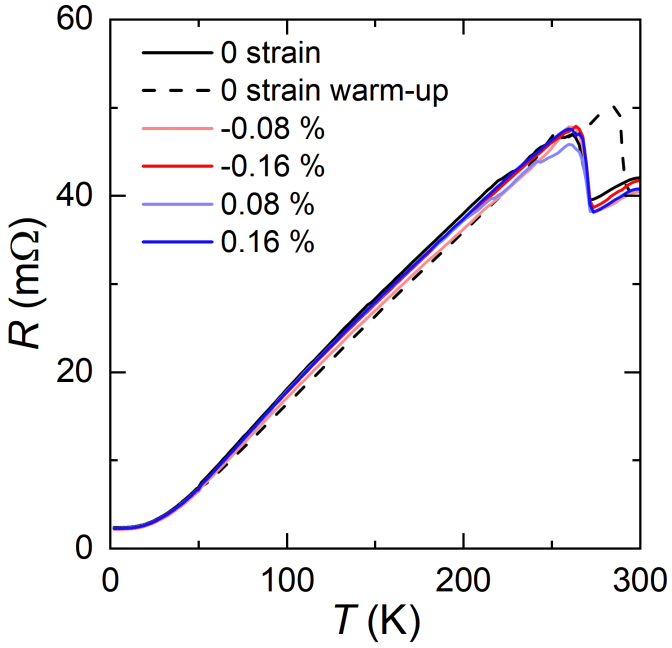


**Figure 6.10.** $R(T)$ curves of an $IrTe_2$ single crystal sample showing the structural transition $T_s$ at about 272 K on cool-down and 287 K on warm-up. All solid curves are cool-down $T$ sweeps, while the dashed curve is a warm-up $T$ sweep. The uniaxial strain is applied along the $a$ axis, parallel to the current direction. Compression is shown in red, tension is shown in blue. The solid black curve is the cool-down zero strain measurement, the dashed black curve is the warm-up measurement that directly followed.

## 6.4 $ZrTe_3$

### 6.4.1 Background

$ZrTe_3$ is a transition metal trichalcogenide (TMT) and has a quasi-2D crystal structure with quasi-1D trigonal prismatic $ZrTe_3$ chains with inversion symmetry along the $b$ axis, see Fig. 6.11. Contrary to $NbSe_2$, the charge density wave (CDW) order originates from a Peierls-type distortion as a result of the quasi-1D electronic structure. The in-plane anisotropic resistance of $ZrTe_3$ is made apparent by a bump at around $T = 60$ K when the current direction is along the $a$ axis. Similar to $NbSe_2$, this bump is attributed to the CDW phase transition and happens at $T_{cdw}$. When current is applied along the $b$ axis, the bump is absent. This is believed to be because electron transport along the $a$ axis is dominated by the same part of the Fermi surface (FS) that is responsible for CDW order [193]. Bulk superconductivity is observed below $T_c = 2$ K and is, like in $NbSe_2$, thought to be competing with the charge-ordered phase [193, 194]. Experimentally, it has been shown that bulk superconductivity in $ZrTe_3$ can be tuned by suppressing CDWs through hydrostatic pressure, intercalation and disorder [195–197].

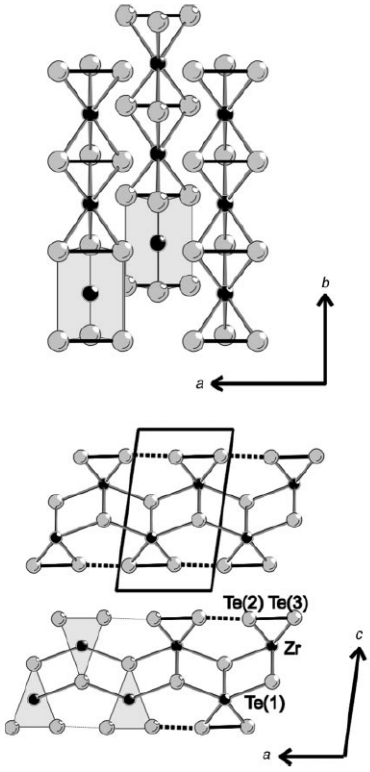


**Figure 6.11.** Crystal structure of $ZrTe_3$. Displayed are the view of the structure along the $c$ axis presenting the trigonal prism chains and the view along the $b$ axis that emphasizes the layered structure of $ZrTe_3$. Figure adapted from Ref. [193]

According to Felser *et al.*, changes in the distance between the intraprism Te(2)–Te(3) atoms play a major role in the shaping of the part of the FS relevant for CDW formation [193, 198]. This has been corroborated by angle-resolved photoemission spectroscopy (ARPES) data [199]. Uniaxial compression along the $a$ axis would make the CDW sections of the FS vanish by strongly changing the band structure, thereby getting rid of charge order. Calculations performed by Felser *et al.* predict large alterations in the band structure with a change of about 3 % in Te(2)–Te(3) intra- and interprism distances [193], though smaller changes should have measurable effects as well.

### 6.4.2 Results

$ZrTe_3$ single crystals were purchased from HQ Graphene through their website [164]. The crystals have a plate-like shape of about 5 mm in size with a metallic appearance as shown in Fig. 6.12(a). Small lines are visible on the surface of the crystals, these are parallel to the $b$ axis. To corroborate this, Laue diffraction was performed, see Fig. 6.12(b). Samples were then cleaved and cut from the crystals with a sharp blade. Typical sample dimensions were $1.5 \times 0.5 \times 0.1$ mm$^3$ ($l \times w \times t$). Fig. 6.12(c) shows a mounted sample cut with the long edge along $a$ and displays the aforementioned lines along $b$. A notable detail of $ZrTe_3$ is that it oxidizes quite rapidly, increasing resistance by several orders of magnitude within a few hours if left exposed to air. This complicated the sample mounting procedure and was remedied by using constant gaseous nitrogen flow during the handling of the samples.

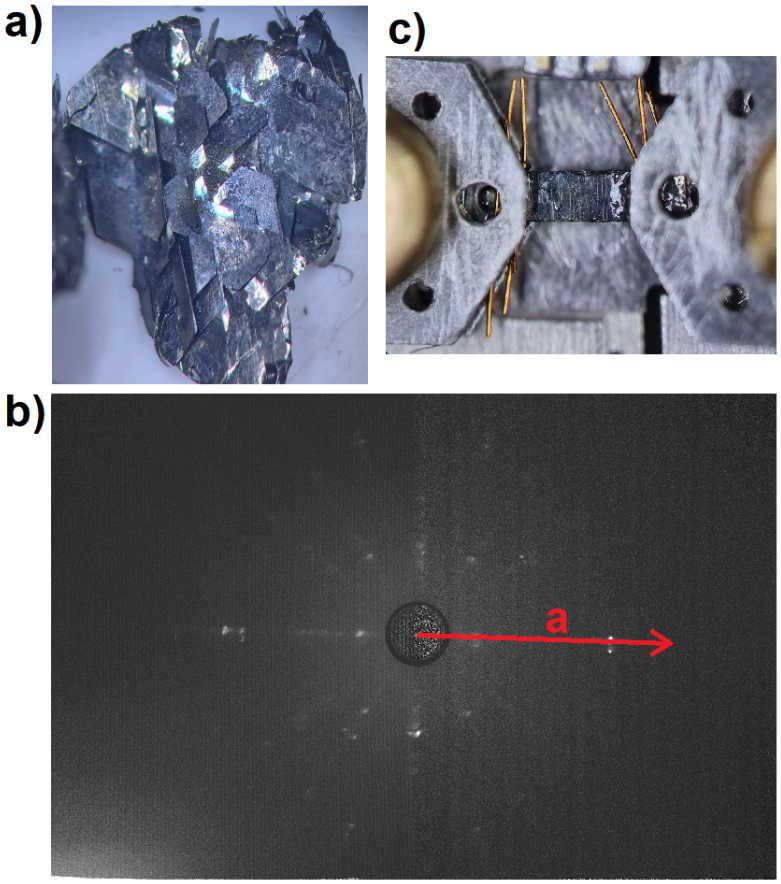


**Figure 6.12.** (a) $ZrTe_3$ single crystals purchased from HQ Graphene. (b) Laue backscattering diffraction image of a $ZrTe_3$ single crystal used for sample orientation. The red arrow indicates the $a$ axis of the crystal. The direction of the $c$ axis is normal to the image. (c) $ZrTe_3$ sample mounted on the CS120 strain cell using the conventional method.

Before performing strain measurements, the in-plane resistance anisotropy was studied using samples cut with the long edge along $a$ and $b$. In each case, the current was parallel to the long edge and the $c$ axis was normal to the face of the crystal. Fig. 6.13 shows the $R(T)$ curves of $ZrTe_3$ measured with the current along the $a$ and the $b$ axis. As expected, the CDW bump is only visible when the current runs

along the $a$ axis. The cool-down measurements were performed in the range of 300 to 2 K, at which point the superconducting phase emerges.

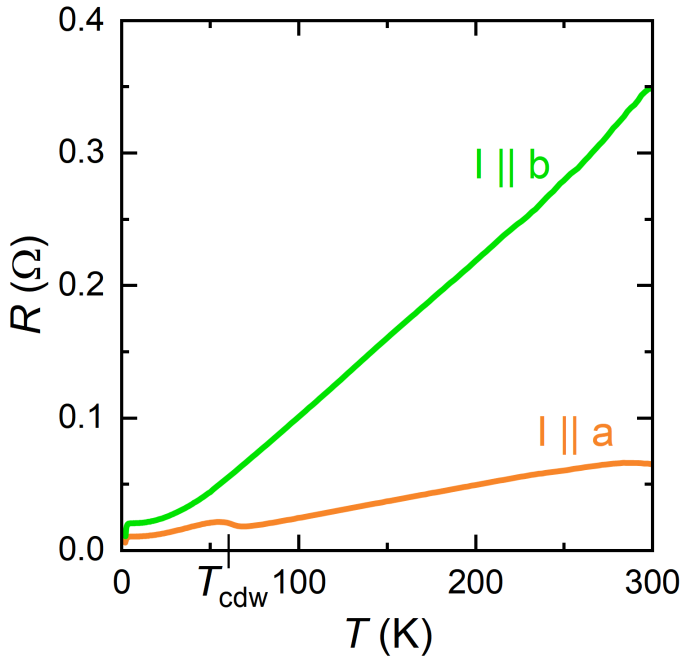


**Figure 6.13.** $R(T)$ diagram of $ZrTe_3$ single crystals samples measured with the current along the $a$ axis (in orange) and $b$ axis (in green). Superconductivity emerges at $T_c = 2$ K for both samples, while the CDW bump is only observed for $I \parallel a$, at $T_{cdw} = 58$ K.

Uniaxial strain measurements were performed on $ZrTe_3$ samples in the CS120 cell. The current and the strain were applied along the $a$ axis, parallel to the long edge of the samples. Fig. 6.14 shows the $R(T)$ curves of one of the samples in the range of 0 to 80 K, with compressive strain in red and tensile strain in blue. The $T_c$ is clearly visible and the resistance in each measurement reached 0 at almost exactly 2 K, no change with uniaxial strain was observed. The CDW bump is again prominent, at $T_{cdw} = 58$ K. To better examine the presence of a shift in $T_{cdw}$ with strain, the first derivative of the data was taken of which the result is displayed in the inset of the figure. No significant shift in $T_{cdw}$ with strain is observed. There does appear to be an increase in resistance of the sample over time as different amounts of

strain are applied. The first big jump is between the uniaxial compression measurements of $-0.28\,\%$ and $-0.42\,\%$. The final zero strain measurement (black dashed line) also does not fall directly on top of the first zero strain measurement (black solid line) and instead follows the trend of increased resistance with measurement run. This implies non-elastic deformation has taken place and makes the measurement slightly less reliable, though the characteristics of $ZrTe_3$ are still evident. The reason for the occurrence of the deformation could be the fact that the CS120 was used instead of the CS100, making higher strain amounts possible and increasing the chance of leaving the elastic regime of the material. The reason for the inclusion of the data of this particular sample is that it provided the clearest and most reliable resistance data.

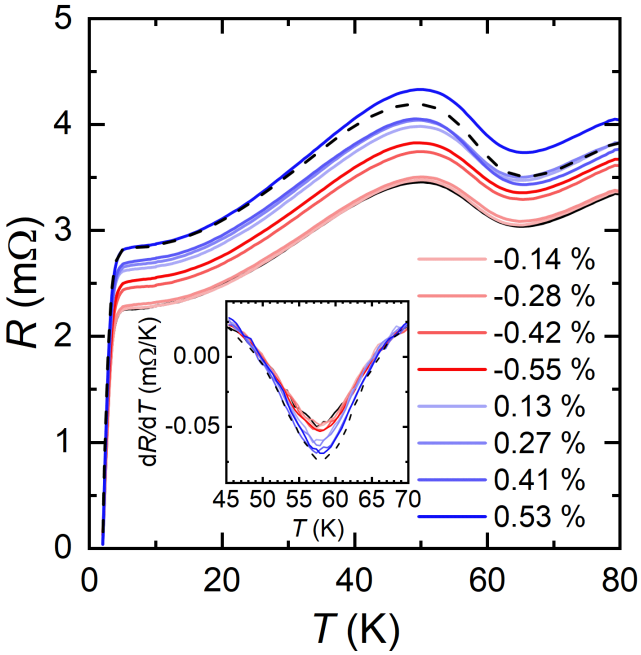


**Figure 6.14.** $R(T)$ curves of a $ZrTe_3$ single crystal sample showing $T_{cdw}$ at 58 K and $T_c$ at 2 K. The uniaxial strain is applied along the $a$ axis, parallel to the current direction. Compression is shown in red, tension is shown in blue. The solid black curve is the first zero strain measurement, while the dashed black curve is measured last. The inset shows the first derivative of the $R(T)$ data, offering a more precise look at $T_{cdw}$.

It is a possibility that the amount of strain applied to the $ZrTe_3$ samples in this study is not large enough to sufficiently change the band structure of the material in a way that it would alter the measured resistance data. However, achieving these larger strains without non-elastically deforming the sample may prove challenging, as the samples in this study already show signs of the deformation at relatively low strain levels.

## 6.5 ZrSiTe

### 6.5.1 Background

ZrSiTe, like its related compounds ZrSiS and ZrSiSe, adopts a layered tetragonal crystal structure with space group $P4/nmm$. All three compounds are semimetals that host topological nodal-line fermions [65, 72, 200]. The S, Se and Te chalcogen ions differ in size, increasing with atomic number. The size difference affects the compounds in two important ways. Firstly, the $c/a$ ratio of lattice parameters is increased by 1.6 % and 13.2 % for ZrSiSe and ZrSiTe, respectively, as compared to ZrSiS [201], resulting in structural dimensionality evolution from a 3D-like to a 2D-like crystal structure [200–202]. Secondly, increasing the chalcogen ion size leads to an increase in spin-orbit coupling (SOC) strength, thereby altering the band structure of the compound [203].

Experimental research performed on ZrSiTe has provided evidence of the aforementioned effects. De Haas-van Alphen (dHvA) oscillations were not observed when the magnetic field was oriented along the $ab$ plane, but were prominent with the field oriented along the $c$ axis due to the 2D-like nature of the material [200]. Angle-resolved photoemission spectroscopy (ARPES) data obtained by Hosen *et al.* demonstrates the addition of a small hole pocket in ZrSiTe not present in ZrSiS or ZrSiSe, implying the strong SOC introduced by the heavier Te ions significantly altered the band structure [203].

Another important difference between ZrSiTe and the other two compounds is the magnitude of the magnetoresistance (MR). ZrSiS displays an extremely large MR in the order of $10^5$ % at 9 T, whereas ZrSiSe reaches $10^4$ % at around 9 T [9, 75, 203]. ZrSiTe on the other hand exhibits ordinary magnetotransport. This is believed to be due to the absence of near-perfect electron-hole compensation in ZrSiTe, meaning only one type of carrier dominates the electrical conductivity of the system [203].

With the magneto-elastoresistance (MER) and Shubnikov-de Haas (SdH) oscillations of ZrSiS and ZrSiSe thoroughly explored [9, 204], we aimed to study the MR of ZrSiTe under uniaxial strain to get a better understanding of the effect of strain on the MER and SdH oscillations of ZrSiTe.

### 6.5.2 Results

A singular ZrSiTe sample was gifted to us by the group of Steffen Wiedmann at Radboud Universiteit Nijmegen. The crystal was grown by the Schoop Lab of Princeton University. Its dimensions were sufficient for uniaxial strain measurements using the conventional mounting method for the CS100 strain cell. Laue diffraction was performed, but the results were not sufficiently clear to accurately orient the sample. However, the small sample dimensions forced a specific sample orientation in the strain cell, and Linnartz *et al*. found that – in the case of ZrSiSe – uniaxial strain affected the MER of the samples in both the [100] and [110] strain directions [9]. Therefore, we oriented our sample along an unknown principal axis ([100] or [110]), with the $c$ axis ([001]) certainly directed perpendicular to the face of the crystal. The sample surface was oxidized so the top layers were cleaved off to provide proper contact for the gold wires. The mounting procedure was then performed with the use of constant gaseous nitrogen flow to prevent oxidation.

Fig. 6.15 shows the $R(B)$ curves of the uniaxially strained ZrSiTe sample. The magnetic field was parallel to the $c$ axis, while the current direction was parallel to the strain direction. Compression is shown in red, tension is shown in blue. No large MR is observed as expected. MER and SdH oscilations are also absent. The lack of MER implies no change in transport mobility with strain similar to ZrSiS, but contrary to ZrSiSe [9, 204].

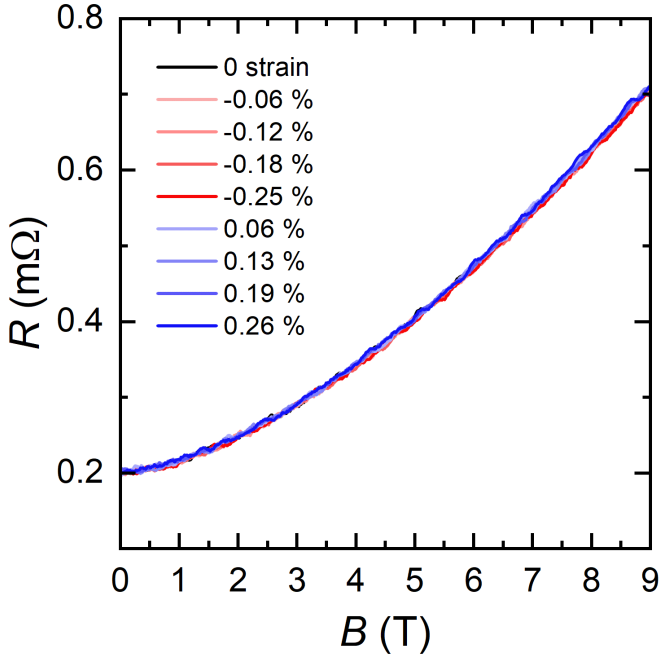


**Figure 6.15.** $R(B)$ curves of the ZrSiTe single crystal sample under uniaxial strain along an unknown principle axis ([100] or [110]). Compression is shown in red, tension is shown in blue.

Since dHvA oscillations have been observed experimentally in ZrSiTe before at magnetic fields of about 5 T [200], it was somewhat expected that our ZrSiTe sample would exhibit SdH oscillations as well. However, the dHvA oscillations were quite weak, and the amount of defects in our sample is assumed to be large due to its relatively small residual resistance ratio of 7.7 and the Laue diffraction results. Accordingly, the absence of SdH oscillations in our sample is not entirely surprising. Future MR studies on ZrSiTe should focus on using high quality crystals with a well defined sample orientation.

## 6.6 $LaO_{0.8}F_{0.2}BiSSe$

### 6.6.1 Background

$LaO_{0.8}F_{0.2}BiSSe$ has already been described extensively in chapter 4, so this subsection will focus on the anisotropic behavior of the material in the $ab$ plane. Being sufficiently F-doped, the structural phase transition of LaOBiSSe from tetragonal to monoclinic is fully suppressed [205]. Although $LaO_{0.8}F_{0.2}BiSSe$ possesses a tetragonal four-fold structural symmetry, two-fold symmetric in-plane anisotropy was observed in its superconducting states [206, 207]. This is an indicator of nematic superconductivity, in which the superconducting gap amplitude breaks the rotational symmetry of the crystal. Nematic superconductivity has been reported in the topological superconductor $Sr_xBi_2Se_3$ [165, 208, 209]. In that material, uniaxial strain was used experimentally to suppress certain superconducting domains with different nematic orientations, essentially demonstrating superconducting-domain engineering [210]. Similar to studies of $Sr_xBi_2Se_3$, we aimed to explore the effect of uniaxial strain on the nematic superconductivity of $LaO_{0.8}F_{0.2}BiSSe$.

### 6.6.2 Results

$LaO_{0.8}F_{0.2}BiSSe$ crystals were taken from the same batch as the one used for the study described in chapter 4. The size of the crystals was slightly too small for the conventional mounting method, so the bowtie method was used. Laue diffraction was performed to determine the $a$ axis, see Fig. 6.16. Samples were then cleaved and cut from the crystals with a sharp blade. Typical sample dimensions were $1.0 \times 0.5 \times 0.05\,\mathrm{mm}^3$ ($l \times w \times t$).

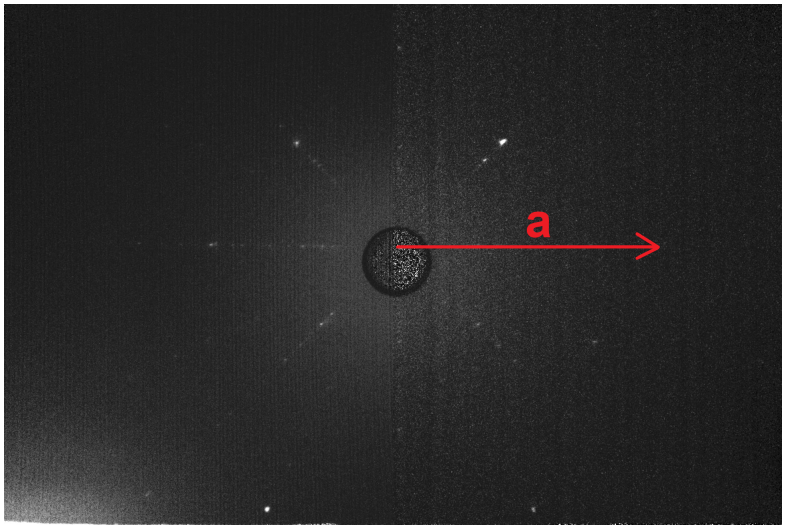


**Figure 6.16.** Laue backscattering diffraction image of a $LaO_{0.8}F_{0.2}BiSSe$ crystal used for sample orientation. The red arrow indicates the $a$ axis of the crystal. The direction of the $c$ axis is normal to the image.

Uniaxial strain measurements were performed on the $LaO_{0.8}F_{0.2}BiSSe$ samples in the CS120 cell. The current and the strain were applied along the $a$ axis, parallel to the long edge of the samples. Fig. 6.17 shows the $R(T)$ curves of one of the samples in the range of 3 to 4 K and $B = 0$, with compressive strain in red and tensile strain in blue. Taking the superconducting transition temperature as the point where the resistance of the sample reaches 50 % of the normal resistance gives $T_c \approx 3.4$ K. The $T_c$ shows a small systematic decrease with both compressive and tensile strain: $-0.19$ % compression leads to a $-0.43$ % decrease, while $0.18$ % tension leads to a $-0.60$ % decrease. The zero strain return measurement taken at the end of the measurement cycle closely reproduces the first zero strain measurement, only deviating from the original $T_c$ by $-0.09$ %. Our findings are in line with those published by Kostylev *et al.* on the nematic superconductor $Sr_xBi_2Se_3$ [210], where a 0.5 % change in $T_c$ with 1.0 % uniaxial strain is observed. This is attributed to a change in density of states of the crystal.

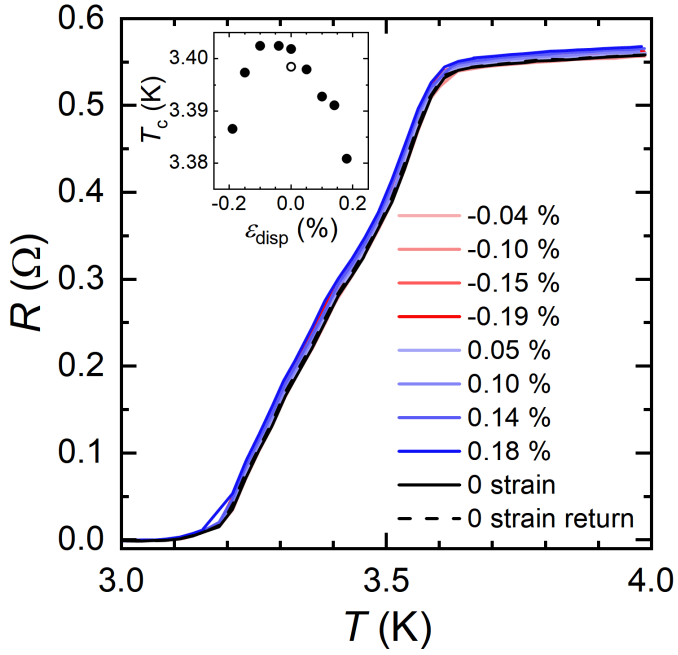


**Figure 6.17.** $R(T)$ curves of a $LaO_{0.8}F_{0.2}BiSSe$ single crystal sample under uniaxial strain along the $a$ axis and $B = 0$. Compression is shown in red, tension is shown in blue. The solid black curve is the first zero strain measurement, while the dashed black curve is measured last. The inset shows the strain dependence of $T_c$.

Fig. 6.18 shows the $R(B)$ curves of the same sample in the range of 0 to 9 T at $T = 3$ K. Like the $T_c$, the upper critical field $B_{c2}$ of the crystal decreases with uniaxial strain. Taking $B_{c2}$ as the point where the resistance of the sample reaches 50 % of the normal resistance gives $B_{c2} \approx 1.45$ T at zero strain. Under $-0.18$ % compression the $B_{c2}$ is decreased by $-6.8$ %, while under 0.19 % tension the decrease is $-11.0$ %. The zero strain return measurement does not lie exactly on the first zero strain curve, but differs by $-5.0$ %. The work of Kostylev *et al.* demonstrates a change in $B_{c2}$ of $Sr_xBi_2Se_3$ of between 0 and 30 %, depending on uniaxial strain direction with strains of up to 1.2 % [210]. This directional dependence is used as evidence for in-situ uniaxial-strain control of nematic superconductivity in $Sr_xBi_2Se_3$.

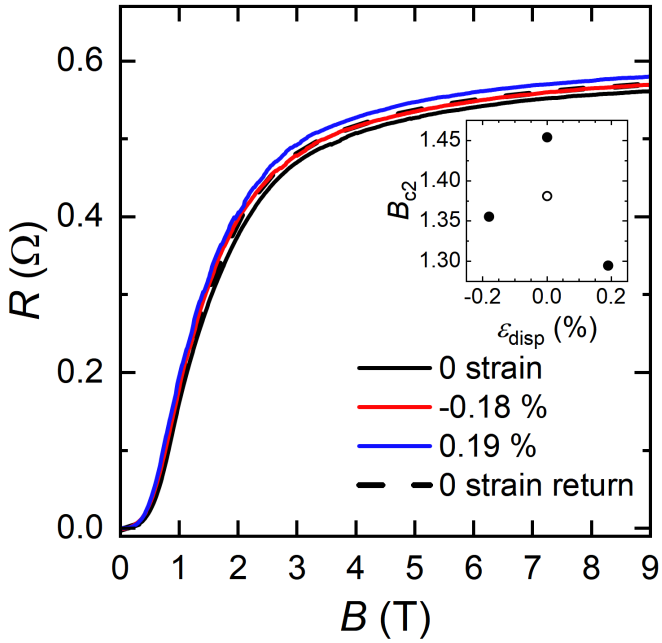


**Figure 6.18.** $R(B)$ curves of a $LaO_{0.8}F_{0.2}BiSSe$ single crystal sample under uniaxial strain along the $a$ axis at $T = 3$ K. Compression is shown in red, tension is shown in blue. The solid black curve is the first zero strain measurement, while the dashed black curve is measured last. The inset shows the strain dependence of $B_{c2}$.

Our study on $LaO_{0.8}F_{0.2}BiSSe$ finds changes in $T_c$ and $B_{c2}$ of similar magnitude as those obtained by Kostylev *et al.* on $Sr_xBi_2Se_3$ [210], but at lower strain amounts. A substantial decrease in $B_{c2}$ is observed when uniaxial stress is applied along the $a$ axis, reaffirming the potential of the bowtie mounting method. For these reasons, future research should perform uniaxially strained $B_{c2}$ measurements along different axes. This could shine light on strain-tunability of nematic superconductors with a tetragonal crystal structure, analogous to trigonal nematic superconductors such as $Sr_xBi_2Se_3$. Addtionally, larger crystal size would allow for the use of the conventional mounting method and with it larger strain values.

## 6.7 Highly oriented pyrolitic graphite

### 6.7.1 Background

Graphite is a layered crystal composed of stacked sheets of graphene, each formed by carbon atoms arranged in a hexagonal unit cell. Similar to graphene, it is known to host topologically non-trivial Dirac fermions [211, 212]. Other remarkable properties of graphite that have been observed experimentally are the quantum Hall effect (QHE), ferromagnetism, and magnetic-field-driven metal-insulator transitions [213–215]. With graphene and its multitude of forms such as carbon nanotubes receiving the amount of attention they have the past few decades, having a full understanding of the magnetic and electric properties of graphite can be advantageous. In this explorative study we performed in-plane uniaxial strain measurements on highly oriented pyrolitic graphite (HOPG) crystals to examine their strain response. HOPG is the highest-quality synthetic form of graphite available. It has a low mosaic spread angle, implying close alignment between each individual graphite crystallite. High quality HOPG crystals have an in-plane mosaic spread smaller than 1 degree. Typical crystallite diameter ranges from 1 to 10 $\mu$m.

### 6.7.2 Results

A HOPG crystal was purchased from HQ Graphene through their website [164]. Laue diffraction did not yield a clear picture of the orientation of the crystal. This is somewhat expected, since even though the crystallites are highly oriented, they are still small and misaligned. Determining the hexagonal out-of-plane axis was trivial, as the crystals are strongly layered. Samples were cleaved and cut from the crystal with a sharp blade. Typical sample dimensions were $1.5\times0.5\times0.1\,\mathrm{mm}^3$ ($l\times w\times t$).

A sample was mounted in the CS100 strain cell using the conventional mounting method. Uniaxial strain measurements were then performed with the current and strain applied along the in-plane direction. Fig. 6.19(a) shows the $R(B)$ curves of the sample in the range of 0 to 9 T, with compressive strain in red and tensile strain in blue. Shubnikov-de Haas (SdH) oscillations are prominently visible from 0.5 T onward. Fig. 6.19(b) shows the corresponding fast Fourier transform (FFT) diagram of the curves in (a) after taking the first derivative of the data in order to remove the background magnetoresistance. The peak frequencies align well with those in the literature, with the characteristic peak of the topologically

trivial electron-type carriers at 4.7 T and its harmonics at 9.4 and 14.5 T [213, 216, 217]. The clarity of the frequency peaks reaffirms the high quality of the crystal; the SdH peak structure appears even more clear than previously observed in the literature. Like in similar SdH oscillation studies, the characteristic peak belonging to the topologically non-trivial Dirac hole-type carriers is not observed. This peak has been detected in de Haas-van Alphen (dHvA) studies, though, at a frequency of 6.41 T [213, 216, 217].

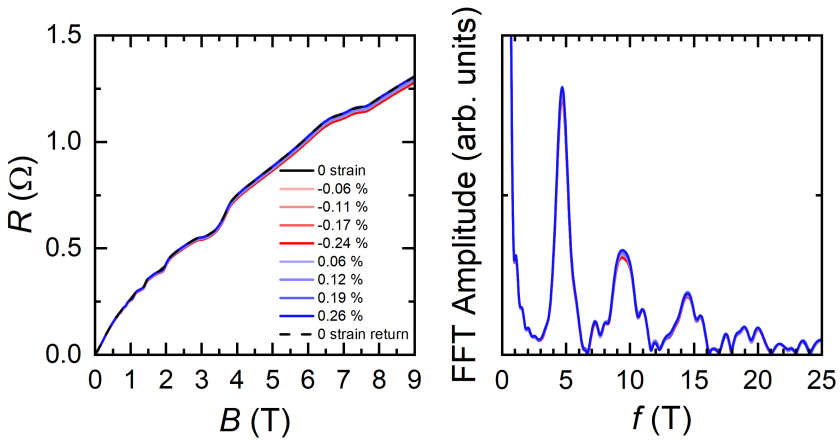


**Figure 6.19.** (a) $R(B)$ curves of a HOPG sample under uniaxial strain along the $a$ axis. Compression is shown in red, tension is shown in blue. The solid black curve is the first zero strain measurement, while the dashed black curve is measured last. (b) FFT diagram of the SdH oscillations shown in (a). The characteristic peak belonging to topologically trivial electron carriers is found at 4.7 T. Its harmonics are found at 9.4 T and 14.5 T.

The only systematic change in our measurement data appears to be a slight increase in FFT amplitude of the electron peak and its harmonics under uniaxial tension. A possible interpretation of this can be an increase in quantum mobility with tensile strain. Biaxial tensile strains have been shown to increase carrier mobility in Si metal-oxide-semiconductors by decreasing macroscopic interface roughness [218]. Though the strain in our study is uniaxial, it is plausible that tension enhances electronic transport in the sample by better aligning crystallites. This would lower structural disorder and enhance quantum oscillatory phenomena such as SdH and

dHvA oscillations. Future uniaxial strain studies on HOPG could aim to measure the dHvA effect and apply strains of a larger magnitude.

## 6.8 Conclusion and outlook

In this chapter, we present additional materials that were uniaxially strained and studied for their various intriguing physical properties. The largely insignificant strain effects as a result generally suggest that applying a larger amount of uniaxial stress to the crystal samples could instead provide more compelling results. However, it must be noted that excessive amounts of uniaxial strain could lead to non-elastic deformation, fundamentally and irreversibly damaging the material by adding imperfections and defects to the crystal structure. Taking this into account, future strain studies should aim to apply larger strains and push each material to its elastic limit in order to fully examine the material properties. The fact that the credible theoretical hypotheses described in this chapter cannot be corroborated experimentally by carefully performed studies highlights the challenging nature of uniaxial strain research.

# Bibliography


1. C. Kittel, P. McEuen, J. Wiley, and Sons. Introduction to Solid State Physics. John Wiley & Sons, 2019.
2. R. Cava, N. de Leon, and W. Xie. "Introduction: Quantum Materials". Chem. Rev. 121, 2021, pp. 2777–2779.
3. N. P. Armitage, E. J. Mele, and A. Vishwanath. "Weyl and Dirac semimetals in three-dimensional solids". Rev. Mod. Phys. 90, 2018, p. 015001.
4. N. A. Red'Ko and N. A. Rodionov. "Topological phase transitions in $Bi_{1-x}Sb_x$ alloys and composition dependence of the position of the heavy-hole band". JETP Lett. 42, 1985, p. 246.
5. M. Koshino and I. F. Hizbullah. "Magnetic susceptibility in three-dimensional nodal semimetals". Phys. Rev. B 93, 2016, p. 045201.
6. J. Hu, Z. Tang, J. Liu, X. Liu, Y. Zhu, D. Graf, K. Myhro, S. Tran, C. N. Lau, J. Wei, and Z. Mao. "Evidence of Topological Nodal-Line Fermions in ZrSiSe and ZrSiTe". Phys. Rev. Lett. 117, 2016, p. 016602.
7. J. Liu and L. Balents. "Correlation effects and quantum oscillations in topological nodal-loop semimetals". Phys. Rev. B 95, 2017, p. 075426.
8. B. Roy. "Interacting nodal-line semimetal: Proximity effect and spontaneous symmetry breaking". Phys. Rev. B 96, 2017, p. 041113.
9. J. F. Linnartz, A. Kool, J. P. Lorenz, C. S. A. Müller, M. R. van Delft, R. Singha, L. M. Schoop, N. E. Hussey, A. de Visser, and S. Wiedmann. "Unraveling magneto-elastoresistance in the Dirac nodal-line semi-metal ZrSiSe". npj Q. Mat. 9, 2024, p. 63.
10. M. Tinkham. Introduction to Superconductivity. 2nd edn. Dover, 2004.
11. J. F. Annett. Superconductivity, Superfluids and Condensates. Oxford University Press, 2004.

12. T. Hattori, Y. Ihara, Y. Nakai, K. Ishida, Y. Tada, S. Fujimoto, N. Kawakami, E. Osaki, K. Deguchi, N. K. Sato, and I. Satoh. "Superconductivity Induced by Longitudinal Ferromagnetic Fluctuations in UCoGe". Phys. Rev. Lett. 108, 2012, p. 066403.

13. W.-M. Huang and H.-H. Lin. "Pairing mechanism in multiband superconductors". Sci. Rep. 10, 2020, p. 7439.

14. F. Flicker and J. van Wezel. "Charge order from orbital-dependent coupling evidenced by $NbSe_2$". Nat. Comm. 6, 2015, p. 7034.

15. W. Shi, B. J. Wieder, H. L. Meyerheim, Y. Sun, Y. Zhang, Y. Li, L. Shen, Y. Qi, L. Yang, J. Jena, P. Werner, K. Koepernik, S. Parkin, Y. Chen, C. Felser, B. A. Bernevig, and Z. Wang. "A charge-density-wave topological semimetal". Nat. Phys. 17, 2021, pp. 381–387.

16. M. Litskevich, M. S. Hossain, S.-B. Zhang, Z.-J. Cheng, S. N. Guin, N. Kumar, C. Shekhar, Z. Wang, Y. Li, G. Chang, J.-X. Yin, Q. Zhang, G. Cheng, T. A. Cochran, N. Shumiya, Y.-X. Jiang, X. P. Yang, D. Multer, X. Liu, N. Yao, Y. Yao, C. Felser, T. Neupert, and M. Z. Hasan. "Boundary modes of a charge density wave state in a topological material". Nat. Phys. 20, 2024, pp. 1253–1261.

17. A. M. Gabovich and A. I. Voitenko. "Superconductors with charge- and spin-density waves: theory and experiment (Review)". Low Temperature Physics 26, 2000, pp. 305–330.

18. A. Gabovich, A. Voitenko, and M. Ausloos. "Charge- and spin-density waves in existing superconductors: competition between Cooper pairing and Peierls or excitonic instabilities". Phys. Rep. 367, 2002, pp. 583–709.

19. J. Chang, E. Blackburn, A. T. Holmes, N. B. Christensen, J. Larsen, J. Mesot, R. Liang, D. A. Bonn, W. N. Hardy, A. Watenphul, M. v. Zimmermann, E. M. Forgan, and S. M. Hayden. "Direct observation of competition between superconductivity and charge density wave order in $YBa_2Cu_3O_{6.67}$". Nat. Phys. 8, 2012, pp. 871–876.

20. Y. Liu, D. F. Shao, L. J. Li, W. J. Lu, X. D. Zhu, P. Tong, R. C. Xiao, L. S. Ling, C. Y. Xi, L. Pi, H. F. Tian, H. X. Yang, J. Q. Li, W. H. Song, X. B. Zhu, and Y. P. Sun. "Nature of charge density waves and superconductivity in $1T$–$TaSe_{2-x}Te_x$". Phys. Rev. B 94, 2016, p. 045131.

21. K. Cho, M. Ko'nczykowski, S. Teknowijoyo, M. A. Tanatar, J. Guss, P. B. Gartin, J. M. Wilde, A. Kreyssig, R. J. McQueeney, A. I. Goldman, P. J. Mishra V. Hirschfeld, and R. Prozorov. "Using controlled disorder to probe the interplay between charge order and superconductivity in $NbSe_2$". Nat. Comm. 9, 2018, p. 2796.

22. M. Leroux, V. Mishra, C. Opagiste, P. Rodière, A. Kayani, W.-K. Kwok, and U. Welp. "Charge density wave and superconductivity competition in $Lu_5Ir_4Si_{10}$: A proton irradiation study". Phys. Rev. B 102, 2020, p. 094519.

23. Y. Feng, J. Wang, R. Jaramillo, J. van Wezel, S. Haravifard, G. Srajer, Y. Liu, Z.-A. Xu, P. B. Littlewood, and T. F. Rosenbaum. "Order parameter fluctuations at a buried quantum critical point". PNAS 109, 2012, pp. 7224–7229.

24. M. Leroux, I. Errea, M. Le Tacon, S.-M. Souliou, G. Garbarino, L. Cario, A. Bosak, F. Mauri, M. Calandra, and P. Rodière. "Strong anharmonicity induces quantum melting of charge density wave in $2H$–$NbSe_2$ under pressure". Phys. Rev. B 92, 2015, p. 140303.

25. I. H. Shames and F. A. Cozzarelli. Elastic and inelastic stress analysis. 1st edn. CRC Press, 1997.

26. B. J. Goodno and J. M. Gere. Mechanics of Materials. Cl-Engineering, 2017.

27. M. E. Barber. "Uniaxial stress technique and investigations into correlated electron systems". Ph.D. thesis. University of St Andrews, 2017.

28. C. W. Hicks, M. E. Barber, S. D. Edkins, D. O. Brodsky, and A. P. Mackenzie. "Piezoelectric-based apparatus for strain tuning". Rev. Sci. Instr. 85, 2014, p. 065003.

29. C. W. Hicks, F. Jerzembeck, H. M. L. Noad, M. E. Barber, and A. P. Mackenzie. "Probing Quantum Materials with Uniaxial Stress". Ann. Rev. Cond. Matt. Phys., 2024.

30. G. Jones and D. J. Dunstan. "Diamond-anvil uniaxial stress cell". Rev. Sci. Instrum. 67, 1996, pp. 489–493.

31. U. Welp, M. Grimsditch, S. Fleshler, W. Nessler, J. Downey, G. W. Crabtree, and J. Guimpel. "Effect of uniaxial stress on the superconducting transition in $YBa_2Cu_3O_7$". Phys. Rev. Lett. 69, 1992, pp. 2130–2133.

32. O. M. Dix, A. G. Swartz, R. J. Zieve, J. Cooley, T. R. Sayles, and M. B. Maple. "Anisotropic Dependence of Superconductivity on Uniaxial Pressure in $CeIrIn_5$". Phys. Rev. Lett. 102, 2009, p. 197001.

33. D. S. Jin, A. Husmann, T. F. Rosenbaum, T. E. Steyer, and K. T. Faber. "Controlled Symmetry Breaking in Superconducting $UPt_3$". Phys. Rev. Lett. 78, 1997, pp. 1775–1778.

34. N. H. van Dijk, P. Rodière, F. Yakhou, M.-T. Fernández-Díaz, B. Fåk, A. Huxley, and J. Flouquet. "Magnetic order of $UPt_3$ under uniaxial pressure". Phys. Rev. B 63, 2001, p. 104426.

35. Y. Kamihara, T. Watanabe, M. Hirano, and H. Hosono. "Iron-based layered superconductor $La[O_{1-x}F_x]FeAs$ ($x = 0.05$-$0.12$) with $T_c$ = 26 K". J. Am. Chem. Soc. 130, 2008, pp. 3296–3297.

36. J.-H. Chu, J. G. Analytis, K. de Greve, P. L. McMahon, Z. Islam, Y. Yamamoto, and I. R. Fisher. "In-Plane Resistivity Anisotropy in an Underdoped Iron Arsenide Superconductor". Science 329, 2010, pp. 824–826.

37. J.-H. Chu, H.-H. Kuo, J. G. Analytis, and I. R. Fisher. "Divergent Nematic Susceptibility in an Iron Arsenide Superconductor". Science 337, 2012, pp. 710–712.

38. M. S. Ikeda, T. Worasaran, J. C. Palmstrom, J. A. W. Straquadine, P. Walmsley, and I. R. Fisher. "Symmetric and antisymmetric strain as continuous tuning parameters for electronic nematic order". Phys. Rev. B 98, 2018, p. 245133.

39. M. E. Barber, A. Steppke, A. P. Mackenzie, and C. W. Hicks. "Piezoelectric-based uniaxial pressure cell with integrated force and displacement sensors". Rev. Sci. Instr. 90, 2019, p. 023904.

40. A. P. Mackenzie and Y. Maeno. "The superconductivity of $Sr_2RuO_4$ and the physics of spin-triplet pairing". Rev. Mod. Phys. 75, 2003, pp. 657–712.

41. Y. Maeno, S. Yonezawa, and A. Ramires. "Still Mystery after All These Years –Unconventional Superconductivity of $Sr_2RuO_4$–". J. Phys. Soc. Jpn. 93, 2024, p. 062001.

42. Y. Maeno, T. Ando, Y. Mori, E. Ohmichi, S. Ikeda, S. NishiZaki, and S. Nakatsuji. "Enhancement of Superconductivity of $Sr_2RuO_4$ to 3 K by Embedded Metallic Microdomains". Phys. Rev. Lett. 81, 1998, pp. 3765–3768.

43. N. H. Jo, E. Gati, and H. Pfau. "Uniaxial stress effect on the electronic structure of quantum materials". Front. Electron. Mater. 4, 2024, p. 1392760.

44. C. W. Hicks, D. O. Brodsky, E. A. Yelland, A. S. Gibbs, J. A. N. Bruin, M. E. Barber, S. D. Edkins, K. Nishimura, S. Yonezawa, Y. Maeno, and A. P. Mackenzie. "Strong Increase of $T_c$ of $Sr_2RuO_4$ Under Both Tensile and Compressive Strain". Science 344, 2014, pp. 283–285.

45. H.-H. Kim, S. M. Souliou, M. E. Barber, E. Lefrançois, M. Minola, M. Tortora, R. Heid, N. Nandi, R. A. Borzi, G. Garbarino, A. Bosak, J. Porras, T. Loew, M. König, P. J. W. Moll, A. P. Mackenzie, B. Keimer, C. W. Hicks, and M. Le Tacon. "Uniaxial pressure control of competing orders in a high-temperature superconductor". Science 362, 2018, pp. 1040–1044.

46. S. Nakata, P. Yang, M. E. Barber, K. Ishida, H.-H. Kim, T. Loew, M. Le Tacon, A. P. Mackenzie, M. Minola, C. W. Hicks, and B. Keimer. "Normal-state charge transport in $YBa_2Cu_3O_{6.67}$ under uniaxial stress". npj Quantum Mater. 7, 2022, p. 118.

47. J. Mutch, W.-C. Chen, P. Went, T. Qian, I. Z. Wilson, A. Andreev, C.-C. Chen, and J.-H. Chu. "Evidence for a strain-tuned topological phase transition in $ZrTe_5$". Sci. Adv. 5, 2019, eaav9771.

48. N. H. Jo, O. A. Ashour, Z. Shu, C. Jozwiak, A. Bostwick, Y. Wang, E. Downey, S. H. Ryu, K. Sun, T. Kong, S. M. Griffin, and E. Rotenberg. "Effects of strain and defects on the topological properties of $HfTe_5$". Phys. Rev. B 109, 2024, p. 235122.

49. N. H. Jo, L.-L. Wang, P. P. Orth, S. L. Bud'ko, and P. C. Canfield. "Magnetoelastoresistance in $WTe_2$: Exploring electronic structure and extremely large magnetoresistance under strain". PNAS 116, 2019, pp. 25524–25529.

50. D. Shoenberg. Magnetic oscillations in metals. Cambridge University Press, 1984.

51. A. Alexandradinata and L. Glazman. "Semiclassical theory of Landau levels and magnetic breakdown in topological metals". Phys. Rev. B 97, 2018, p. 144422.

52. A. Alexandradinata, C. Wang, W. Duan, and L. Glazman. “Revealing the Topology of Fermi-Surface Wave Functions from Magnetic Quantum Oscillations”. Phys. Rev. X 8, 2018, p. 011027.

53. C. S. A. Müller, T. Khouri, M. R. van Delft, S. Pezzini, Y.-T. Hsu, J. Ayres, M. Breitkreiz, L. M. Schoop, A. Carrington, N. E. Hussey, and S. Wiedmann. “Determination of the Fermi surface and field-induced quasiparticle tunneling around the Dirac nodal loop in ZrSiS”. Phys. Rev. Res. 2, 2020, p. 023217.

54. CS1x0 Datasheet. Version 9.7. Razorbill Instruments. 2024.

55. AP001: Thermal expansion. Version 1.2. Razorbill Instruments. 2023.

56. AP005: Mounting samples. Version 4.3. Razorbill Instruments. 2023.

57. URL: https://www.go-araldite.com/en.

58. RP100 power supply manual. Version 6.9. Razorbill Instruments. 2023.

59. N. Takeshita, T. Sasagawa, T. Sugioka, Y. Tokura, and H. Takagi. “Gigantic Anisotropic Uniaxial Pressure Effect on Superconductivity within the $CuO_2$ Plane of $La_{1.64}Eu_{0.2}Sr_{0.16}CuO_4$: Strain Control of Stripe Criticality”. J. Phys. Soc. Jpn. 73, 2004, pp. 1123–1126.

60. M. S. Torikachvili, S. L. Bud’ko, N. Ni, P. C. Canfield, and S. T. Hannahs. “Effect of pressure on transport and magnetotransport properties in $CaFe_2As_2$ single crystals”. Phys. Rev. B 80, 2009, p. 014521.

61. S. D. Johnson, R. J. Zieve, and J. C. Cooley. “Nonlinear effect of uniaxial pressure on superconductivity in $CeCoIn_5$”. Phys. Rev. B 83, 2011, p. 144510.

62. P. Malinowski, Q. Jiang, J. J. Sanchez, J. Mutch, Z. Liu, P. Went, J. Liu, P. J. Ryan, J.-W. Kim, and J.-H. Chu. “Suppression of superconductivity by anisotropic strain near a nematic quantum critical point”. Nat. Phys. 16, 2020, pp. 1189–1193.

63. M. S. da Luz, J. J. Neumeier, R. K. Bollinger, A. S. Sefat, M. A. McGuire, R. Jin, B. C. Sales, and D. Mandrus. “High-resolution measurements of the thermal expansion of superconducting Co-doped $BaFe_2As_2$”. Phys. Rev. B 79, 2009, p. 214505.

64. D. Schiferl and C. S. Barrett. "The crystal structure of arsenic at 4.2, 78 and 299°K". J. Appl. Cryst. 2, 1969, pp. 30–36.

65. L. M. Schoop, M. N. Ali, C. Straßer, A. Topp, A. Varykhalov, D. Marchenko, V. Duppel, S. S. P. Parkin, B. V. Lotsch, and C. R. Ast. "Dirac cone protected by non-symmorphic symmetry and three-dimensional Dirac line node in ZrSiS". Nat. Comm. 7, 2016, p. 11696.

66. J. Park, J. M. Bartlett, H. M. L. Noad, A. L. Stern, M. E. Barber, M. König, S. Hosoi, T. Shibauchi, A. P. Mackenzie, A. Steppke, and C. W. Hicks. "Rigid platform for applying large tunable strains to mechanically delicate samples". Rev. Sci. Instrum. 91, 2020, p. 083902.

67. C. Dhital, Z. Yamani, W. Tian, J. Zeretsky, A. S. Sefat, Z. Wang, R. J. Birgeneau, and S. D. Wilson. "Effect of Uniaxial Strain on the Structural and Magnetic Phase Transitions in $BaFe_2As_2$". Phys. Rev. Lett. 108, 2012, p. 087001.

68. T. Worasaran, M. S. Ikeda, J. C. Palmstrom, J. A. W. Straquadine, S. A. Kivelson, and I. R. Fisher. "Nematic quantum criticality in an Fe-based superconductor revealed by strain-tuning". Science 372, 2021, pp. 973–977.

69. H. Weng, Y. Liang, Q. Xu, R. Yu, Z. Fang, X. Dai, and Y. Kawazoe. "Topological node-line semimetal in three-dimensional graphene networks". Phys. Rev. B 92, 2015, p. 045108.

70. Y. Wu, L. Wang, E. Mun, D. Johnson, D. Mou, L. Huang, Y. Lee, S. Budḱo, P. Canfield, and A. Kaminski. "Dirac node arcs in $PtSn_4$". Nat. Phys. 12, 2016, p. 667.

71. G. Bian, T.-R. Chang, R. Sankar, S.-Y. Xu, H. Zheng, T. Neupert, C.-K. Chiu, S.-M. Huang, G. Chang, I. Belopolski, D. S. Sanchez, M. Neupane, N. Alidoust, C. Liu, B. Wang, C.-C. Lee, H.-T. Jeng, C. Zhang, Z. Yuan, S. Jia, A. Bansil, F. Chou, H. Lin, and M. Z. Hasan. "Topological nodal-line fermions in spin-orbit metal $PbTaSe_2$". Nat. Comm. 7, 2016, p. 10556.

72. M. Neupane, I. Belopolski, M. M. Hosen, D. S. Sanchez, R. Sankar, M. Szlawska, S.-Y. Xu, K. Dimitri, N. Dhakal, P. Maldonado, P. M. Oppeneer, D. Kaczorowski, F. Chou, M. Z. Hasan, and T. Durakiewicz. "Observation of topological nodal fermion semimetal phase in ZrSiS". Phys. Rev. B 93, 2016, 201104(R).

73. X. Wang, X. Pan, M. Gao, J. Yu, J. Jiang, J. Zhang, H. Zuo, M. Zhang, Z. Wei, W. Niu, Z. Xia, X. Wan, Y. Chen, F. Song, Y. Xu, B. Wang, G. Wang, and R. Zhang. "Evidence of Both Surface and Bulk Dirac Bands and Anisotropic Nonsaturating Magnetoresistance in ZrSiS". Adv. Elec. Mat. 2, 2016, p. 1600228.

74. M. N. Ali, L. M. Schoop, C. Garg, J. M. Lippmann, E. Lara, B. Lotsch, and S. S. P. Parkin. "Butterfly magnetoresistance, quasi-2D Dirac Fermi surface and topological phase transition in ZrSiS". Sci. Adv. 2, 2016, e1601742.

75. R. Singha, A. K. Pariari, B. Satpati, and P. Mandal. "Large nonsaturating magnetoresistance and signature of nondegenerate Dirac nodes in ZrSiS". Proc. Natl. Acad. Sci. 114, 2017, p. 2468.

76. J. Hu, Z. Tang, J. Liu, Y. Zhu, J. Wei, and Z. Mao. "Nearly massless Dirac fermions and strong Zeeman splitting in the nodal-line semimetal ZrSiS probed by de Haas–van Alphen quantum oscillations". Phys. Rev. B 96, 2017, p. 045127.

77. Y. Huh, E.-G. Moon, and Y. B. Kim. "Long-range Coulomb interaction in nodal-ring semimetals". Phys. Rev. B 93, 2016, p. 035138.

78. A. N. Rudenko, E. A. Stepanov, A. I. Lichtenstein, and M. I. Katsnelson. "Excitonic Instability and Pseudogap Formation in Nodal Line Semimetal ZrSiS". Phys. Rev. Lett. 120, 2018, p. 216401.

79. S. Pezzini, M. R. van Delft, L. M. Schoop, B. V. Lotsch, A. Carrington, M. I. Katsnelson, N. E. Hussey, and S. Wiedmann. "Unconventional mass enhancement around the Dirac nodal loop in ZrSiS". Nat. Phys. 14, 2018, p. 178.

80. M. R. van Delft. "Emergent phenomena in Weyl, nodal line and one-dimensional semimetals". Ph.D. thesis. Radboud Universiteit Nijmegen, 2019.

81. C. C. Gu, J. Hu, X. L. Chen, Z. P. Guo, B. T. Fu, Y. H. Zhou, C. An, Y. Zhou, R. R. Zhang, C. Y. Xi, Q. Y. Gu, C. Park, H. Y. Shu, W. G. Yang, L. Pi, Y. H. Zhang, Y. G. Yao, Z. R. Yang, J. H. Zhou, J. Sun, Z. Q. Mao, and M. L. Tian. "Experimental evidence of crystal symmetry protection for the topological nodal line semimetal state in ZrSiS". Phys. Rev. B 100, 2019, p. 205124.

82. R. Singha, S. Samanta, S. Chatterjee, A. Pariari, D. Majumdar, B. Satpati, L. Wang, A. Singha, and P. Mandal. "Probing lattice dynamics and electron-phonon coupling in the topological nodal-line semimetal ZrSiS". Phys. Rev. B 97, 2018, p. 094112.

83. D. VanGennep, T. A. Paul, C. W. Yerger, S. T. Weir, Y. K. Vohra, and J. J. Hamlin. "Possible pressure-induced topological quantum phase transition in the nodal line semimetal ZrSiS". Phys. Rev. B 99, 2019, p. 085204.

84. Y. Liu, Y. Y. Li, S. Rajput, D. Gilks, L. Lari, P. L. Galindo, M. Weinert, V. K. Lazarov, and L. Li. "Tuning Dirac states by strain in the topological insulator $Bi_2Se_3$". Nat. Phys. 10, 2014, p. 294.

85. J. Heui Hwang, S. Kwon, J. Park, J. Hun Kim, J. Lee, J. Sung Kim, H.-K. Lyeo, and J. Young Park. "Strain effects on in-plane conductance of the topological insulator $Bi_2Te_3$". Appl. Phys. Lett. 104, 2014, p. 161613.

86. A. Steppke, L. Zhao, M. E. Barber, T. Scaffidi, F. Jerzembeck, H. Rosner, A. S. Gibbs, Y. Maeno, S. H. Simon, A. P. Mackenzie, and C. W. Hicks. "Strong peak in $T_c$ of $Sr_2RuO_4$ under uniaxial pressure". Science 355, 2017, eaaf9398.

87. D. Wang, L. Chen, H. Liu, C. Shi, X. Wang, G. Cui, P. Zhang, and Y. Chen. "Strain induced band inversion and topological phase transition in methyl-decorated stanene film". Sci. Rep. 7, 2017, p. 17089.

88. C. Schindler, J. Noky, M. Schmidt, C. Felser, J. Wosnitza, and J. Gooth. "Effect of uniaxial stress on the electronic band structure of NbP". Phys. Rev. B 102, 2020, p. 035132.

89. W. Zhou, A. N. Rudenko, and S. Yuan. "Effect of Mechanical Strain on the Optical Properties of Nodal-Line Semimetal ZrSiS". Adv. Elec. Mat. 6, 2020, p. 1900860.

90. N. Kumar, Y. Sun, M. Nicklas, S. J. Watzman, O. Young, I. Leermakers, J. Hornung, J. Klotz, J. Gooth, K. Manna, V. Süß, S. N. Guin, T. Förster, M. Schmidt, L. Muechler, B. Yan, P. Werner, W. Schnelle, U. Zeitler, J. Wosnitza, S. S. P. Parkin, C. Felser, and C. Shekhar. "Extremely high conductivity observed in the triple point topological metal MoP". Nat. Comm. 10, 2019, p. 2475.

91. H. Cao, J. Tian, I. Miotkowski, T. Shen, J. Hu, S. Qiao, and Y. P. Chen. "Quantized Hall Effect and Shubnikov–de Haas Oscillations in Highly Doped $Bi_2Se_3$: Evidence for Layered Transport of Bulk Carriers". Phys. Rev. Lett. 108, 2012, p. 216803.

92. M. de Jong, W. Chen, T. Angsten, A. Jain, R. Notestine, A. Gamst, M. Sluiter, C. Krishna Ande, S. van der Zwaag, J. J. Plata, C. Toher, S. Curtarolo, G. Ceder, K. A. Persson, and M. Asta. "Charting the complete elastic properties of inorganic crystalline compounds". Sci. Data 2, 2015, p. 150009.

93. C. Friedrich, S. Blügel, and A. Schindlmayr. "Efficient implementation of the GW approximation within the all-electron FLAPW method". Phys. Rev. B 81, 2010, p. 125102.

94. J. P. Perdew, K. Burke, and M. Ernzerhof. "Generalized Gradient Approximation Made Simple". Phys. Rev. Lett. 77, 1996, pp. 3865–3868.

95. G. Pizzi, V. Vitale, R. Arita, S. Blügel, F. Freimuth, G. Géranton, M. Gibertini, D. Gresch, C. Johnson, T. Koretsune, J. Ibañez-Azpiroz, H. Lee, J.-M. Lihm, D. Marchand, A. Marrazzo, Y. Mokrousov, J. I. Mustafa, Y. Nohara, Y. Nomura, L. Paulatto, S. Poncé, T. Ponweiser, J. Qiao, F. Thöle, S. S. Tsirkin, M. Wierzbowska, N. Marzari, D. Vanderbilt, I. Souza, A. A. Mostofi, and J. R. Yates. "Wannier90 as a community code: new features and applications". J. of Phys.: Cond. Matt. 32, 2020, p. 165902.

96. A. Jain, S. P. Ong, G. Hautier, W. Chen, W. D. Richards, S. Dacek, S. Cholia, D. Gunter, D. Skinner, G. Ceder, and K. A. Persson. "Commentary: The Materials Project: A materials genome approach to accelerating materials innovation". APL Mat. 1, 2013, p. 011002.

97. Y. Mizuguchi, H. Fujihisa, Y. Gotoh, K. Suzuki, H. Usui, K. Kuroki, S. Demura, Y. Takano, H. Izawa, and O. Miura. "$BiS_2$-based layered superconductor $Bi_4O_4S_3$". Phys. Rev. B 86, 2012, p. 220510.

98. Y. Mizuguchi. "Material Development and Physical Properties of $BiS_2$-Based Layered Compounds". J. Phys. Soc. Jpn. 88, 2019, p. 041001.

99. Y. Mizuguchi, S. Demura, K. Deguchi, Y. Takano, H. Fujihisa, Y. Gotoh, H. Izawa, and O. Miura. "Superconductivity in Novel BiS2-Based Layered Superconductor $LaO_{1-x}F_xBiS_2$". J. Phys. Soc. Jpn. 81, 2012, p. 114725.

100. R. Higashinaka, T. Asano, T. Nakashima, K. Fushiya, Y. Mizuguchi, O. Miura, T. D. Matsuda, and Y. Aoki. "Pronounced –Log $T$ Divergence in Specific Heat of Nonmetallic $CeOBiS_2$: A Mother Phase of $BiS_2$-Based Superconductor". J. Phys. Soc. Jpn. 84, 2015, p. 023702.

101. R. Jha, A. Kumar, S. Kumar Singh, and V. P. S. Awana. "Synthesis and Superconductivity of New $BiS_2$ Based Superconductor $PrO_{0.5}F_{0.5}BiS_2$". J. Supercond. Nov. Magn. 26, 2013, pp. 499–502.

102. S. Demura, Y. Mizuguchi, K. Deguchi, H. Okazaki, H. Hara, T. Watanabe, S. James Denholme, M. Fujioka, T. Ozaki, H. Fujihisa, Y. Gotoh, O. Miura, T. Yamaguchi, H. Takeya, and Y. Takano. "New Member of $BiS_2$-Based Superconductor $NdO_{1-x}F_xBiS_2$". J. Phys. Soc. Jpn. 82:3, 2013, p. 033708.

103. K. Hoshi, H. Arima, N. Kataoka, M. Ochi, A. Yamashita, A. de Visser, T. Yokoya, K. Kuroki, and Y. Mizuguchi. "Controlling of Localization by Elemental-substitution Effect in Layered $BiCh_2$-based Compounds $LaO_{1-x}F_xBiS_{2-y}Se_y$". J. Phys. Soc. Jpn. 92, 2023, p. 054704.

104. K. Hoshi, R. Kurihara, Y. Goto, M. Tokunaga, and Y. Mizuguchi. "Extremely high upper critical field in $BiCh_2$-based (Ch: S and Se) layered superconductor $LaO_{0.5}F_{0.5}BiS_{2-x}Se_x$ (x = 0.22 and 0.69)". Sci. Rep. 12, 2022, p. 288.

105. K. Hoshi and Y. Mizuguchi. "Experimental overview on pairing mechanisms of $BiCh_2$-based (Ch: S, Se) layered superconductors". J. Phys.: Cond. Matt. 33, 2021, p. 473001.

106. A. M. Clogston. "Upper Limit for the Critical Field in Hard Superconductors". Phys. Rev. Lett. 9, 1962, pp. 266–267.

107. D. Srivastava, G. C. Tewari, M. Karppinen, and R. M. Nieminen. "First-principles study of layered antiferromagnetic $CuCrX_2$ (X = S, Se and Te)". J. Phys.: Cond. Matt. 25, 2013, p. 105504.

108. L. Jiao, Z. Weng, J. Liu, J. Zhang, G. Pang, C. Guo, F. Gao, X. Zhu, H.-H. Wen, and H. Q. Yuan. "Evidence for nodeless superconductivity in $NdO_{1-x}F_xBiS_2$ (x = 0.3 and 0.5) single crystals". J. Phys.: Cond. Matt. 27, 2015, p. 225701.

109. N. Kase, Y. Terui, T. Nakano, and N. Takeda. "Superconducting gap symmetry of the $BiS_2$-based superconductor $LaO_{0.5}F_{0.5}BiSSe$ elucidated through specific heat measurements". Phys. Rev. B 96, 2017, p. 214506.

110. N. Kase. "Specific Heat Study of the $BiS_2$-Based Superconductor". J. Phys. Soc. Jpn. 88, 2019, p. 041007.

111. N. R. Werthamer, E. Helfand, and P. C. Hohenberg. "Temperature and Purity Dependence of the Superconducting Critical Field, $H_{c2}$. III. Electron Spin and Spin-Orbit Effects". Phys. Rev. 147, 1966, pp. 295–302.

112. D. Maruyama, M. Sigrist, and Y. Yanase. "Locally Non-centrosymmetric Superconductivity in Multilayer Systems". J. Phys. Soc. Jpn. 81, 2011, p. 3.

113. S.-L. Wu, K. Sumida, K. Miyamoto, K. Taguchi, T. Yoshikawa, A. Kimura, Y. Ueda, M. Arita, M. Nagao, S. Watauchi, I. Tanaka, and T. Okuda. "Direct evidence of hidden local spin polarization in a centrosymmetric superconductor $LaO_{0.55}F_{0.45}BiS_2$". Nat. Comm. 8, 2017, p. 1919.

114. O. Zheliuk, J. M. Lu, Q. H. Chen, A. A. E. Yumin, S. Golightly, and J. T. Ye. "Josephson coupled Ising pairing induced in suspended $MoS_2$ bilayers by double-side ionic gating". Nat. Nanotech. 14, 2019, pp. 1123–1128.

115. R. Masutomi, T. Okamoto, and Y. Yanase. "Unconventional superconducting phases in multilayer films with layer-dependent Rashba spin-orbit interactions". Phys. Rev. B 101, 2020, p. 184502.

116. M. V. Salis. "Experimental Investigation of $PdTe_2$, doped $PdTe_2$ and $BiCh_2$ Superconductors". PhD thesis. University of Amsterdam, 2023.

117. M. Nagao. "Growth and characterization of R(O,F)$BiS_2$ (R = La, Ce, Pr, Nd) superconducting single crystals". Nov. Supercond. Mat. 1, 2015, p. 1.

118. A. C. Mark and R. J. Hemley. "On the lineshapes of temperature-dependent transport measurements of superconductors under pressure". arXiv, 2024.

119. Y. C. Chan, K. Y. Yip, Y. W. Cheung, Y. T. Chan, Q. Niu, J. Kajitani, R. Higashinaka, T. D. Matsuda, Y. Yanase, Y. Aoki, K. T. Lai, and S. K. Goh. "Anisotropic two-gap superconductivity and the absence of a Pauli paramagnetic limit in single-crystalline $LaO_{0.5}F_{0.5}BiS_2$". Phys. Rev. B 97, 2018, p. 104509.

120. N. T. Huy, A. Gasparini, D. E. de Nijs, Y. Huang, J. C. P. Klaasse, T. Gortenmulder, A. de Visser, A. Hamann, T. Görlach, and H. v. Löhneysen. "Superconductivity on the Border of Weak Itinerant Ferromagnetism in UCoGe". Phys. Rev. Lett. 99, 2007, p. 067006.

121. S. Ran, C. Eckberg, Q.-P. Ding, Y. Furukawa, T. Metz, S. R. Saha, I.-L. Liu, M. Zic, H. Kim, J. Paglione, and N. P. Butch. "Nearly ferromagnetic spin-triplet superconductivity". Science 365:6454, 2019, pp. 684–687.

122. N. Hayashi, K. Wakabayashi, P. A. Frigeri, and M. Sigrist. "Temperature dependence of the superfluid density in a noncentrosymmetric superconductor". Phys. Rev. B 73, 2006, p. 024504.

123. L. P. Gor'kov and E. I. Rashba. "Superconducting 2D System with Lifted Spin Degeneracy: Mixed Singlet-Triplet State". Phys. Rev. Lett. 87, 2001, p. 037004.

124. T. Yoshida, M. Sigrist, and Y. Yanase. "Parity-Mixed Superconductivity in Locally Non-centrosymmetric System". J. Phys. Soc. Jpn. 83:1, 2014, p. 013703.

125. Y. Yang, W.-S. Wang, Y.-Y. Xiang, Z.-Z. Li, and Q.-H. Wang. "Triplet pairing and possible weak topological superconductivity in $BiS_2$-based superconductors". Phys. Rev. B 88, 2013, p. 094519.

126. T. Yoshida, M. Sigrist, and Y. Yanase. "Complex-Stripe Phases Induced by Staggered Rashba Spin–Orbit Coupling". J. Phys. Soc. Jpn. 82:7, 2013, p. 074714.

127. O. Prakash, A. Kumar, A. Thamizhavel, and S. Ramakrishnan. "Evidence for bulk superconductivity in pure bismuth single crystals at ambient pressure". Science 355, 2017, pp. 52–55.

128. V. G. Peschanskii and Y. A. Kolesnichenko. "On the 60th anniversary of the Lifshitz-Kosevich theory". Low Temp. Phys. 40, 2014, pp. 267–269.

129. I. Aguilera, C. Friedrich, and S. Blügel. "Electronic phase transitions of bismuth under strain from relativistic self-consistent $GW$ calculations". Phys. Rev. B 91, 2015, p. 125129.

130. C. L. Kane and E. J. Mele. "$Z_2$ Topological Order and the Quantum Spin Hall Effect". Phys. Rev. Lett. 95, 2005, p. 146802.

131. L. Fu, C. L. Kane, and E. J. Mele. "Topological Insulators in Three Dimensions". Phys. Rev. Lett. 98, 2007, p. 106803.

132. C. R. Ast and H. Höchst. "Electronic structure of a bismuth bilayer". Phys. Rev. B 67, 2003, p. 113102.

133. Y. M. Koroteev, G. Bihlmayer, J. E. Gayone, E. V. Chulkov, S. Blügel, P. M. Echenique, and P. Hofmann. "Strong Spin-Orbit Splitting on Bi Surfaces". Phys. Rev. Lett. 93, 2004, p. 046403.

134. P. Hofmann. "The surfaces of bismuth: Structural and electronic properties". Prog. in Surf. Sci. 81, 2006, pp. 191–245.

135. E. Tichovolsky and J. Mavroides. "Magnetoreflection studies on the band structure of bismuth-antimony alloys". Solid State Comm. 7, 1969, pp. 927–931.

136. O. V. Yazyev, E. Kioupakis, J. E. Moore, and S. G. Louie. "Quasiparticle effects in the bulk and surface-state bands of $Bi_2Se_3$ and $Bi_2Te_3$ topological insulators". Phys. Rev. B 85, 2012, p. 161101.

137. I. Aguilera, C. Friedrich, G. Bihlmayer, and S. Blügel. "*GW* study of topological insulators $Bi_2Se_3$, $Bi_2Te_3$, and $Sb_2Te_3$: Beyond the perturbative one-shot approach". Phys. Rev. B 88, 2013, p. 045206.

138. M. Maltz and M. S. Dresselhaus. "Magnetoreflection Studies in Bismuth". Phys. Rev. B 2, 1970, pp. 2877–2887.

139. M. P. Vecchi and M. S. Dresselhaus. "Temperature dependence of the band parameters of bismuth". Phys. Rev. B 10, 1974, pp. 771–774.

140. R. T. Isaacson and G. A. Williams. "Alfvén-Wave Propagation in Solid-State Plasmas. III. Quantum Oscillations of the Fermi Surface of Bismuth". Phys. Rev. 185, 1969, pp. 682–688.

141. R. N. Brown, J. G. Mavroides, and B. Lax. "Magnetoreflection in Bismuth". Phys. Rev. 129, 1963, pp. 2055–2061.

142. G. E. Smith, G. A. Baraff, and J. M. Rowell. "Effective *g* Factor of Electrons and Holes in Bismuth". Phys. Rev. 135, 1964, A1118–A1124.

143. V. S. Edel'man. J. Exp. Theor. Phys. 41, 1975, p. 125.

144. R. J. Dinger and A. W. Lawson. "Cyclotron Resonance and the Cohen Nonellipsoidal Nonparabolic Model for Bismuth. III. Experimental Results". Phys. Rev. B 7, 1973, pp. 5215–5227.

145. Z. Zhu, B. Fauqué, K. Behnia, and Y. Fuseya. "Magnetoresistance and valley degree of freedom in bulk bismuth". Journal of Physics: Condensed Matter 30, 2018, p. 313001.

146. Z. Zhu, B. Fauqué, Y. Fuseya, and K. Behnia. "Angle-resolved Landau spectrum of electrons and holes in bismuth". Phys. Rev. B 84, 2011, p. 115137.

147. N. B. Brandt, V. A. Kul'Bachinskiĭ, and N. Y. Minina. "Effect of tension on the Fermi surface in bismuth". Sov. J. of Exp. and Theor. Phys. Lett. 26, 1977, p. 162.

148. N. B. Brandt, V. A. Kul'Bachinskiĭ, N. Y. Minina, and V. D. Shirokikh. "Change of the band structure and electronic phase transitions of Bi and $Bi_{1-x}Sb_x$ alloys under uniaxial tension strains". Sov. J. of Exp. and Theor. Phys. Lett. 51, 1980, pp. 562–571.

149. S. Hosoi, F. Tachibana, M. Sakaguchi, K. Ishida, M. Shimozawa, K. Izawa, Y. Fuseya, Y. Kinoshita, and M. Tokunaga. "Effects of strain-tunable valleys on charge transport in bismuth". Phys. Rev. Res. 6, 2024, p. 033096.

150. M. Cankurtaran, H. Celik, and T. Alper. "Ultrasonic quantum oscillations in semimetallic $Bi_{1-x}Sb_x$ alloys". J. of Phys. F: Metal Phys. 15, 1985, p. 391.

151. B. Lax, J. G. Mavroides, H. J. Zeiger, and R. J. Keyes. "Infrared Magnetoreflection in Bismuth. I. High Fields". Phys. Rev. Lett. 5, 1960, pp. 241–243.

152. S. Golin. "Band Model for Bismuth-Antimony Alloys". Phys. Rev. 176, 1968, pp. 830–832.

153. T. Teramoto, T. Komine, S. Yamamoto, M. Kuraishi, R. Sugita, Y. Hasegawa, and H. Nakamura. "Influence of the band structure of BiSb alloy on the magneto-Seebeck coefficient". J. of Appl. Phys. 104, 2008, p. 053714.

154. URL: https://www.goodfellow.com/.

155. URL: https://mateck.com/en/.

156. A. Gourgout, A. Marguerite, B. Fauqué, and K. Behnia. "Electronic thermal resistivity and quasiparticle collision cross section in semimetals". Phys. Rev. B 110, 2024, p. 155119.

157. W. Kang, F. Spathelf, B. Fauqué, Y. Fuseya, and K. Behnia. "Boundary conductance in macroscopic bismuth crystals". Nat. Commun. 13, 2022, p. 189.

158. F. Spathelf, B. Fauqué, and K. Behnia. "Magneto-Seebeck effect in bismuth". Phys. Rev. B 105, 2022, p. 235116.

159. P. Brown. "High-pressure states of bismuth". PhD thesis. University of Cambridge, 2017.

160. R. N. Bhargava. "de Haas-van Alphen and Galvanomagnetic Effect in Bi and Bi-Pb Alloys". Phys. Rev. 156, 1967, pp. 785–797.

161. M. C. Steele and J. Babiskin. "Oscillatory Thermomagnetic Properties of a Bismuth Single Crystal at Liquid Helium Temperatures". Phys. Rev. 98, 1955, pp. 359–367.

162. C. Li, J. C. de Boer, B. de Ronde, S. V. Ramankutty, E. van Heumen, Y. Huang, A. de Visser, A. A. Golubov, M. S. Golden, and A. Brinkman. "$4\pi$-periodic Andreev bound states in a Dirac semimetal". Nature Mater. 17, 2018, pp. 875–880.

163. J. C. de Boer, D. H. Wielens, J. A. Voerman, B. de Ronde, Y. Huang, M. S. Golden, C. Li, and A. Brinkman. "Nonlocal signatures of the chiral magnetic effect in the Dirac semimetal $Bi_{0.97}Sb_{0.03}$". Phys. Rev. B 99, 2019, p. 085124.

164. HQ Graphene. URL: https://www.hqgraphene.com/index.php.

165. J. P. Lorenz. Uniaxial stress measurements using the CS100 cryostrain cell. MSc. thesis. University of Amsterdam, 2021, unpublished.

166. C. Schindler. "Uniaxial-stress response, electron-phonon interaction, and magnetic interactions in topological semimetals and narrow-gap semiconductors". Ph.D. thesis. Technical University Dresden, 2021.

167. C. W. Nicholson, M. Rumo, A. Pulkkinen, G. Kremer, B. Salzmann, M.-L. Mottas, B. Hildebrand, T. Jaouen, T. K. Kim, S. Mukherjee, K. Ma, M. Muntwiler, F. O. von Rohr, C. Cacho, and C. Monney. "Uniaxial strain-induced phase transition in the 2D topological semimetal $IrTe_2$". Comm. Mat. 2, 2021, p. 25.

168. S. Manzeli, D. Ovchinnikov, D. Pasquier, O. V. Yazyev, and A. Kis. "2D transition metal dichalcogenides". Nat. Rev. Mat. 2, 2017, p. 17033.

169. G. Gruner. Density waves in solids. 1st edn. Addison-Wesley, 1994.

170. A. Soumyanarayanan, M. M. Yee, Y. He, J. van Wezel, D. J. Rahn, K. Rossnagel, E. W. Hudson, M. R. Norman, and J. E. Hoffman. "Quantum phase transition from triangular to stripe charge order in $NbSe_2$". PNAS 110, 2013, pp. 1623–1627.

171. S. Gao, F. Flicker, R. Sankar, H. Zhao, Z. Ren, B. Rachmilowitz, S. Balachandar, F. Chou, K. S. Burch, Z. Wang, J. van Wezel, and I. Zeljkovic. "Atomic-scale strain manipulation of a charge density wave". PNAS 115, 2018, pp. 6986–6990.

172. F. Flicker and J. van Wezel. "Charge ordering geometries in uniaxially strained $NbSe_2$". Phys. Rev. B 92, 2015, p. 201103.

173. F. Flicker and J. van Wezel. "Charge order in $NbSe_2$". Phys. Rev. B 94, 2016, p. 235135.

174. Hoffman Lab. URL: https://hoffman.physics.harvard.edu/.

175. A. Wieteska, B. Foutty, Z. Guguchia, F. Flicker, B. Mazel, L. Fu, S. Jia, C. Marianetti, J. van Wezel, and A. Pasupathy. Uniaxial strain tuning of superconductivity in $2H$-$NbSe_2$. 2019.

176. S. Levelt. Uniaxial strain as tuning parameter in superconductors. BSc. thesis. University of Amsterdam, 2021, unpublished.

177. M. S. Bahramy, O. J. Clark, B.-J. Yang, J. Feng, L. Bawden, J. M. Riley, I. Markovi'c, F. Mazzola, V. Sunko, D. Biswas, S. P. Cooil, M. Jorge, J. W. Wells, M. Leandersson, T. Balasubramanian, J. Fujii, I. Vobornik, J. E. Rault, T. K. Kim, M. Hoesch, K. Okawa, M. Asakawa, T. Sasagawa, T. Eknapakul, W. Meevasana, and P. D. C. King. "Ubiquitous formation of bulk Dirac cones and topological surface states from a single orbital manifold in transition-metal dichalcogenides". Nat. Mat. 17, 2018, pp. 21–28.

178. N. Matsumoto, K. Taniguchi, R. Endoh, H. Takano, and S. Nagata. "Resistance and susceptibility anomalies in $IrTe_2$ and $CuIrTe_4$". J. Low T. Phys. 117, 1999, pp. 1129–1133.

179. P.-J. Hsu, T. Mauerer, M. Vogt, J. J. Yang, Y. S. Oh, S.-W. Cheong, M. Bode, and W. Wu. "Hysteretic Melting Transition of a Soliton Lattice in a Commensurate Charge Modulation". Phys. Rev. Lett. 111, 2013, p. 266401.

180. C. Chen, J. Kim, Y. Yang, G. Cao, R. Jin, and E. W. Plummer. "Surface phases of the transition-metal dichalcogenide $IrTe_2$". Phys. Rev. B 95, 2017, p. 094118.

181. G. L. Pascut, K. Haule, M. J. Gutmann, S. A. Barnett, A. Bombardi, S. Artyukhin, T. Birol, D. Vanderbilt, J. J. Yang, S.-W. Cheong, and V. Kiryukhin. "Dimerization-Induced Cross-Layer Quasi-Two-Dimensionality in Metallic $IrTe_2$". Phys. Rev. Lett. 112, 2014, p. 086402.

182. G. Saleh and S. Artyukhin. "First-principles theory of phase transitions in $IrTe_2$". J. Phys. Chem. Lett. 11, 2020, pp. 2127–2132.

183. A. F. Fang, G. Xu, T. Dong, P. Zheng, and N. L. Wang. "Structural phase transition in $IrTe_2$: A combined study of optical spectroscopy and band structure calculations". Sci. Rep. 3, 2013, p. 1153.

184. D. Ootsuki, S. Pyon, K. Kudo, M. Nohara, M. Horio, T. Yoshida, A. Fujimori, M. Arita, H. Anzai, H. Namatame, M. Taniguchi, N. L. Saini, and T. Mizokawa. "Electronic Structure Reconstruction by Orbital Symmetry Breaking in $IrTe_2$". J. Phys. Soc. Jpn. 82, 2013, p. 093704.

185. H. Cao, B. C. Chakoumakos, X. Chen, J. Yan, M. A. McGuire, H. Yang, R. Custelcean, H. Zhou, D. J. Singh, and D. Mandrus. "Origin of the phase transition in $IrTe_2$: Structural modulation and local bonding instability". Phys. Rev. B 88, 2013, p. 115122.

186. Y. S. Oh, J. J. Yang, Y. Horibe, and S.-W. Cheong. "Anionic Depolymerization Transition in $IrTe_2$". Phys. Rev. Lett. 110, 2013, p. 127209.

187. G. L. Pascut, T. Birol, M. J. Gutmann, J. J. Yang, S.-W. Cheong, K. Haule, and V. Kiryukhin. "Series of alternating states with unpolarized and spin-polarized bands in dimerized $IrTe_2$". Phys. Rev. B 90, 2014, p. 195122.

188. J. Dai, K. Haule, J. J. Yang, Y. S. Oh, S.-W. Cheong, and W. Wu. "Hierarchical stripe phases in $IrTe_2$ driven by competition between Ir dimerization and Te bonding". Phys. Rev. B 90, 2014, p. 235121.

189. Q. Li, W. Lin, J. Yan, X. Chen, A. G. Gianfrancesco, D. J. Singh, D. Mandrus, S. V. Kalinin, and M. Pan. "Bond competition and phase evolution on the $IrTe_2$ surface". Nat. Comm. 5, 2014, p. 5358.

190. S. Pyon, K. Kudo, and M. Nohara. "Superconductivity Induced by Bond Breaking in the Triangular Lattice of $IrTe_2$". J. Phys. Soc. Jap. 81, 2012, p. 053701.

191. S. Pyon, K. Kudo, and M. Nohara. "Emergence of superconductivity near the structural phase boundary in Pt-doped $IrTe_2$ single crystals". Physica C 494, 2013, pp. 80–84.

192. O. Ivashko, L. Yang, D. Destraz, E. Martino, Y. Chen, C. Y. Guo, H. Q. Yuan, A. Pisoni, P. Matus, S. Pyon, K. Kudo, M. Nohara, L. Forr'o, H. M. Rønnow, M. H"ucker, M. v. Zimmermann, and J. Chang. "Charge-Stripe Order and Superconductivity in $Ir_{1-x}Pt_xTe_2$". Sci. Rep. 7, 2017, p. 17157.

193. C. Felser, E. W. Finckh, H. Kleinke, F. Rocker, and W. Tremel. "Electronic properties of $ZrTe_3$". J. Mater. Chem. 8, 1998, pp. 1787–1798.

194. K. Yamaya, S. Takayanagi, and S. Tanda. "Mixed bulk-filament nature in superconductivity of the charge-density-wave conductor $ZrTe_3$". Phys. Rev. B 85, 2012, p. 184513.

195. R. Yomo, K. Yamaya, M. Abliz, M. Hedo, and Y. Uwatoko. "Pressure effect on competition between charge density wave and superconductivity in $ZrTe_3$: Appearance of pressure-induced reentrant superconductivity". Phys. Rev. B 71, 2005, p. 132508.

196. X. Zhu, H. Lei, and C. Petrovic. "Coexistence of Bulk Superconductivity and Charge Density Wave in $Cu_xZrTe_3$". Phys. Rev. Lett. 106, 2011, p. 246404.

197. X. Zhu, B. Lv, F. Wei, Y. Xue, B. Lorenz, L. Deng, Y. Sun, and C.-W. Chu. "Disorder-induced bulk superconductivity in $ZrTe_3$ single crystals via growth control". Phys. Rev. B 87, 2013, p. 024508.

198. A. J. Berlinsky. "One-dimensional metals and charge density wave effects in these materials". Rep. Prog. Phys. 42, 1979, p. 1243.

199. M. Hoesch, X. Cui, K. Shimada, C. Battaglia, S. Fujimori, and H. Berger. "Splitting in the Fermi surface of $ZrTe_3$: A surface charge density wave system". Phys. Rev. B 80, 2009, p. 075423.

200. J. Hu, Z. Tang, J. Liu, X. Liu, Y. Zhu, D. Graf, K. Myhro, S. Tran, C. N. Lau, J. Wei, and Z. Mao. "Evidence of Topological Nodal-Line Fermions in ZrSiSe and ZrSiTe". Phys. Rev. Lett. 117, 2016, p. 016602.

201. C. Wang and T. Hughbanks. "Main Group Element Size and Substitution Effects on the Structural Dimensionality of Zirconium Tellurides of the Zr-SiS Type". Inorg. Chem. 34, 1995, pp. 5524–5529.

202. Q. Xu, Z. Song, S. Nie, H. Weng, Z. Fang, and X. Dai. "Two-dimensional oxide topological insulator with iron-pnictide superconductor LiFeAs structure". Phys. Rev. B 92, 2015, p. 205310.

203. M. M. Hosen, K. Dimitri, I. Belopolski, P. Maldonado, R. Sankar, N. Dhakal, G. Dhakal, T. Cole, P. M. Oppeneer, D. Kaczorowski, F. Chou, M. Z. Hasan, T. Durakiewicz, and M. Neupane. "Tunability of the topological nodal-line semimetal phase in ZrSiX-type materials (X = S, Se, Te)". Phys. Rev. B 95, 2017, p. 161101.

204. J. P. Lorenz, J. F. Linnartz, A. Kool, M. R. van Delft, W. Guo, I. Aguilera, R. Singha, L. M. Schoop, N. E. Hussey, S. Wiedmann, and A. de Visser. "Uniaxial strain effects on the Fermi surface and quantum mobility of the Dirac nodal-line semimetal ZrSiS". Phys. Rev. B 109, 2024, p. 235114.

205. K. Hoshi, S. Sakuragi, T. Yajima, Y. Goto, A. Miura, C. Moriyoshi, Y. Kuroiwa, and Y. Mizuguchi. "Structural Phase Diagram of $LaO_{1-x}F_xBiSSe$: Suppression of the Structural Phase Transition by Partial F Substitutions". Cond. Matt. 5, 2020, p. 81.

206. K. Hoshi, M. Kimata, Y. Goto, T. D. Matsuda, and Y. Mizuguchi. "Two-Fold-Symmetric Magnetoresistance in Single Crystals of Tetragonal $BiCh_2$-Based Superconductor $LaO_{0.5}F_{0.5}BiSSe$". J. Phys. Soc. Jap. 88, 2019, p. 033704.

207. K. Hoshi, M. Kimata, Y. Goto, A. Miura, C. Moriyoshi, Y. Kuroiwa, M. Nagao, and Y. Mizuguchi. "Two-fold symmetry of in-plane magnetoresistance anisotropy in the superconducting states of $BiCh_2$-based $LaO_{0.9}F_{0.1}BiSSe$ single crystal". J. Phys. Comm. 4, 2020, p. 095028.

208. Y. Pan, A. M. Nikitin, G. K. Araizi, Y. K. Huang, Y. Matsushita, T. Naka, and A. de Visser. "Rotational symmetry breaking in the topological superconductor $Sr_xBi_2Se_3$ probed by upper-critical field experiments". Sci. Rep. 6, 2016, p. 28632.

209. S. Yonezawa. "Nematic Superconductivity in Doped $Bi_2Se_3$ Topological Superconductors". Cond. Matt. 4, 2019, p. 2.

210. I. Kostylev, S. Yonezawa, Y. Wang Z. Ando, and Y. Maeno. "Uniaxial-strain control of nematic superconductivity in $Sr_xBi_2Se_3$". Nat. Comm. 11, 2020, p. 4152.

211. S. Y. Zhou, G.-H. Gweon, J. Graf, A. V. Fedorov, C. D. Spataru, R. D. Diehl, Y. Kopelevich, D.-H. Lee, S. G. Louie, and A. Lanzara. "First direct observation of Dirac fermions in graphite". Nat. Phys. 2, 2006, pp. 595–599.

212. I. A. Luk'yanchuk, Y. Kopelevich, and M. El Marssi. "Dirac Fermions in graphite: The state of art". Phys. B: Cond. Matt. 404, 2009, pp. 404–406.

213. I. A. Luk'yanchuk and Y. Kopelevich. "Dirac and Normal Fermions in Graphite and Graphene: Implications of the Quantum Hall Effect". Phys. Rev. Lett. 97, 2006, p. 256801.

214. P. Esquinazi, A. Setzer, R. Höhne, C. Semmelhack, Y. Kopelevich, D. Spemann, T. Butz, B. Kohlstrunk, and M. Lösche. "Ferromagnetism in oriented graphite samples". Phys. Rev. B 66, 2002, p. 024429.

215. Y. Kopelevich, J. H. S. Torres, R. R. da Silva, F. Mrowka, H. Kempa, and P. Esquinazi. "Reentrant Metallic Behavior of Graphite in the Quantum Limit". Phys. Rev. Lett. 90, 2003, p. 156402.

216. I. A. Luk'yanchuk and Y. Kopelevich. "Phase Analysis of Quantum Oscillations in Graphite". Phys. Rev. Lett. 93, 2004, p. 166402.

217. B. C. Camargo, Y. Kopelevich, A. Usher, and S. B. Hubbard. "Effect of structural disorder on quantum oscillations in graphite". Appl. Phys. Lett. 108, 2016, p. 031604.

218. G. Hadjisavvas, L. Tsetseris, and S. T. Pantelides. "The Origin of Electron Mobility Enhancement in Strained MOSFETs". IEEE Elec. Dev. Lett. 28, 2007, pp. 1018–1020.

# List of publications

1. M. V. Salis, **J. P. Lorenz**, Y. K. Huang and A. de Visser, *Disorder-induced transition from type-I to type-II superconductivity in the Dirac semimetal $PdTe_2$*, (**2022**) Phys. Rev. B 105, 054508

2. **J. P. Lorenz**, J. F. Linnartz, A. Kool, M. R. van Delft, W. Guo, I. Aguilera, R. Singha, L. M. Schoop, N. E. Hussey, S. Wiedmann and A. de Visser, *Uniaxial strain effects on the Fermi surface and quantum mobility of the Dirac nodal-line semimetal ZrSiS*, (**2024**) Phys. Rev. B 109, 235114
*[Chapter 3]*

3. J. F. Linnartz, A. Kool, **J. P. Lorenz**, C. S. A. Müller, M. R. van Delft, R. Singha, L. M. Schoop, N. E. Hussey, A. de Visser and S. Wiedmann, *Unraveling magneto-elastoresistance in the Dirac nodal-line semi-metal ZrSiSe*, (**2024**) npj Quantum Mater. 9, 63

# Summary

This thesis describes a number of experiments in which electronic transport was used to probe high magnetic field and uniaxial strain effects on various quantum materials. After a basic introduction on quantum materials, uniaxial strain and quantum oscillations, an overview is provided of experimental aspects relevant to work performed during this PhD. The underdoped iron pnictide $Ba(Fe_{1-x}Co_x)_2As_2$ was successfully used as a benchmark material in order to verify proper functionality of the used Razorbill strain cells and mounting method. Experimental investigation focused on single crystals of four different types of quantum materials: Dirac nodal-line semimetals, bismuth dichalcogenides, elements, and transition metal di- and trichalcogenides.

In this work the established Dirac nodal-line semimetal ZrSiS has been further investigated in order to elucidate the effect of uniaxial strain on its delicate electronic structure. The magnetoresistance of a sample was measured under tensile (up to 0.34 %) and compressive (up to $-0.28$ %) strain exerted along the $a$ axis and in magnetic fields up to 30 T. A systematic weakening of the peak structure in the Shubnikov-de Haas frequency spectrum was observed upon changing from compressive to tensile strain. This effect may be explained by a decrease in the effective quantum mobility upon decreasing the $c/a$ ratio, which is corroborated by a concurrent increase in the Dingle temperature.

A second Dirac nodal-line semimetal that was studied is ZrSiTe. We aimed to study its magnetoresistance to gain a better understanding of the effect of uniaxial strain on the magneto-elastoresistance and Shubnikov-de Haas oscillations of ZrSiTe. This would allow for the results to be linked to those of its sister compounds ZrSiS and ZrSiSe, which have both been uniaxially strained previously. Since de Haas-van Alphen oscillations have been observed experimentally in ZrSiTe in the past, it was somewhat expected our sample would exhibit Shubnikov-de Haas oscillations as well. However, the oscillations were absent in our measured sample, attributed to the small residual resistance ratio (7.7) of our sample and the fact that the de Haas-van Alphen oscillations in the literature were quite weak.

From a new family of layered superconductors, the bismuth dichalcogenide $LaO_{0.8}F_{0.2}BiS_{2-x}Se_x$ ($x = 0.5$ and $x = 1.0$) was characterized at higher

magnetic fields than before with the aim to better comprehend the extremely large in-plane $B_{c2}$. Typically attributed to its local inversion symmetry-induced Rashba-type spin-orbit coupling, the $B_{c2}$ greatly exceeds the conventional paramagnetic and orbital limits. Our research specifically aimed to examine how the Josephson vortex state in relation to the local inversion symmetry could be the key mechanism responsible for the high $B_{c2}$. Our data shows no change in the upwards trend of the $B_{c2}$ as $T$ approaches 0 K. Additionally, the calculated out-of-plane coherence lengths $\xi_{\perp}(0)$ are not small enough to suggest the presence of Josephson vortices, leading us to reason that there is no Josephon vortex state present in this family of $BiCh_2$-based superconductors. Further research could perhaps provide a more decisive picture regarding the dimensionality of $BiCh_2$-based systems at low temperatures, perhaps corroborating our findings.

Uniaxial strain experiments were performed on $LaO_{0.8}F_{0.2}BiSSe$, one of the two doping levels of the crystals mentioned above. We observed a substantial decrease in $B_{c2}$ and a small decrease in $T_c$ when uniaxial stress was applied along the $a$ axis, similar to the nematic superconductor $Sr_xBi_2Se_3$, validating our aim to explore the effect of uniaxial strain on the nematic superconductivity of $LaO_{0.8}F_{0.2}BiSSe$. The bowtie mounting method was used, reaffirming its potential and verifying its functionality. In the future, strain studies could perform uniaxially strained $B_{c2}$ and $T_c$ measurements along other axes, possibly shining light on the strain-tunability of nematic superconductors with a tetragonal crystal structure.

A uniaxial strain study on bulk bismuth (Bi) and doped bismuth ($Bi_{0.96}Sb_{0.04}$) was performed with the intention of bridging the gap between theoretical literature and previous experimental studies on bismuth, ideally gaining a better understanding of the three-dimensional topological properties of bismuth under strain. We report the observation of two systematic strain effects: a change in quantum mobility with strain, and a frequency shift, likely due to a change in quasiparticle pocket size with strain and implying a lifting of electron pocket degeneracy in line with the literature. Though theoretically predicted, no apparent trivial to topological or semimetal to semiconductor phase transitions were observed in either Bi or $Bi_{0.96}Sb_{0.04}$, suggesting our strain amounts were too low and prompting future research to perform a uniaxial strain study on bismuth using larger strains.

Highly oriented pyrolitic graphite was exploratively investigated using uniaxial strain with the aim to know more about the effect of uniaxial strain on materials with a topological character. A small change in fast Fourier transform amplitude with tensile strain was observed, which was linked to a change in quantum mobil-

ity. This could be the result of increased crystallite alignment, as that would lower structural disorder and enhance quantum oscillatory phenomena. Future uniaxial strain studies could aim to apply strains of a larger magnitude.

With the goal being to improve the understanding of the competition between the superconducting phase and charge density wave phase, $NbSe_2$ and $ZrTe_3$ were experimented on using uniaxial strain. No shift in $T_c$ or $T_{cdw}$ was detected for both materials. With the literature predicting otherwise, it leads one to believe that the absence of uniaxial strain effects is perhaps the result of the strain values not being large enough to sufficiently change the band structure of the materials in a way that it would alter the measured resistance data. Future studies should aim to perform similar experiments at higher strain values while remaining within the elastic regime of the samples.

$IrTe_2$ is a transition metal dichalcogenide like $NbSe_2$, but owes its charge ordered phase not to charge density wave physics but to dimer formation. With the intent of studying the strain tunability of $T_s$ and its effect on $T_c$, uniaxial strain experiments were successfully performed on $IrTe_2$ using the bowtie method, but no change in $T_s$ or $T_c$ with strain was observed. With no availability of samples large enough for the conventional mounting method, and since the conventional mounting method tends to be more reliable, future studies could aim to acquire larger samples and corroborate our results.

Overall, we hope the work presented in this thesis has added value to the foundation of uniaxial strain research, which is in its early stages. The ability to measure the electronic properties of crystals at higher strain values is desirable, emphasized both here and in recent review papers [29, 43]. With plenty of new and interesting physics still to be discovered, we firmly believe that uniaxial strain will continue to be an invaluable tuning parameter for the elucidation of emergent phenomena in quantum materials.

# Samenvatting

Dit proefschrift beschrijft een aantal experimenten waarbij electronisch transport gebruikt was om het effect van hoge velden en uniaxiale deformatie op diverse kwantummaterialen te onderzoeken. Na een fundamentele introductie op het gebied van kwantummaterialen, uniaxiale deformatie en kwantum oscillaties volgt een overzicht van de relevante experimentele aspecten van het werk dat is uitgevoerd tijdens dit promotietraject. De ondergedoopte ijzerpnictide $Ba(Fe_{1-x}Co_x)_2As_2$ is op een geslaagde wijze gebruikt als maatstaf om de functionaliteit van het Razorbill deformatie-apparaat en de montagemethode te verifiëren. Experimenteel onderzoek was gefocust op éénkristallen van vier verschillende types kwantummaterialen: Dirac knooppuntlijn semimetalen, bismuth dichalcogeniden, elementen, en overgangsmetaal di- en trichalcogeniden.

In dit werk is het gevestigde Dirac knooppuntlijn semimetaal ZrSiS verder onderzocht om het effect van uniaxiale deformatie op haar fijngevoelige electronische structuur te verduidelijken. De magnetoweerstand van een monster was gemeten onder trek- (tot 0.34 %) en drukdeformatie (tot $-0.28$ %) uitgeoefend op de $a$-as en in een magnetische veld van tot 30 T hoog. Een systematische verzwakking van de piekenstruktuur was waargenomen in het Shubnikov-de Haas frequentiespectrum wanneer er van druk- naar trekdeformatie werd gegaan. Dit effect zou kunnen worden verklaard door een verlaging in de effectieve kwantummobiliteit bij het verlagen van de $c/a$ verhouding, wat bevestigd wordt door een gelijktijdige verhoging van de Dingle-temperatuur.

Een tweede Dirac knooppuntlijn semimetaal dat onderzocht was is ZrSiTe. We wilden de magnetoweerstand onderzoeken om een beter begrip te krijgen van het effect van uniaxiale deformatie op de magnetoweerstand en Shubnikov-de Haas oscillaties van ZrSiTe. Dit zou ons in staat stellen om de verkregen resultaten te koppelen aan die van haar zusterverbindingen ZrSiS en ZrSiSe, die allebei in het verleden al uniaxiaal zijn gedeformeerd. Omdat de Haas-van Alphen oscillaties vroeger al experimenteel zijn waargenomen in ZrSiTe, was het enigszins te verwachten dat ons monster ook Shubnikov-de Haas oscillaties zou laten zien. De oscillaties waren echter niet aanwezig in ons gemeten monster, wat we toeschrijven aan de kleine

restweerstandsverhouding van het monster en het feit dat de de Haas-van Alphen oscillaties in de literatuur vrij zwak zijn.

Onderdeel van een nieuwe family van gelaagde supergeleiders is de bismuth dichalcogenide $LaO_{0.8}F_{0.2}BiS_{2-x}Se_x$ ($x = 0.5$ en $x = 1.0$). Dit materiaal is gekarakteriseerd bij hogere velden dan in het verleden gedaan was, met als doel een beter begrip te vormen van de extreem hoge $B_{c2}$ in het vlak. De $B_{c2}$ overtreft de conventionele paramagnetische en orbitale limieten ruimschoots, wat meestal wordt toegeschreven aan de locale inversiesymmetrie-geïnduceerde Rashba-type spin-baankoppeling van het materiaal. Ons onderzoek was specifiek gericht op het onderzoeken van de rol van de Josephson vortex toestand met betrekking tot de locale inversiesymmetrie en hoe het het sleutelmechanisme zou kunnen zijn dat verantwoordelijk is voor de hoge $B_{c2}$. Onze data laat zien dat de opwaartse trend van de $B_{c2}$ voort blijft bestaan terwijl $T$ het absolute nulpunt nadert. Bovendien zijn de berekende coherentie lengtes $\xi_{\perp}(0)$ niet klein genoeg om de aanwezigheid van Josephson vortices te suggereren, wat ons tot de rede leidt dat er geen Josephson vortex toestand aanwezig is in deze familie van $BiCh_2$-gebaseerde supergeleiders. Toekomstig onderzoek zou een beslissender beeld kunnen leveren met betrekking tot de dimensionaliteit van $BiCh_2$-gebaseerde systemen bij lage temperaturen. Dit zou onze bevindingen kunnen bevestigen.

Er was geëxperimenteerd met uniaxiale deformatie op $LaO_{0.8}F_{0.2}BiSSe$, één van de twee dopingniveaus van de bovengenoemde kristallen. Een sterke daling in de $B_{c2}$ en een kleine daling in de $T_c$ werd waargenomen wanneer uniaxiale deformatie langs de $a$-as was aangelegd, zoals bij de nematische supergeleider $Sr_xBi_2Se_3$. Dit bekrachtigde ons doel om het effect van uniaxiale deformatie op de nematische supergeleiding van $LaO_{0.8}F_{0.2}BiSSe$ te onderzoeken. De bowtie montagemethode werd gebruikt met goed gevolg, wat de potentie en functionaliteit ervan heeft bevestigd. In de toekomst zou onderzoek op het gebied van uniaxiale deformatie metingen uit kunnen voeren langs andere assen, om mogelijk licht te werpen op de afstemming van nematische supergeleiders met een tetragonale kristalstructuur door middel van deformatie.

Bulk bismuth (Bi) en gedoopt bismuth ($Bi_{0.96}Sb_{0.04}$) zijn onderzocht door middel van uniaxiale deformatie met de bedoeling om een brug te slaan tussen de theoretische literatuur en eerder experimenteel onderzoek. Idealiter werd er een beter begrip verkregen op het gebied van de driedimensionale topologische eigenschappen van gedeformeerd bismuth. We rapporteren de waarneming van twee systematische deformatie-effecten: een verandering in kwantummobiliteit

door deformatie, en een frequentieverschuiving, wat waarschijnlijk het resultaat is van een verandering in de grootte van het vlak dat de quasi-deeltjes herbergt. Dit impliceert dat de deformatie de degeneratie van het bovengenoemde vlak opheft en is in overeenstemming met de literatuur. Hoewel het wel theoretisch voorspeld is vonden we geen faseovergangen van triviaal naar topologisch of semimetallisch naar halfgeleidend waar in Bi of $Bi_{0.96}Sb_{0.04}$. Dit suggereert dat onze graad van deformatie te laag was en spoort toekomstig onderzoek aan om bismuth te bestuderen door middel van een hogere mate van deformatie.

Hooggeoriënteerd pyrolitisch grafiet was verkennend onderzocht door middel van uniaxiale deformatie met de bedoeling om meer te weten te komen over het effect van uniaxiale deformatie op materialen met een topologisch karakter. Een kleine verandering in de fast Fourier transform-amplitude door trekdeformatie werd waargenomen, wat toegekend werd aan een verandering in kwantummobiliteit. Dit zou het resultaat kunnen zijn van verhoogde uitlijning van de kristallieten. Dat zou namelijk de structurele wanorde verminderen en kwantum oscillatie-gerelateerde fenomenen verhelderen. Toekomstig onderzoek op het gebied van uniaxiale deformatie zou zich wederom kunnen richten op het toepassen van een hogere mate van deformatie.

Met het doel om het begrip van concurrentie tussen de supergeleidende fase en de ladingdichtheidsgolf fase uit te breiden, werd er ook op $NbSe_2$ en $ZrTe_3$ geëxperimenteerd door middel van uniaxiale deformatie. Er was geen verschuiving waargenomen van $T_c$ of $T_{cdw}$ voor beide materialen. Omdat de literatuur anders voorspelt is het denkbaar dat de afwezigheid van deformatie-effecten het resultaat zou kunnen zijn van het feit dat de toegepaste deformatie klein was, en misschien niet groot genoeg was om de bandenstructuur van de materialen dermate aan te passen opdat het zich zou uiten in de gemeten weerstandsdata. Net zoals de twee bovengenoemde materialen zou toekomstig onderzoek zich kunnen richten op het toepassen van een hogere mate van deformatie, echter moet er op gelet worden dat de monsters zich in het elastische regime blijven begeven.

$IrTe_2$ is een overgangsmetaal dichalcogenide zoals $NbSe_2$, maar dankt haar lading geordende fase niet aan ladingdichtheidsgolffysica maar aan dimeervorming. Met het voornemen om de afstembaarheid door middel van deformatie van $T_s$ en daarmee het effect op $T_c$ te onderzoeken, werden deformatie experimenten succesvol op $IrTe_2$ monsters uitgevoerd met het gebruik van de bowtie montagemethode. Er werd echter geen verandering door deformatie in de $T_s$ of $T_c$ waargenomen. Zonder de beschikbaarheid van monsters die groot genoeg waren voor de conven-

tionele montagemethode was het gebruik van de bowtie montagemethode de enige optie. Omdat de conventionele montagemethode betrouwbaarder is, raden we aan dat toekomstig onderzoek grotere monsters probeert te verkrijgen en de conventionele montagemethode gebruikt als het het plan is om onze data te bekrachtigen.

Tenslotte hopen we dat het werk dat gepresenteerd wordt in dit proefschrift een waardevolle toevoeging is aan de basis van onderzoek op het gebied van uniaxiale deformatie, wat zich nog in een vroege staat bevindt. Het vermogen om electronische eigenschappen van kristallen te bestuderen bij een hogere mate van deformatie is wenselijk en deze wens wordt in dit proefschrift en in recente overzichtsartikelen benadrukt [29, 43]. Met een overvloed van nieuwe en interessante natuurkunde dat nog ontdekt moet worden, geloven wij dat uniaxiale deformatie een belangrijke afstemmingsparameter zal blijven als het om de opheldering van opkomende verschijnselen in kwantummaterialen gaat.

# Acknowledgements

The support I have received from a great number of people have made it possible for me to bring my PhD research to a satisfying conclusion. First I want to thank **Anne**, my promotor. Your attention to detail and ability to deal with setbacks have had an exceptionally positive effect on both the quality of my work and my emotional wellbeing. I have always appreciated your patience and look back fondly on the time we spent together at Science Park. I'm sure you won't run out of fun ways to spend your days in retirement! **Mark**, you have been everything I wanted in a copromotor. Thank you for your advice on both academic and personal matters, and for our casual conversations together. **Jean-Sébastien**, your input during my evaluation sessions has helped me keep my research on track, I appreciate you as my independent supervisor.

Thanks to **Yingkai**, **Leslie** and **Ratnadwip** for providing me with high quality single crystals that have been absolutely crucial to my research. Thank you **Irene** and **Weiyi** for your DFT calculations on ZrSiS that firmly convinced the last referee to greenlight the paper. Thanks to the UvA Technology Centre for all the technical help over the years: **Gerrit**, **Johan**, **Tjeerd**, **Sven**, **Tristan**, and **Hans**. **Astrid**, it has always been very pleasant to have you as IoP secretary, I'm going to miss seeing your smile. **Ayako**, your presence in the lab for a few months during my master's project was nice, thanks for teaching me how to make the tiny AC susceptibility coil! From Nijmegen, most notably **Jasper**, **Arwin**, **Thom**, and **Steffen**, it's been a blast doing research with you guys and performing experiments at the very extreme, supported by HFML-RU/NWO-I. The relaxed atmosphere you facilitated really made me want to come back to HMFL again and again. **Erik**, I greatly appreciate your efforts that led to the creation of the TopCore consortium under Grant No. OCENW.GROOT.2019.048, supported by the Dutch Research Council (NWO).

A large number of people at Science Park have been responsible for making my time here enjoyable for the full four years. I want to thank several of them in particular. **Marc**, your laidback attitude and dry/dark humour made sure to take the edge off at the start of my master's project. You made me feel welcome in the lab and didn't hesitate to help me when I was frustrated or stuck on something. I'm sure we'll stay in touch forever and I look forward to talking to you more about history, politics and video games. **Sergio**, I really respect you as a scientist and I

truly admire your knowledge and determination. I am certain you have a bright future ahead and I hope to be a part of it in one way or another. **Saumya** and **Arnaud**, having you guys and your positive attitudes around reminded me not to take things too seriously all the time and helped me focus on what's important. **Marco** and **Daan**, thanks for our coffee talks on career choices and job opportunities. Your opinions and tips are very valuable to me, as I've always had difficulty deciding on career direction. **Freek**, I enjoyed having you as my colleague and I'm glad you've been feeling better lately. I'll miss our relaxing conversations.

When Marc left, it got quieter and a bit harder to be excited about going to the lab. Just a few months later and with perfect timing, **Marie** showed up to the institute. Your energetic personality was easily sufficient to tunnel the gap left behind by Marc. Since then, we've spent many hours in the common room having fun and making sure we were both doing alright. I'll make sure to keep dropping by for lunch! Besides Marie, I've witnessed many more excellent additions to the institute during the last year of my PhD. Thanks **Falk**, for your chill vibes and stoic view on things. I hope you enjoy your time in Denmark, and we'll have to stay in touch to discuss One Piece... You too, **Farhan**! Thanks **Crystal** for our comfy conversations and for teaching me things about Cyprus. **Anne Claude**, your cheerful and respectful attitude has often brightened my day. I'll certainly visit Strasbourg in the future! **Katya**, good luck finalizing your PhD and we'll have to talk about our jewelcrafting business more later... Thanks **Grisha**, for your grounding takes and your healthy dose of sarcasm. **Madeline**, your presence always improved the quality of my coffee breaks. Surely our shared struggles when it comes to career choice will ultimately diminish. **Jared**, thanks for the pleasant talks in the common room. Your smile and positivity are greatly appreciated. **Anna**, I'm excited to see who's going to win our bet! Having you around at and outside of Science Park was always fun. I also want to share my appreciation for the QMat group in general, everyone there has contributed to my growth as a scientist and its activities have improved my relevant skills significantly.

I would've never had the opportunity to do a PhD if I hadn't successfully completed my physics studies. Thanks **Auke**, **Mitchel**, **Levi**, **Hiele**, **Matthijs**, **Hoang**, **Alparslan**, and **Joris** for the moral support throughout, and for a ton of fun times together. Thanks to you too, **Thomas**, for being both a great friend and a fine paranymph. I'm really enjoying living together with you in the new house! Big shoutout to my online friend group as well: **Reio**, **Squid**, **Funky**, **Ali**, **Evertras**, **Soek**, **Invo**, **Nes**, **Luigi**, **Rai**, **Pie**, and **Toge**. Your jokes and daily presence could

keep me going in any situation and I deeply value the connection we have built up over the last 14 years.

I want to express my most sincere gratitude to the people closest to me. **Olga**, **Evy** and **David**, you have always supported me and believed in me. Thank you for consistently wishing me the best, no matter what. Thanks to my father **Maarten** for convincing me to set the bar high and providing me with the foundation of confidence to pursue my goal of acquiring a PhD. And finally, thank you **Yani**, for all your love and support. It was during these four years you entered my life and I am very, very happy you did.